ns^2-md^0 POST-TRANSITION METAL OXIDES FOR SOLAR ENERGY APPLICATIONS

by

EDAN BAINGLASS

DISSERTATION

Submitted in partial fulfillment of the requirements
for the degree of Doctor of Philosophy at
The University of Texas at Arlington
August, 2020

Arlington, Texas

Supervising Committee:

Muhammad N. Huda, Supervising Professor
Alexander Weiss
Qiming Zhang
Ali Koymen
Benjamin Jones

Abstract

ns^2-md^0 Post-Transition Metal Oxides for Solar Energy Applications

Edan Bainglass, Ph. D.

The University of Texas at Arlington, 2020

Supervising Professor: Muhammad N. Huda

Meeting the growing global energy demand while mitigating the deterioration of the global climate requires the rapid introduction of clean, renewable, and sustainable fuels. Solar energy output at daytime provides more than enough to satiate global demands. However, to utilize solar energy at night would require the development of efficient materials for solar energy storage. Photoelectrochemical (PEC) water-splitting is regarded as one of the most promising solar storage technologies. The material properties necessary to drive both O_2 and H_2 evolution reactions may be decoupled by designing a photoanode-photocathode PEC cell, with each half reaction respectively handled by an n-type and a p-type semiconductor.

In this dissertation, the ns^2-md^0 metal oxide class is investigated computationally using density functional theory to determine its viability as a platform on which to design and develop the next generation of materials for solar energy applications. Metal oxides are stable, abundant, and environmentally safe. They are also highly flexible in their electronic properties. Many n-type metal oxides have been studied for PEC applications in attempt to improve their light absorption and conduction properties. In contrast, p-type metal oxides are rare due to the depth of the O 2p dominated valence band maxima (VBM) of metal oxides. The ns^2-md^0 class has been suggested

as a mechanism for upshifting the VBM and improving hole carrier mobility via ns^2 – O 2p hybridization. The first part of the dissertation aims to study the electronic structure of ns^2-md^0 systems in various crystal symmetries containing different *n* and *m* values.

The second part studies the theoretically predicted novel quaternary metal oxide $CuBiW_2O_8$ (CBTO), which has recently been successfully synthesized and identified as a promising p-type solar absorber. Here, the introduction of Cu 3d orbitals in an ns^2-md^0 system further upshifts the VBM due to the height of Cu 3d energy levels relative to O 2p. However, localized Cu 3d orbitals also hinder efficient charge extraction. Anion doping in the form of S-in-O substitution is investigated as a means of reducing VBM localization.

Lastly, CBTO surfaces are explored as an initial step in a larger study aimed to determine the effects of secondary phase impurities observed on the CBTO sample surface during the experimental synthesis. To estimate the relative stabilities of CBTO surfaces, an improved methodology is proposed to calculate surface energies addressing the inherent complexities of quaternary metal oxides.

Acknowledgements

First and foremost, I would like to thank my research advisor, Dr. Muhammad N. Huda, for allowing me the opportunity to conduct research under his tutelage. My interest in the field of condensed matter physics and my love for computational methodologies were born out of countless fruitful discussions in his office. These conversations, which often went beyond scientific topics and into philosophical territories, stimulated my mind and provided an avenue for intellectual growth and exploration. I am immensely grateful for his guidance and time. Success in this field would not have been possible without his support.

I would also like to thank my committee members, Dr. Alexander Weiss, Dr. Ali Koymen, Dr. Qiming Zhang, and Dr. Benjamin Jones, for their time, support, and tutelage. I have had the pleasure of attending their courses and enriching my education through their dedicated instruction. I have also had the great pleasure of collaborating with Dr. Jones on a research project probing the origins of matter. I am deeply thankful to Dr. Ramon Lopez for his support through the AACCESS program that allowed me to transfer to and finance my education at the University of Texas at Arlington. I also thank Ms. Stacey Cody for her patience and diligence with any and all my requests and quandaries over the years. Her role in supporting the physics department is truly unparallel.

I am grateful to the Office of Graduate Studies for their financial support during the last stretch of my program through the Dissertation Fellowship. My successful completion and defense of this dissertation would not have been possible otherwise. I am similarly grateful for the financial support of the Truman D. Black endowment, Dr. John L. Fry endowment, Scharf endowment, and the James L. Horwitz scholarship fund, for providing relief from stress and allowing greater focus on producing quality research.

I give special thanks to my group members, Dr. Sajib Barman, Hori Pada Sarker, Noura Alkhaldi, Hussain Alathlawi, Hany Mahdy, and Achyuth Manoj, as well as past group members Dr. Pranab Sarker, Dr. Shafaq Moten, Dr. Sarah Hernandez, and the late Dr. Cedric Mayfield, for their support, guidance, and encouragement. I am especially indebted to Dr. Cedric Mayfield for his help and counsel in my early graduate years. It saddens me greatly not being able to share with him the fruits of my work. We miss him greatly.

Lastly, I would like to thank the National Science Foundation for supporting my research and providing access to the resources of the Texas Advanced Computing Center (TACC). Similarly, I would like to thank the High Performance Computing (HPC) center at the University of Texas at Arlington for their resources.

Table of Contents

Chapter 1

Introduction

1.1. Global Crisis

A 2019 United Nations report[1] has set a mid-century projection for the global population at around 10 billion – a growth of 25% over the next 30 years. Global economies are projected to follow with a yearly growth rate of 3% in gross domestic product (GDP)[2]. The growing demand for energy is set to hit a global consumption rate of 180,000 TWh by 2050, an increase of nearly 50% from 2018. Residential and commercial sectors slowly but gradually shift towards cleaner electrical power as technologies continue to improve. However, the bulk of energy consumption so far remains in the industrial sector, which still favors highly-efficient, energy-dense fossil fuels. It is an overwhelming consensus that the unchecked use of fossil fuels has resulted in the exponential growth in heat-trapping greenhouse gases leading to the increase in global temperatures[3]. The strain on the global ecosystem has surpassed sustainable levels, evident in its catastrophic effects felt across the globe over the past decade[4]. Counteracting the changing climate while meeting the growing demand for energy would require the introduction of cleaner fuel sources into the global power grid. Of the various renewable fuels that may satiate the energy demand, solar energy remains the only sustainable clean source, with solar radiation incident on Earth far outweighing the global consumption rate[5,6]. However, like other renewable sources, solar energy is both intermittent and nonuniformly distributed[7]. To overcome these challenges, an efficient method for storing solar energy must be developed.

1.2. Photoelectrochemical Water-Splitting

One of the most promising solar-energy-storage technologies is photoelectrochemical (PEC) water-splitting[8] – an artificial photosynthesis-like process aimed at converting solar energy

into clean chemical energy stored in hydrogen gas. The market for hydrogen is widespread and has seen significant growth over the past decade[9]. The high efficiency and zero-CO_2 emissions of hydrogen fuel cells makes them ideal candidates for clean power generation[10,11]. However, their mass commercialization has yet to occur due to their substantial cost compared to fossil-based technologies. To drive down the cost, several aspects of the hydrogen fuel cycle must be addressed. On the production side, PEC water-splitting offers a clean and renewable solution to generating hydrogen fuel from abundant sources, i.e. water and sunlight. However, material requirements for achieving high PEC solar-to-hydrogen conversion efficiencies are stringent and have yet to be met cost-effectively[12]. A new generation of materials must be developed to address both the technical and non-technical aspects of PEC devices.

Solar-to-hydrogen PEC conversion begins with the splitting of water molecules. The over-all uphill chemical reaction is written as[13]

$$2H_2O \rightarrow 2H_2 + O_2 \tag{1.1}$$

and requires 1.23 V to initiate. In a PEC cell (fig. 1.1), the reaction is driven by the potential difference of electron-hole pairs generated from absorbed photons. In the valence band, holes of energy lower than the water oxidation potential participate in the oxygen evolution reaction (OER)

$$2H_2O + 4h^+ \rightarrow O_2 + 4H^+ \tag{1.2}$$

while excited electrons in the conduction band with higher energy than the water reduction poten-tial drive the hydrogen evolution reaction (HER)

$$4H^+ + 4e^- \rightarrow 2H_2 \tag{1.3}$$

To achieve stoichiometric water-splitting, the valence-to-conduction band gap must straddle both OER and HER potentials. For high efficiency, the band gap should be large enough to overcome the minimum required voltage, as well as the overpotentials associated with reaction kinetics at

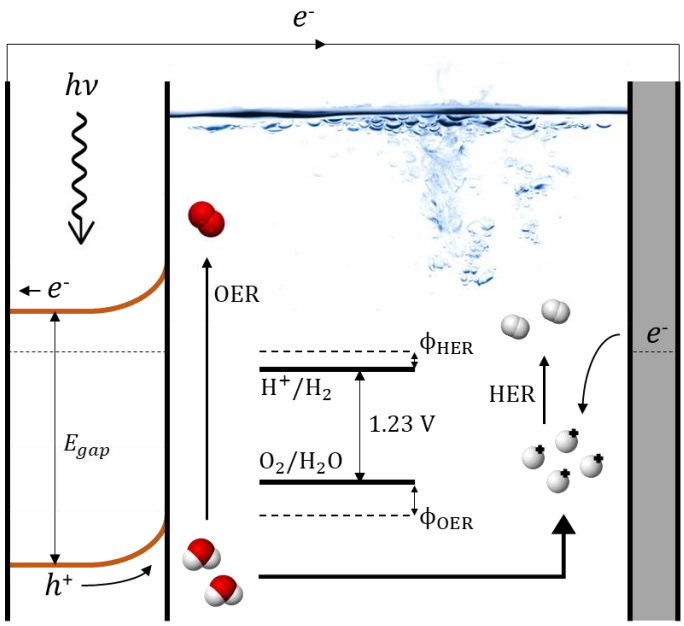

Figure 1.1. Photoelectrochemical water-splitting (PEC) mechanism. This single-photoanode cell illustrates the photoexcitation process, oxygen evolution reaction (OER), hydrogen evolution reaction (HER), and overpotentials (ϕ).

the solid-liquid interface[8]. However, the band gap should be small enough to capture sufficient sunlight. Ideal band gaps are often quoted around 2 eV for optimal efficiency. To facilitate the migration of charge carriers towards the solid-liquid interface and avoid bulk and/or surface re-combination of charge carriers, materials must maximize carrier mobilities and minimize charge trapping. Furthermore, materials must not react chemically with the aqueous solution (corrosion resistant), nor degrade under illumination. In addition to the technical requirements, other crucial considerations regarding the choice of materials include both the abundancy of its elemental constituents and their post-processing environmental impact.

1.3. Metal Oxides

Since the initial proof of concept in 1972 by Fujishima and Honda[14], much research has been conducted in the development of efficient and cost-effective materials for PEC cells. Of the various classes of materials, metal oxides are some of the most versatile, studied for both

photovoltaic (PV)[15] and PEC applications[16,17]. They are non-toxic, chemically stable, and thus abundant in nature. They are relatively simple to synthesize, highly tunable, and possess a broad range of band gaps and band edge positions with respect to the water redox potentials (fig. 1.1). However, due to wide band gaps, high recombination rates, and low conductivity, metal oxides have yielded weak photocurrents and overall low solar-to-hydrogen conversion efficiencies. Several schemes exist for optimizing metal oxide properties including doping and alloying, nanoscale design, synthesis-control, post-processing surface treatments, and heterostructure design. The present dissertation focuses primarily on electronic structure modification through the introduction and mixing of electronic bands from transition and post-transition metals through alloying. Anion doping is also considered. Lastly, the technique of semiconductor heterojunctions is discussed within the scope of improving charge transport.

PEC cells come in various flavors[16]. In a single-light-absorber cell (fig. 1.1), for example, a photoanode converts light into hole-electron pairs. Holes oxidize water at the surface, while electrons are pulled to a counter electrode, where they reduce water and generate H_2 gas. For a self-biasing cell, the band edge positions in the photoanode are required to straddle the water redox potentials. Materials such as TiO_2 and ZnO meet this requirement. However, their wide band gaps (> 3 eV) limits the capture of light leading to poor efficiencies[11], with current densities less than 1 mA/cm^2. Developing a single material to fit all the necessary requirements has proven a major challenge to single photoelectrode PEC cells. An alternative to the above design is to replace the counter electrode with a photocathode (fig. 1.2). The use of separate materials decouples the water-splitting half-reactions and removes the straddling band gap condition. Not only that each photoelectrode now handles its own respective reaction, allowing for greater flexibility in band edge positions, but the two semiconductors may also exhibit different band gaps, extending the range

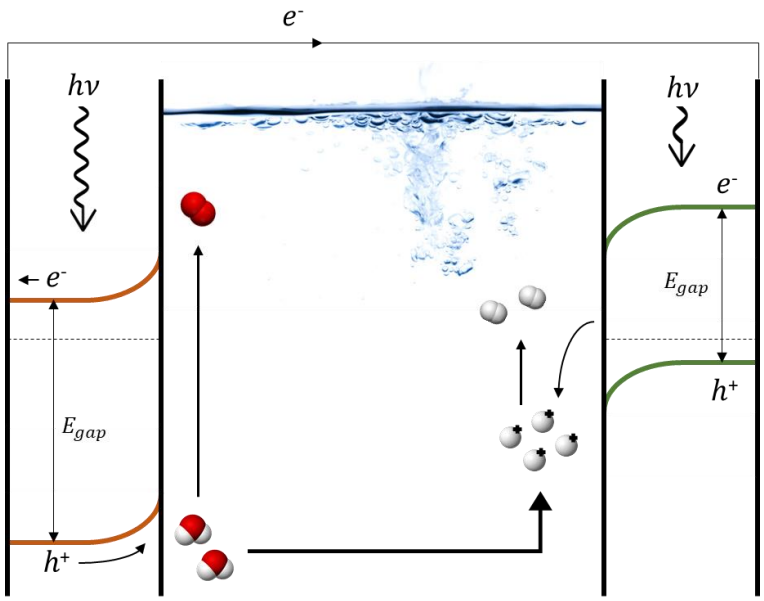

Figure 1.2. Photoanode-photocathode PEC cell. Unlike the single-photoelectrode cell (fig. 1.1), this design allows n-type and p-type photoelectrodes to independently handle the OER and HER processes, respectively. This design also benefits from additional light absorption at a different energy range.

of photon energies available to the cell. The duel photoelectrode design is thus attractive due to its inherent p-n bias and ability to capture a larger portion of the solar spectrum.

A challenge of p-n PEC cell designs is an inherent difficulty of p-type doping in metal oxides[18,19]. This is primarily attributed to the depth of O 2p orbitals which form the valence band maxima (VBM) of metal oxides. Due to their high electronegativity, O-sites act as localized hole traps[20] preventing charge migration and increasing recombination rates. Deep O 2p VBM states also require greater ionization energies, which precludes their use in ambient conditions. Furthermore, fermi level shifting towards the VBM in the presence of p-type dopants is exacerbated by the deep O 2p VBM and results in larger formation probabilities of so-called "acceptor-killer" defects[18]. To overcome the p-type doping limit, it is necessary to increase the VBM energy. Two proposed solutions involving the upshift of O 2p dominated VBM are: (i) the introduction of transition metals of filled nd^{10} electronic configuration; and (ii) the coupling of post-transition metal lone-pair electrons to O 2p orbitals.

In the first approach, nd^{10} – O 2p orbital overlap gives rise to an occupied antibonding state at a higher VBM than that formed by O 2p alone. Ideal nd^{10} candidates are Cu^{1+} and Ag^{1+}, both having d-orbitals of higher energy than O 2p, thus ensuring the upshift of the VBM via orbital hybridization. Among Cu^{1+} containing ternary oxides, Cu-delafossites are known to be p-type oxides, where $CuM^{IIIB}O_2$ (M^{IIIB} = Sc, Y, La) are better p-type candidates than $CuM^{IIIA}O_2$ (M^{IIIB} = Al, Ga, In) due to modifications in electronic properties in response to changes in structural symmetry[21]. Earlier, Kawazoe et al.[22] confirmed the inherent p-type conductivity of $CuAlO_2$ and $CuGaO_2$ of the delafossite structure via Hall mobility measurements and attributed it to spontaneous Cu^{1+} vacancies. The authors also confirmed p-type conductivity in non-delafossite K-doped $SrCu_2O_2$. Many other Cu^{1+} ternary compounds can be found in the literature[23,24]. Ag 4d – O 2p hybridization and subsequent VBM upshift have also been observed in Ag^{1+} compounds such as $AgNbO_3$, Ag_2MoO_4, and $AgVO_3$[25]. However, Ag^{1+} compounds are difficult to synthesize and exhibit lower conductivity compared to Cu^{1+} systems[20,26], which themselves suffer from low hole mobility due to the highly localized nature of 3d orbitals. Moreover, many of these ternary compounds still exhibit wide band gaps above 3 eV, which limits their capacity for solar energy capture.

In the second approach, lone-pair electrons of post-transition metal ions, e.g. Bi^{3+}, Sb^{3+}, Pb^{2+}, Sn^{2+}, are introduced via doping and/or alloying and couple with O orbitals in ns^2 – O 2p hybridized states. The antibonding portion forms a higher energy VBM reducing ionization energies and narrowing band gaps. In addition, s-p hybridization yields more dispersive bands, thus increasing hole mobility and reducing recombination rates. Additional coupling of md^0 orbitals from a second cation in ns^2-md^0 ternary metal oxide alloys is expected to further improve electron mobilities and reduce band gaps through md^0 – O 2p hybridization[27–29]. $BiVO_4$, an ns^2-md^0

compound often regarded as a paradigm in PEC research[30–32], exhibits a Bi 6s – O 2p dispersive antibonding state at the VBM resulting in a 2.5 eV direct band gap. However, dispersion at the conduction band minimum (CBM) is less due to the localized nature of V 3d electrons. Low electron mobility results in the formation of small polaronic states and conduction governed by polaron hopping[33–35]. This has led to photocurrents significantly lower than theoretically predicted[35,36] for $BiVO_4$-based PEC cells. The use of md^0 transition metals of higher periods (m = 4, 5) is expected to yield more dispersed conduction bands and improved electron mobilities due to reduced localization. It has been demonstrated by first principle study[37] that alloying of Nb (4d) in $BiVO_4$ indeed reduces the electron effective mass due to relatively more delocalized band at CBM.

The above two are concerned with upshifting the O 2p VBM through hybridization with cation orbitals to enhance solar energy capture and allow for p-type semiconductor engineering. Careful selection of dopant species may improve charge mobility through orbital delocalization. Anion doping of S, Se, or Te in O-sites can further improve both carrier mobility and solar energy capture through reduced p orbital localization at higher periods. The lower stability of metal chalcogenides in aqueous solutions may be mitigated via protective coating such as graphene[38–40], which can suppress surface reactivity and prolong the stability of the semiconductor. However, such techniques may also impact the efficiency of the PEC process. Nevertheless, quaternary metal chalcogenides, such as $CuIn_xGa_{1-x}Se_2$ (CIGS) and Cu_2ZnSnS_4 (CZTS), have been studied extensively in recent years. These complex materials exhibit light absorption in the visible-range and high carrier mobilities, as well as favorable band edge positions for PEC applications[41,42]. Moreover, p-type conduction has been demonstrated in both[43–45]. However, expensive components and synthesis processes prevent their commercialization.

Following the design principles of the solutions discussed thus far, one may attempt to design multinary metal oxides of a d^{10}-ns^2-md^0 electronic configuration, taking advantage of both the delocalization mechanism of s-p hybridization, as well as the VBM upshift and band gap narrowing mechanism of d^{10} – O 2p hybridization. Several Cu^{1+} and Ag^{1+} quaternary metal oxides have already been developed[46–48]. A novel Cu^{1+}-based solar-absorber was recently predicted from first-principles, namely $CuBiW_2O_8$ (CBTO), with promising material properties for PEC applications[49] and has since been verified experimentally[50]. Hall mobility measurements confirm p-type conduction, as expected from the Cu^{1+} compounds. However, slow hole mobility resulted in diffusion lengths shorter than the optical absorption depth, preventing efficient solar energy conversion. This was partially attributed to a persistent presence of Bi_2WO_6 impurities at the sample surface. Further theoretical calculations confirmed that the impurities are thermodynamically supported and are not an artifact of experimental design. This motivates a study of the Bi_2WO_6-CBTO interface and its effects on the overall electronic properties of CBTO.

1.4. Current Scope

The present dissertation is concerned in general with the ns^2-md^0 class of materials. First, the stibiotantalite mineral, or $Sb(Ta,Nb)O_4$, is examined. Structural and electronic properties are investigated as functions of crystal phase by modeling $Sb(Ta,Nb)O_4$ on its own orthorhombic layered phase, and on the monoclinic and tetragonal phases of $BiVO_4$. Also, the md^0 character is varied from Ta (m = 5) to Nb (m = 4) to test the effects of higher period d-orbitals on the band gap and band dispersion properties. Next, the layered structure of the russellite mineral, or Bi_2WO_6, is examined. Here, the behavior of lone-pair electrons in a mixed 5s/6s environment is investigated through Sb-in-Bi substitutions. The configurational space of the $BiSbWO_6$ alloy is explored with emphasis on the effects of lone-pair electrons on the electronic structure.

The following two chapters then switch attention to the d^{10}-modulated ns^2-md^0 class by focusing on the newly developed CBTO compound. First, anion doping is considered through S-in-O substitutions to study the effects of higher period p orbitals on the localization of the Cu 3d dominated VBM. Next, the stable surfaces of CBTO are calculated following a proposed guideline for theoretical determination of accurate surface energies in preparation for a future interface study addressing the presence of Bi_2WO_6 impurities.

1.5. Summary

The overall study sets out to determine the viability of the ns^2-md^0 material design pertaining to the requirements of the PEC process. Results provided here will serve as a base understanding on which to develop and engineer the next generation of solar energy converting materials. At its core, the study provides a thorough examination of the various mechanism by which the shortcomings of metal oxides may be lifted and improved. The first principles study follows the density functional theory framework, as described in the next chapter.

Chapter 2

Theoretical and Computational Methodology

The following sections detail the fundamental theory behind the calculations performed in this dissertation. The information provided draws on reviews by Parr and Yang[51], Jones[52], Capelle[53], and Cramer[54], as well as the Nobel lecture given by Walter Kohn[55], the founding father of density functional theory. Note that throughout the chapter, Hartree atomic units are considered, where the elementary charge e, electron mass m_e, coulomb constant $4\pi\varepsilon_0$, and reduced Planck constant $\hbar$ are all unity. Lengths are given in Bohr radius a_0 (0.529 Å).

2.1. The Electronic Many-Body Problem

The electronic structure of matter is inherently a quantum mechanical problem, and as such, it intuitively involves the Schrödinger equation. For a non-relativistic, time independent system, the Schrödinger equation is given by

$$\hat{H}\Psi = E\Psi \tag{2.1}$$

where $\hat{H}$ is the Hamiltonian operator, E the energy of the system, and Ψ the wavefunction. The Hamiltonian operator of an N-electron, M-nuclei, solid-state system is given by

$$\hat{H} = -\frac{1}{2}\sum_{i}^{N}\nabla_{r_i}^2 - \frac{1}{2}\sum_{i}^{M}\nabla_{R_i}^2 + \sum_{i<j}^{N}\frac{1}{r_{ij}} + \sum_{i<j}^{M}\frac{Z_i Z_j}{R_{ij}} - \sum_{i}^{M}\sum_{j}^{N}\frac{Z_i}{\left|\vec{R}_i - \vec{r}_j\right|} \tag{2.2}$$

or more compactly

$$\hat{H} = \hat{T}_e + \hat{T}_n + \hat{V}_{ee} + \hat{V}_{nn} + \hat{V}_{ne} \tag{2.3}$$

where $\hat{T}_e$ and $\hat{T}_n$ are the kinetic energy operators of electrons and nuclei, $\hat{V}_{ee}$ and $\hat{V}_{nn}$ are their interaction operators, and $\hat{V}_{ne}$ is the electron-nuclei mutual interaction term. Under the Born-Oppenheimer approximation, which considers nuclei as static in the electronic inertial frame, eq. 2.3 can be decoupled into separate electronic and nuclear parts

$$\hat{H}_e = \hat{T}_e + \hat{V}_{ee} + \hat{V}_{ne} \tag{2.4}$$

$$\hat{H}_n = \hat{T}_n + \hat{V}_{nn} \tag{2.5}$$

with the latter used in eq. 2.1 to separately obtain the nuclear energy of the system. The last term in eq. 2.4 considers the effect of nuclei on electrons as an external coulombic potential $v(\vec{r})$. Using eq. 2.2, the potential is defined as

$$\hat{V}_{ne} = -\sum_{i}^{N}\sum_{j}^{M}\frac{Z_j}{r_{ij}} = \sum_{i}^{N} v(\vec{r}_i) \tag{2.6}$$

$$v(\vec{r}_i) = -\sum_{j}^{M}\frac{Z_j}{r_{ij}} \tag{2.7}$$

where r_{ij} is the distance between the i^{th} electron and the j^{th} nucleus of charge Z_j.

In solid-state matter, the set of eigenstate solutions $\{\Psi_i\}$, with corresponding eigenvalues $\{E_i\}$, must obey the periodic boundary conditions of the system, as well as the antisymmetric requirement associated with exchange of fermionic particles. In accordance with the statistical interpretation of quantum mechanics, the absolute value squared of ψ_i leads to the probability of finding the system in the i^{th} quantum states. The states are hence also orthonormal

$$\langle \Psi_i | \Psi_j \rangle = \delta_{ij} \tag{2.8}$$

where δ_{ij} is the Kronecker delta, equal to 1 for $i = j$ and 0 otherwise. Measurements of a real observable quantity $\hat{O}$ may yield any of its corresponding eigenvalues. An average of measurements on an ensemble of like-systems is obtained from the expectation value of $\hat{O}$

$$\langle \hat{O} \rangle = \frac{\langle \Psi | \hat{O} | \Psi \rangle}{\langle \Psi | \Psi \rangle} \tag{2.9}$$

From the variational principle, taking the expectation value of $\hat{H}$ would yield the ground state energy E_0 only if the wavefunction Ψ represents the ground state Ψ_0. Then, for any guessed wavefunction Ψ, we have

$$E = \langle \Psi | \hat{H} | \Psi \rangle \geq \langle \Psi_0 | \hat{H} | \Psi_0 \rangle = E_0 \tag{2.10}$$

including the case where our initial guess is exactly the ground state. In the case it is not, minimization of the functional $E[\Psi]$ with respect to all allowed solutions would yield the ground state energy E_0, and thus the ground state wavefunction Ψ_0. By constraining the minimization process as follows

$$\delta\left[\langle \Psi | \hat{H} | \Psi \rangle - E\langle \Psi | \Psi \rangle\right] = 0 \tag{2.11}$$

where E is the Lagrange multiplier, the ground state wavefunction Ψ_0 is guaranteed to be normalized. This process then gives a recipe to obtain the ground state energy of the system E_0, among other observable quantities, from knowledge of the number of electrons N and the external nuclear potential $v(\vec{r})$. In other words, any real observable $\hat{O}$ of the solid-state system is a functional of N and $v(\vec{r})$ through Ψ.

The crux of the N-electron problem lies in the electron-electron interaction term $\hat{V}_{ee}$. The electronic Hamiltonian of eq. 2.4 involves $3N$ degrees of freedom. In a realistic system, $N \sim 10^{23}$, and exact analytical solutions exist up to $N = 2$. There also remains the question of how to model an N-electron wavefunction. A simple and convenient approximation is that of the Hartree method, in which the wavefunction Ψ_H is given as a product of decoupled single-electron eigenstates[54]

$$\Psi_H = \prod_i^N \psi_i(\vec{r}_i) \tag{2.12}$$

avoiding explicit determination of electron-electron correlation and exchange interactions. Instead, each electron is regarded as moving in an effective potential v_H

$$v_H(\vec{r}_i) = -\frac{Z_j}{r_{ij}} + \widehat{U}_i \tag{2.13}$$

constructed of a nuclear term with charge Z_j, and a mean-field potential

$$\widehat{U}_i = \sum_{j \neq i} \int \psi_j^*(\vec{r}\,') \frac{1}{|\vec{r}_i - \vec{r}\,'|} \psi_j(\vec{r}\,') d\vec{r}\,' \tag{2.14}$$

in which electron i interacts with an average electrostatic field of $N-1$ electrons. Passing the Hartree product through eq. 2.11 yields a set of single-electron differential equations

$$\left\{-\frac{1}{2}\nabla^2 + v_H(\vec{r}_i)\right\}\psi_i(\vec{r}_i) = \varepsilon_i \psi_i(\vec{r}_i) \tag{2.15}$$

Since v_H in eq. 2.13 involves the operator $\widehat{U}$ that is defined by the solution set, the problem is approached self-consistently. An initial guessed set of eigenstates $\{\psi_i\}$ defines the Hartree potential via eqs. 2.13 and 2.14. Solving eq. 2.15 then yields a new set of eigenstates $\{\psi_i\}$ that are presumably more accurate. The cycle repeats until input and output solution sets agree within predefined convergence criteria in total energy E, evaluated by[54]

$$E = \sum_i \varepsilon_i - \frac{1}{2}\sum_{i \neq j} \int\int \frac{|\psi_i|^2 |\psi_j|^2}{r_{ij}} d\vec{r}_i d\vec{r}_j \tag{2.16}$$

where the electron-electron repulsion energy is subtracted from the sum of the eigenvalues to account for the double-counting that arises from the use of the mean-field approximation.

The Hartree approximation, however, neglects the fermionic nature of electrons. Extending the framework of the Hartree approximation, Hartree-Fock (HF) theory replaces the Hartree product of eq. 2.12 with a single Slater determinant

$$\Psi_{HF} \approx \frac{1}{\sqrt{N!}} \begin{vmatrix} \psi_1(\vec{r}_1) & \cdots & \psi_N(\vec{r}_1) \\ \vdots & \ddots & \vdots \\ \psi_1(r_N) & \cdots & \psi_N(r_N) \end{vmatrix} \tag{2.17}$$

thus explicitly accounting for the antisymmetric requirement of fermions. Evaluating the expectation value $\langle \Psi_{HF} | \hat{V}_{ee} | \Psi_{HF} \rangle$ yields both 'Coulomb integrals'

$$\hat{J}_{ij} = \frac{1}{2} \int \int \psi_i(\vec{r}) \psi_i^*(\vec{r}) \frac{1}{|\vec{r} - \vec{r}'|} \psi_j^*(\vec{r}') \psi_j(\vec{r}') d\vec{r} d\vec{r}' \tag{2.18}$$

and 'exchange integrals'

$$\hat{K}_{ij} = \frac{1}{2} \int \int \psi_i^*(\vec{r}) \psi_j(\vec{r}) \frac{1}{|\vec{r} - \vec{r}'|} \psi_i(\vec{r}') \psi_j^*(\vec{r}') d\vec{r} d\vec{r}' \tag{2.19}$$

The Hartree-Fock electronic energy is then expressed as

$$E_{HF} = \sum_{i}^{N} \varepsilon_i - \hat{V}_{ee} \tag{2.20}$$

$$\hat{V}_{ee} = \frac{1}{2} \sum_{i,j=1}^{N} (\hat{J}_{ij} - \hat{K}_{ij}) \tag{2.21}$$

where eq. 2.21 is the total electron-electron repulsion energy. In the HF formalism, the classical electrostatic repulsion between electrons of like-spin is reduced due to their exchange interaction. This is often referred to as a 'Fermi hole' surrounding each electron and is a manifestation of the Pauli exclusion principle[54].

Though a significant improvement, and one that captures many physical properties of most molecular systems, the single Slater determinant model of HF theory is insufficient for larger systems. HF theory avoids errors due to self-interaction and provides an exact description of exchange energy. However, it does not properly account for the correlation of electrons. The error, or correlation energy E_{corr}^{HF}, defined as the difference between the true ground state energy and that calculated from eq. 2.20, can play a decisive role in describing the system. Methods that attempt to account for electronic correlation explicitly, such as multiconfiguration self-consistent theory, many-body perturbation theory, and coupled-cluster theory, quickly overtax available

computational resources due to the so-called exponential wall that is a consequence of the $3N$ degrees of freedom inherent in the wavefunction.

2.2. Density Functional Theory

The development of density functional theory (DFT), the state-of-the-art methodology for modern electronic-structure research, was motivated by the need for an efficient and exact theory of matter. Its mathematical rigor was provided by the Hohenberg-Kohn (HK) theorems in their seminal 1965 paper[56]. An efficient algorithm was provided in the following year by Kohn and Sham[57]. At the heart of DFT is the electron density $n(\vec{r})$, a 3-dimensional quantity that is, as will be shown in the following sub-sections, a unique characteristic of a system and a direct path to its Hamiltonian from which all other properties are accessed.

2.2.1. First HK Theorem

For a given system, there exists a one-to-one correspondence between the external potential $v(\vec{r})$ and the non-degenerate ground state electron density $n(\vec{r})$. The proof follows from the contradicting assumption that two external potentials, $v(\vec{r})$ and $v'(\vec{r})$, corresponding to ground states Ψ and Ψ', exist, differ by more than a constant, and give rise to a single charge density $n(\vec{r})$. Then, from eqs. 2.4, 2.6, and 2.10, and

$$\int \Psi^*(\vec{r})\Psi(\vec{r})d\vec{r} = \int \Psi'^*(\vec{r})\Psi'(\vec{r})d\vec{r} = n(\vec{r}) \tag{2.22}$$

we get

$$E < \langle\Psi'|\hat{H}|\Psi'\rangle = \int v(\vec{r})n(\vec{r})d\vec{r} + \langle\Psi'|\hat{T}_e + \hat{V}_{ee}|\Psi'\rangle = E' + \int [v(\vec{r}) - v'(\vec{r})]n(\vec{r})d\vec{r} \tag{2.23}$$

$$E' < \langle\Psi|\hat{H}'|\Psi\rangle = \int v'(\vec{r})n(\vec{r})d\vec{r} + \langle\Psi|\hat{T}_e + \hat{V}_{ee}|\Psi\rangle = E + \int [v'(\vec{r}) - v(\vec{r})]n(\vec{r})d\vec{r} \tag{2.24}$$

The sum of eqs. 2.23 and 2.24 results in the following contradiction

$$E + E' < E' + E \tag{2.25}$$

Thus, by *reductio ad absurdum*, it is shown that the charge density $n(\vec{r})$ is uniquely connected to the external potential $v(\vec{r})$. Since

$$\int n(\vec{r})d\vec{r} = N \tag{2.26}$$

the charge density uniquely determines both N and $\widehat{H}$, and, through eq. 2.1, provides access to all ground state properties of the system.

2.2.2. Second HK Theorem

With the one-to-one correspondence at hand, we can now express the total energy of the electronic system as a functional of the unique charge density $n(\vec{r})$

$$E[n] = T_e[n] + V_{ee}[n] + V_{ne}[n] = F_{HK}[n] + \int v(\vec{r})n(\vec{r})d\vec{r} \tag{2.27}$$

$$F_{HK}[n] = T_e[n] + V_{ee}[n] \tag{2.28}$$

explicitly defining the universal functional $F_{HK}[n]$, independent of the external potential $v(\vec{r})$ and true for any system. By varying the energy functional against all N-conserving densities (eq. 2.26), we obtain the ground state energy E_0

$$E_0 = \min_{n(\vec{r})} E[n] \tag{2.29}$$

and thus, the corresponding ground state density $n_0(\vec{r})$. The minimization process proceeds in two consecutive steps. In the first, one fixes a trial density $\tilde{n}(\vec{r})$ and varies $E[\tilde{n}]$ against the set of all trial wavefunction $\{\tilde{\Psi}\}$

$$E = \min_{\tilde{\Psi}} E[\tilde{n}] = \int v(\vec{r})\tilde{n}(\vec{r})d\vec{r} + F[\tilde{n}] \tag{2.30}$$

$$F[\tilde{n}] = \min_{\tilde{\Psi}} \langle \tilde{\Psi} | \hat{T}_e + \hat{V}_{ee} | \tilde{\Psi} \rangle \tag{2.31}$$

where $\{\tilde{\Psi}\}$ lead to $\tilde{n}(\vec{r})$ from

$$\tilde{n}(\vec{r}) = N \int \tilde{\Psi}^*(\vec{r}, \vec{r}_2 \cdots \vec{r}_N)\tilde{\Psi}(\vec{r}, \vec{r}_2 \cdots \vec{r}_N) d\vec{r} \cdots d\vec{r}_N \tag{2.32}$$

In the second, eq. 2.30 is varied against all N-representable charge densities $\tilde{n}(\vec{r})$

$$E_0 = \min_{\tilde{n}(\vec{r})} E[\tilde{n}] \tag{2.33}$$

thus reducing the $3N$-dimensional minimization problem to one of only three. If the universal functional $F[n]$ was explicitly known, the total ground state energy of the system would be exactly attainable. Nevertheless, the HK theorems are mathematically sound, and provide an exact formulation of the electronic-structure problem in terms of the charge density.

There remains the matter of expressing the kinetic energy in terms of the electron density. The early density functional theory of Thomas-Fermi (TF)[58,59] represented the kinetic energy $T[n]$ of an interacting electronic system as a sum over infinitesimal cells of constant $n(\vec{r})$ and $v(\vec{r})$. Each cell was approximated as a local uniform electron gas, and its contribution to the real inhomogeneous system was derived from fermion statistical mechanics[54]. The TF formulation, however, lacked the ability to accurately model molecular bonding in general, as it did not account for exchange-correlation interactions and treated kinetic energy locally[53]. To overcome this, Kohn and Sham reexamined the single-particle Hartree equations from the perspective of the formally exact HK theory.

2.2.3. Kohn-Sham Equations

The derivation of the Kohn-Sham (KS) equations can be done by comparison of the real system of interest and a fictitious non-interacting electronic system of the same charge density $n(\vec{r})$. In the absence of electronic interaction, the energy functional is given by

$$E[n] = T_s[n] + \int v(\vec{r})n(\vec{r})d\vec{r} \tag{2.34}$$

where $T_s[n]$ is the kinetic energy functional of the non-interacting fictitious system. Varying eq. 2.34 with respect all $n(\vec{r})$ constrained by eq. 2.26 yields

$$\delta E[n] = \int \delta n(\vec{r}) \left\{ v(\vec{r}) + \frac{\delta}{\delta n(\vec{r})} T_s[n] - \varepsilon \right\} d\vec{r} = 0 \tag{2.35}$$

where the Lagrange multiplier ε accounts for the conservation of particle number N. The Euler-Lagrange equations are then the Hartree equations (eq. 2.12)

$$\left\{ -\frac{1}{2}\nabla^2 + v(\vec{r}_i) \right\} \psi_i(\vec{r}_i) = \varepsilon_i \psi_i(\vec{r}_i) \tag{2.36}$$

with the mean-field potential $\hat{U}$ of eq. 2.14, given here in terms of $n(\vec{r})$, removed

$$v(\vec{r}) = v_H(\vec{r}) - \int \frac{n(\vec{r}')}{|\vec{r} - \vec{r}'|} d\vec{r}' \tag{2.37}$$

To construct similar single-electron Hartree-like equations, we then rewrite the energy functional of the real interacting system (eq 2.27) as follows

$$E[n] = T_s[n] + U[n] + E_{XC}[n] + \int v(\vec{r}) n(\vec{r}) d\vec{r} \tag{2.38}$$

with the kinetic energy $T_s[n]$ of the non-interacting system handled separately. The electron-electron interaction term $\hat{V}_{ee}$ is split into its classical Coulomb repulsion part through the Hartree mean-field approximation

$$U[n] = \frac{1}{2} \int \frac{n(\vec{r}) n(\vec{r}')}{|\vec{r} - \vec{r}'|} d\vec{r} \tag{2.39}$$

and quantum exchange-correlation part $E_{XC}[n]$ defined by eq. 2.38. Variationally minimizing eq. 2.38 with respect to the density function then yields

$$\delta E[n] = \int \delta n(\vec{r}) \left\{ v_{eff}(\vec{r}) + \frac{\delta}{\delta n(\vec{r})} T_s[n] - \varepsilon \right\} d\vec{r} = 0 \tag{2.40}$$

where the effective potential $v_{eff}(\vec{r})$ is given by

$$v_{eff}(\vec{r}) = v(\vec{r}) + \int \frac{n(\vec{r}')}{|\vec{r} - \vec{r}'|} d\vec{r}' + v_{XC}(\vec{r}) \tag{2.41}$$

$$v_{XC}(\vec{r}) = \frac{\delta}{\delta n(\vec{r})} E_{XC}[n] \tag{2.42}$$

By comparing the kernels of eqs. 2.35 and 2.40, we obtain the Euler-Lagrange equations of the real interacting system

$$\left\{-\frac{1}{2}\nabla^2 + v_{KS}(\vec{r}_i)\right\}\psi_i(\vec{r}_i) = \varepsilon_i \psi_i(\vec{r}_i) \tag{2.43}$$

with the Kohn-Sham $v_{KS}(\vec{r})$ being that effective potential defined in eq. 2.41. As the set of equations contained in eq. 2.43, referred to as the Kohn-Sham equations, are of the form of the single-particle Hartree equations, their solution follows a similar self-consistent cycle (fig. 2.1).

2.2.4. Exchange-Correlation Approximations

The Kohn-Sham procedure provides an efficient and practical algorithm for the exact HK theory. However, the formulation does not offer an explicit form for $E_{XC}[n]$. To proceed, one must select an approximation appropriate to the system at hand. In the next sections, the local density approximation (LDA), generalized gradient approximation (GGA), and the use of post-GGA hybrid functionals are discussed.

2.2.4.1. Local Density Approximation

In cases of slow varying density $n(\vec{r})$, or cases of high density where the kinetic energy dominates over the exchange and correlation energy, a good approximation of $E_{XC}[n]$ is given by

$$E_{XC}^{LDA}[n] = \int n(\vec{r}) \varepsilon_{XC}[n(\vec{r})] d\vec{r} \tag{2.44}$$

where $\varepsilon_{XC}[n]$ is the exchange-correlation energy per particle of a uniform electron gas of density $n(\vec{r})$ expressed as a sum of exchange $\varepsilon_X^{LDA}[n]$ and correlation $\varepsilon_C^{LDA}[n]$ terms[60]. Exchange energy is given by the Dirac exact exchange term[61]

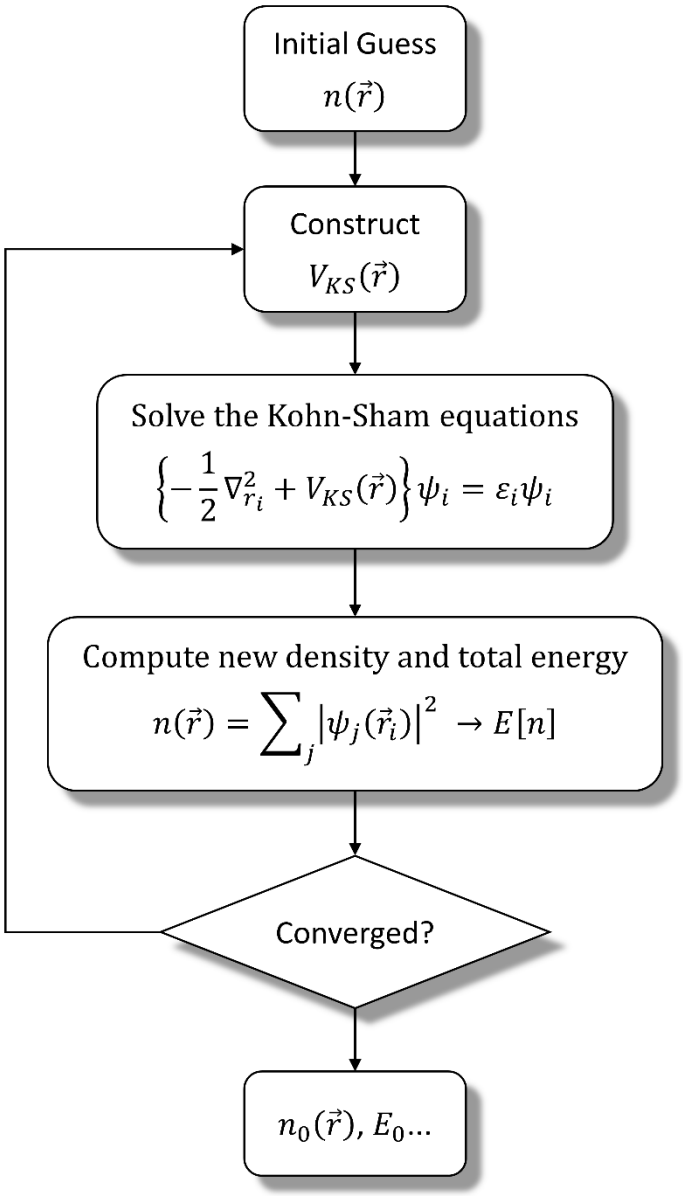

Figure 2.1. Kohn-Sham self-consistent cycle

$$\varepsilon_X^{LDA}[n] = -\frac{3}{4}\left(\frac{3}{\pi}\right)^{1/3}\int n(\vec{r})^{4/3}d\vec{r} = \frac{0.458}{r_s} \tag{2.45}$$

where r_s is the Wigner Seitz radius given by $4/3\pi r_s^3 = n^{-1}$. The correlation term is written with respect to high and low density limits as[62]

$$\varepsilon_C^{LDA}[n] = \begin{cases} \mathrm{A}\ln r_s + \mathrm{B} + r_s(\mathrm{C}\ln r_s + \mathrm{D}) & \text{for } r_s \ll 1 \\ \frac{1}{2}\left(\frac{g_0}{r_s} + \frac{g_1}{r_s^{3/2}} + \frac{g_2}{r_s^2} + \cdots\right) & \text{for } r_s \gg 1 \end{cases} \tag{2.46}$$

where the coefficients are parameterized by fitting to quantum Monte Carlo simulations[53]. For a spin-polarized system, the local (spin) density approximation (LSDA) is given by

$$E_{XC}^{LSDA}[n_\alpha, n_\beta] = \int n(\vec{r})\varepsilon_{XC}[n_\alpha(\vec{r}), n_\beta(\vec{r})]d\vec{r} \tag{2.47}$$

with an exact and straightforward extension of the exchange term[63]

$$\varepsilon_X^{LSDA}[n_\alpha, n_\beta] = \frac{1}{2}\left(\varepsilon_X[2n_\alpha] + \varepsilon_X[2n_\beta]\right) \tag{2.48}$$

and further approximation of the correlation term via a relative polarization function. Though most systems differ significantly from the slow-varying homogeneous electron gas model, LDA has yielded surprisingly good results. This is partially due to its tendency to overestimate E_x, but underestimate E_c, resulting in partial error cancelation[64].

2.2.4.2. Generalized Gradient Approximation

To account for (local) spatial variations in an inhomogeneous charge density that surpass the limits of LDA, we could apply a power-series expansion to $\varepsilon_{XC}[n]$ in terms of gradients of $n(\vec{r})$[65]. However, gradient-expansion approximations (GEA) in general are not successful, as low-order terms do not improve on LDA results, and higher-order terms are difficult to determine and

are thus not considered. Instead, in the generalized gradient approximation (GGA), one employs general functions of the density $n(\vec{r})$ and its gradients $\nabla n(\vec{r})$

$$E_{XC}^{GGA}[n_\alpha, n_\beta] = \int f\left(n_\alpha(\vec{r}), n_\beta(\vec{r}), \nabla n_\alpha(\vec{r}), \nabla n_\beta(\vec{r})\right) d\vec{r} \tag{2.49}$$

where the functional forms of $f(n, \nabla n)$, which only considers the first-order gradient expansion, can be conveniently developed through parameter fitting to experimental data and consideration of physical constraints. In the present dissertation, all calculations employ the parameterization of Perdew-Burke-Ernzerhof (GGA-PBE)[66], a simplified derivation of the gradient-corrected functional which focuses on those features of real systems that are energetically significant. The PBE functional alleviates the major limitations of its predecessors. For example, the earlier PW91 GGA functional[67], which attempted to satisfy as many properties of the exact E_{XC} as possible, had a tendency of performing worse than L(S)DA in homogeneous systems[68–70]. The PBE functional is less restrictive, as it only aims to capture the most significant properties of E_{XC}. GGA-PBE yields better energies and structure geometries than L(S)DA. Nevertheless, GGA functionals in general tend to overestimate lattice parameters due to overcorrections with respect to L(S)DA[71].

2.2.4.3. Hybrid Functional

It is well-known that both L(S)DA and GGA functionals underestimate the fundamental band gap. In KS theory, each electron feels a coulombic interaction with the mean electronic density (eq. 2.39), giving rise to self-interaction energy errors[72]. Such errors tend to delocalize electrons and lead to poor descriptions of electron correlation effects[73], especially in highly correlated transition metal systems. One approach to this problem, based on the adiabatic connection approximation in quantum mechanics[74], is to employ a hybrid functional which includes some amount of HF exact exchange. The hybrid functional is expressed as

$$E_{XC}^{hyb} = \alpha E_X^{HF} + (1-\alpha)E_X^{GGA} + E_C^{GGA} \tag{2.50}$$

where α is a fitting parameter. The standard use of GGA exchange and correlation terms in eq. 2.50 is due to reduced errors in atomization energies compared to L(S)DA. In appendix C, hybrid calculations used for comparison against GGA-PBE employ the screened coulomb potential hybrid functional of Heyd-Scuseria-Ernzerhof (HSE06)[75]. Here, the DFT portion of eq. 2.50 uses GGA-PBE exchange and correlation terms. Screening is achieved by splitting the functional into short (SR) and long range (LR) components (parameterized by ω)

$$E_{XC}^{HSE06} = \alpha E_X^{HF,SR} + (1-\alpha)E_X^{PBE,SR}(\omega) + E_X^{PBE,LR}(\omega) + E_C^{PBE} \tag{2.50}$$

neglecting the weak contributions from long-range HF and PBE terms. The inclusion of exact HF exchange in the hybrid functional methodology often improves the accuracy of the electronic structure for non-metals, though at the cost of significantly more computational resources.

2.3. DFT+U

An alternative method of handling the poor accounting of correlation energies in DFT is to introduce Hubbard-like on-site interaction terms that act only on those localized, highly correlated electrons of angular momentum l – usually 3d or f electrons. The general functional form of DFT+U is written as[76]

$$E_{DFT+U}[n] = E_{DFT}[n] + E_{Hub}\left[\{\rho_{mm'}^{i\sigma}\}\right] - E_{dc}\left[\{\rho^{i\sigma}\}\right] \tag{2.51}$$

where E_{DFT} is the DFT functional given in eq. 2.38. E_{Hub} is the on-site energy obtained from the Hubbard Hamiltonian which treats the motion of localized electrons as a hopping mechanism balanced between a bandwidth-dependent amplitude term and a Coulomb repulsion term proportional to the occupation number $\rho^{i\sigma}$ on the i^{th} site. The strength of the latter is determined by the Hubbard U parameter. E_{dc} is a double-counting term that corrects for those terms in E_{Hub} already included in DFT. The occupation numbers $\rho_{mm'}^{i\sigma}$ of electrons of spin σ and magnetic moment m localized

about the i^{th} atom are defined as projections of the occupied KS orbitals onto a localized basis set. In the present dissertation, the DFT+U formalism developed by Dudarev[77] is considered, where the on-site terms U (coulomb) and J (exchange) are introduced as a single effective parameter $U_{eff} = U - J$. The DFT+U functional is then written as[78]

$$E_{DFT+U}[n] = E_{DFT}[n] + \frac{\bar{U} - \bar{J}}{2} \sum_{\sigma} \left[\left(\sum_{m} \rho_{m}^{i\sigma} \right) - \left(\sum_{m,m'} \hat{\rho}_{mm'}^{i\sigma} \hat{\rho}_{m'm}^{i\sigma} \right) \right] \tag{2.52}$$

where the Hubbard terms $\bar{U}$ and $\bar{J}$ are given as spherical averages. The second term on the right hand side is generally interpreted as a penalty function which drives the occupancy matrix at i^{th} site towards idempotency – $\hat{\rho}^{i\sigma} = \hat{\rho}^{i\sigma}\hat{\rho}^{i\sigma}$. Resultant integer occupancies effectively shift the energy of occupied localized orbitals by $(\bar{U} - \bar{J})/2$, which leads to an increase in band gap energies.

In general, the DFT+U approach is computationally cheaper than the use of hybrid functionals. This often allows the study of larger systems with a more accurate description of the electronic structure. The Hubbard terms can be determined from first principles calculations, though they are often established semi-empirically. In the present dissertation, the DFT+U methodology is used in chapters 5 and 6 to ensure consistency and comparability with previous theoretical results. Effective U values are given with respect to $J = 1$.

2.4. Plane-wave Mechanics

In solid-state calculations, it is convenient to recast the KS equations as a Fourier expansion in a complete plane-wave basis set. This offers formal simplicity, requires a single basis-set for all species, and allows for efficient calculation of Hellman-Feynman forces[79–81]. The periodic distribution of atoms in a solid crystal gives rise to a periodic potential $V(\vec{r})$ that is invariant to translations of lattice vector $\vec{R}$

$$V(\vec{r} + \vec{R}) = V(\vec{r}) \tag{2.53}$$

Bloch's theorem states that single-electron solutions of a periodic Hamiltonian can be expressed as products of a plane wave and a periodic function[82]

$$\psi_{n\vec{k}}(\vec{r}) = u_n(\vec{r})e^{i\vec{k}\cdot\vec{r}} \tag{2.54}$$

$$u_n(\vec{r} + \vec{R}) = u_n(\vec{r}) \tag{2.55}$$

Applying a lattice vector translation to any solution of the form of eq. 2.54 then yields

$$\psi(\vec{r} + \vec{R}) = u(\vec{r} + \vec{R})e^{i\vec{k}\cdot(\vec{r}+\vec{R})} = \left[u(\vec{r})e^{i\vec{k}\cdot\vec{r}}\right]e^{i\vec{k}\cdot\vec{R}} = \psi(\vec{r})e^{i\vec{k}\cdot\vec{R}} \tag{2.56}$$

where eq. 2.55 has been applied. The wave vector $\vec{k}$ is limited to the primitive reciprocal space cell, or first Brillouin zone. Any $\vec{k}'$ outside of the first Brillouin zone can always be expressed as the sum $\vec{k} + \vec{G}$, where $\vec{G}$ is a reciprocal lattice vector defined through $\vec{G} \cdot \vec{R} = 2\pi m$. The periodic boundary conditions force $\vec{k}$ to be real, thus ensuring a conservation of probabilities in all repeating cells, where solutions may be obtained via application of eq. 2.56. Thus, all information associated with the electronic system is confined to the first Brillouin zone. Integrations over the infinite k-point set within the first Brillouin zone can be replaced with discrete summations over a finite "special" set due to the slow variation of the wavefunction with respect to small translations in reciprocal space. Present calculations make use of the scheme developed by Monkhorst and Pack[83], where k-points are distributed uniformly within the volume of the reciprocal cell. The k-point grid is further reduced by removing redundant k-points using operations based on the symmetry of the reciprocal cell. The size of the grid is then converged against variations in total energy to ensure proper k-point sampling of the Brillouin zone.

Following the periodicity of eq. 2.55, we expand $u(\vec{r})$ in a Fourier series

$$u_n(\vec{r}) = \sum_{\vec{G}} c_{n,\vec{G}} e^{i\vec{G}\cdot\vec{r}} \tag{2.57}$$

and by extension, the KS orbitals can be written as Bloch functions

$$\psi_{n\vec{k}}(\vec{r}) = \sum_{\vec{G}} c_{n,\vec{k}+\vec{G}} e^{i(\vec{k}+\vec{G})\cdot\vec{r}} \tag{2.58}$$

Substituting eq. 2.58 into eq. 2.43 yields the plane-wave form of the KS equations

$$\sum_{\vec{G}} \left[\frac{1}{2}\left|\vec{k}+\vec{G}\right|^2 \delta_{\vec{G},\vec{G}'} + V_{eff}\left(\vec{G}-\vec{G}'\right) \right] c_{n,\vec{k}+\vec{G}} = \varepsilon_n c_{n,\vec{k}+\vec{G}} \tag{2.59}$$

where $V_{eff}(\vec{G})$ is the reciprocal space form of the KS effective potential (eq. 2.41). The problem is then reduced to solving self-consistently for the expansion coefficients $\{c_{n,\vec{k}+\vec{G}}\}$. Solving eq. 2.59 is made efficient through the use of Fast Fourier Transform (FFT) algorithms. In practice, the infinite series in eq. 2.59 is truncated by assigning a limit on the kinetic energy of plane-waves

$$\frac{1}{2}\left|\vec{G}_{max}\right|^2 < E_{cut} \tag{2.60}$$

noting that terms with higher kinetic energy typically play a reduced role in modeling the KS orbitals. This also suggests that the quality of the basis set can be tested for convergence via a single parameter, namely E_{cut}.

Near nuclei, the wavefunction oscillates widely due to the strong attractive potential. To capture these oscillations would require a large plane-wave set, or a large value of E_{cut}. Alternatively, noting that core states are far less involved in chemical reactions and thus largely retain their atomic nature, the potential near the core of nuclei can be substituted for an approximated potential. This pseudopotential is norm-conserving, ensuring the correct total charge within the core region defined by the cutoff radius r_c. It is constructed in such a way that eliminates the nodal structure of $\psi(r)$ for $r < r_c$, and is identical to the plane-wave expanded wavefunction outside of

the core region at $r > r_c$. The pseudopotential then leads to a smooth function across the $r = r_c$ core-valence boundary and allows calculations to proceed with a far smaller basis set that is practical on modern machines. Calculations within the present dissertation make use of the Projector Augmented Wave (PAW) formalism[84], in which the accuracy of an all-electron (AE) plane-wave basis set and the efficiency of the pseudopotential (PS) approximation are unified. Valence plane-waves outside an element-specific spherical radius are mapped onto a linearly transformed Hilbert space via so-called projector functions $|p_i\rangle$, resulting in a new basis set of AE-like wavefunctions.

2.5. Electronic Structure Determination

In the present dissertation, several methods are used to explore the electronic structure of a system. These are post-processing techniques applied to the pre-converged ground state density obtained from the Kohn-Sham self-consistent cycle. Standard analyses of the electronic structure typically involve the density of states (DOS) and an $E(\vec{k})$ diagram. The latter is commonly referred to as the band structure and is a plot of the KS eigenvalues along selected paths between special high symmetry k-points in the first Brillouin zone. The DOS and the band structure together provide insight into the environment in which electrons move. For semiconductors, they generally feature a distinct gap between the occupied valence band and unoccupied conduction band. The density of states can be decomposed into individual orbital contributions. This partial, or projected density of states (PDOS) is used to better understand chemical bonding and orbital transitions. Furthermore, the dispersion, or curvature of bands in band structures can be used to determine the effective mass m^* of charge carriers via[85]

$$\frac{1}{m^*} = \frac{1}{\hbar^2}\frac{\partial^2 E}{\partial k^2} \tag{2.61}$$

where the curvature is evaluated at band extrema using finite difference methods. The charge carrier mobility μ is related to the effective mass through

$$\mu = \frac{q\bar{\tau}}{m^*} \tag{2.62}$$

where q is negative for electrons and positive for holes, and $\bar{\tau}$ is the average scattering time[86]. The conductivity σ of a material is obtained from carrier mobilities through

$$\sigma = |e|(n\mu_e + p\mu_h) \tag{2.63}$$

where n and p are respectively the carrier concentrations of electrons (e) and holes (h), and e is the elementary charge. Eqs. 2.62 and 2.63 are given here for completeness. In the present dissertation, conductivity and mobility are not explicitly calculated. Comments regarding the transport properties of a material are limited to variations in the effective masses of its charge carriers, with lighter charge carriers considered as more mobile.

Most electronic properties can be understood from the perspective of charge distribution and charge transfer. Three analytic tools are employed in the present dissertation to explore these properties. The first is a charge analysis developed by Bader[87] that considers the solid system as the sum of quantum subsystems partitioned by zero-flux surfaces along which the density gradients vanish. Net charge is obtained for an atom by integrating over its respective region of density, or basin, and subtracting the result from the nuclear charge. Furthermore, oxidation states may be approximated by subtracting the Bader net charge from the considered number of valence electrons determined by the PAW definition for the atom. For example, the PAW-defined valence electron configuration for oxygen used in present calculations is $2s^2 2p^4$ – a total of 6 electrons. Typical Bader net charges for oxygen may fluctuate about 7, suggesting an O^{-1} oxidation state.

Another method for studying charge transfer in a system is to plot the difference of the total ground state density n_0 and the densities n_x of the constituent atoms

$$\Delta n = n_0 - \sum_x n_x \tag{2.64}$$

where n_x is obtained from a separate calculation on a unit cell containing only species x in its ground state coordinates. The level of theory used in these calculations matches that which obtained the ground state density to ensure transferability. Δn gives a representation of those atomic interactions which led to the chemical bonding observed in n_0.

Lastly, n_0 may be decomposed onto various energy bands of high interest to reveal the various atomic orbital contributions; the band decomposed charge density plot is, in essence, an enhanced multidimensional picture of the DOS and is often analyzed against it to better understand the electronic structure. In the present dissertation, both band decomposed charge density plots and charge difference plots are visualized in VESTA[88].

Chapter 3

Crystal Symmetry and d-orbital Effects

Introductory Comments

The following article explores the stibiotantalite mineral, or $Sb(Ta,Nb)O_4$, in three common ns^2-md^0 crystal symmetries – tetragonal, orthorhombic, and monoclinic. In each crystal phase, the d-orbital character is varied through gradual Nb-in-Ta substitutions. It is shown that crystal phase effects and d-orbital effects are, for the most part, independent of each other. The presence of Nb 4d electrons primarily affects the conduction bands, downshifting the CBM and modifying its band dispersion. The degree of VBM upshift as a result of ns^2 – O 2p hybridization is attributed to differences in crystal structure between the three phases. Favorable band gap and band edge properties are found in the less stable phases, highlighting the complexity and difficulty in matching all the necessary requirements of an efficient PEC material.

ELECTRONIC PROPERTIES OF $SbTa_{1-x}Nb_xO_4$: PHASE-RELATED DISTORTIONS

Edan Bainglass
Muhammad N. Huda

Bainglass, E. & Huda, M. N. Electronic properties of $SbTa_{1-x}Nb_xO_4$: Phase-related distortions. J. Electrochem. Soc. 166, H3195–H3201 (2019).

© Bainglass, E. & Huda, M. N. 2019. Published by ECS. Reproduced by permission of IOP Publishing. CC BY-NC-ND

Electronic Properties of $SbTa_{1-x}Nb_xO_4$: Phase-Related Distortions

E. Bainglass and M. N. Huda

Department of Physics, The University of Texas at Arlington, Arlington, TX 76019, USA

Abstract

We have studied the effects of structural symmetry related distortions on the band gaps and overall energetics of $SbMO_4$ compounds (M = Ta, Nb). Evolution of the electronic structures was studied as one transitions gradually from a system of 4d bands to 5d bands, and whether this has any effect on the Sb oxidation state or its lone pair *s* electrons. From the atomic point of view, electronic correlation energy is higher in Ta 5d than in Nb 4d, and Nb 4d bands are higher in energy than Ta 5d. These were examined in terms of oxidation states in their respective solids and mixed alloys. We look at the effects of increasing Nb concentration on the electronic structures of $SbTa_{1-x}Nb_xO_4$ alloys with emphasis on polyhedral interactions and overall cell distortions. We de-couple the effects caused by the presence of different *n*d cations from those caused by distortions and reorientation of various polyhedra.

3.1. Introduction

It has been suggested that due to strong band dispersion, the ns^2-md^0 transition metal oxide group is favorable for water-splitting photocatalysis[27,89]. Hybridization of valence-dominating O 2p orbitals with transition metal md^0 cation orbitals suggests that these oxides are likely to form large-polarons which exhibit relatively high charge carrier motilities. In addition, s-p and p-d orbital interactions at the valence and conduction bands, respectively, strongly influence band edge positions, a critical factor in the water-splitting reaction[90]. The strength of such interactions is heavily governed by the crystal structure[91,92]. Thus, it is expected that structural distortions will play a crucial role in determining the electronic properties.

Mixed valence Sb_2O_4 compounds are widely used as catalysts in oxidations of hydrocarbons[93]. Among two of its phases, orthorhombic α-Sb_2O_4 and monoclinic β-Sb_2O_4, α-Sb_2O_4 is more stable. However, when α-Sb_2O_4 transforms into β-Sb_2O_4, the latter rarely transforms back. A recent study proposed that this is due to the kinetic barrier rather than thermodynamics[94]. In earlier literature, both $SbTaO_4$ and $SbNbO_4$ in the orthorhombic α-Sb_2O_4 phase have demonstrated pure water splitting as photocatalysts, albeit under UV light, due to their higher band gap[95]. In fact, $SbTaO_4$ was found to be twice as more active in producing hydrogen than $SbNbO_4$. The presence of d electrons has been shown to increase electron carrier concentration and reduce electronic effective mass[96]. These effects result from the lower energy of d electrons and the structural distortion they incur.

The overarching goal of our study is to design or predict materials for solar energy conversion. In this pursuit, the purpose of this study is to investigate the effects of structural symmetry related distortions on the band gaps and overall energetics of these systems. In the current work, we have studied SbMO$_4$ compounds (where M = Ta, Nb replaces the Sb^{5+} cation) in the orthorhombic α-Sb_2O_4 phase, as well as in tetragonal and monoclinic phases. In the parent orthorhombic SbMO$_4$, MO_6 octahedra are connected to each other by sharing four corners. On the other hand, highly distorted SbO_6 octahedra are found to be edge sharing to each other. This layer-by-layer $M^{5+}O_6 - Sb^{3+}O_6$ structure in general gives rise to the ferroelectric behavior for these class of materials due to the net dipole moment in the unit cell[97–99]. Photoferroelectrics[100] have been shown to promote charge separation due to polarization-induced microscopic electric fields[97].

Tetragonal to orthorhombic to monoclinic transitions will further distort the MO_6 octahedra, which affect the M nd electrons/bands (n = 4 and 5 for Nb and Ta, respectively). Therefore, in addition, we will study how the electronic structures evolve as one transitions from a system of

5d bands to 4d bands, and whether this has any effect on the Sb oxidation state or its lone pair *s* electrons.

The pnictogen group (VA) is generally found in a 5+ oxidation state, though Sb^{3+} is commonly observed. For example, the stibiotantalite mineral[101], or $SbTaO_4$, is formed by substituting Ta in the Sb^{5+} site of mixed-valence, orthorhombic α-Sb_2O_4 (fig. 3.1). The resulting $Sb^{3+}Ta^{5+}O^{-2}{}_4$ material belongs to the aforementioned ns^2-md^0 transition metal oxide group. An important point to note, ionic (5+) radii of both Ta and Nb are equal despite Ta having 32 more electrons than Nb. This implies that the size effect due to Ta and Nb in a crystal structure will be similar. However, the electronegativity of Nb is slightly higher than Ta, and the valence electrons are more bound in Ta than Nb, as evident from their first atomic ionization potentials. This implies that as Ta is replaced by Nb, the valence band will upshift in energy and will potentially reduce the band gap. We will examine these issues in the respective solids. Understanding this phenomenon is necessary to predict new alloys involving these systems with suitable band gaps and with desirable photocatalytic and optoelectronic properties.

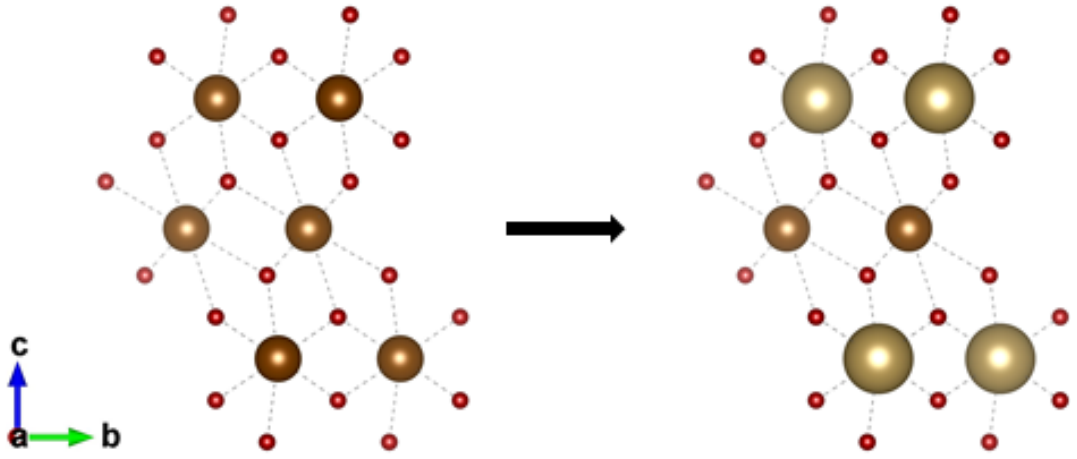

Figure 3.1. Ta substitution in Sb 5+ sites of α-Sb_2O_4. Sb shown in brown (medium); Ta shown in green (large); O shown in red (small).

3.2. Methodology

3.2.1. Computational Methods

Density functional theory (DFT)[56,57] is utilized in calculations of total energies, density of states, and band structures. Exchange-correlation effects are handled by the general gradient approximation (GGA), within the Perdew-Burke-Ernzerhof (PBE) formalism[66,67]. Wave functions are expanded in plane waves, and core electrons for Sb[Kr]{4d}, Ta[Kr]{5s,4d}, and Nb[Ar]{3d} are treated with the projector augmented wave (PAW) method[84,102], as implemented in the Vienna *ab initio* Simulation Package (VASP 5.4.4)[103,104]. A Monkhorst-Pack[83] k-point mesh of 7 × 7 × 3 was used for the tetragonal and orthorhombic phases, while a mesh of 7 × 3 × 11 was used for the monoclinic phase. These grids are chosen in accordance with the shapes of their respective real-space lattices. Density of states (DOS) plots are calculated at finer k-point meshes of 9 × 9 × 5 and 9 × 5 × 13, respectively. All calculations were performed with a plane wave cutoff threshold of 600 eV. Both the k-point grids and the cutoff value were converged within total energy differences of 1 meV. Geometry optimizations are performed without symmetry constraints to an ionic force cutoff of 0.01 eV/Å. Band structure calculation and geometry optimization are done using the 2nd order Methfessel-Paxton method[105]. Total energies and density of states are calculated using the tetrahedron method[106].

We note that under this methodology, band gaps are known to be underestimated. This is exacerbated in d-electron systems due to an underestimation of electron correlation[73,107,108]. The corrective DFT+U methodology is avoided at the current stage, as we focus primarily on the energetic trend among the three Sb*M*O$_4$ phases, rather than absolute band gap energies. Moreover, the DFT+U method is more pertinent to the 3d transition metal systems where partially filled d-bands are more localized. For example, Ersoy et al.[109] clearly shows that on-site Coulomb

interaction for 3d transition metals is significantly higher than that of 4d and 5d transition metals. Thus, we work under the assumption that the energetic trend should not be affected by the under-estimation due to the similar compositions of the phases.

Cohesive energies are calculated as

$$E_{cohesive} = E(SbMO_4) - nE(Sb) - mE(M) - \frac{l}{2}E(O_2) \quad (3.1)$$

where $n = m = 4$, and $l = 8$, for all SbMO$_4$ phases. These energies represent the binding of solids with respect to the free, lowest energy spin configuration states of their constituent atoms. According to this formula, more negative values imply higher stability. Unit cell and charge density visualizations are done in VESTA[88]. Special Brillouin zone symmetry points are obtained from AFLOW[110].

Bader charge analyses[87] are performed using code provided by the Henkelman group[111–114]. Bader net charges are defined as

$$Q_{net} = Q_{VASP} - Q_{Bader} \quad (3.2)$$

where Q_{VASP} is the valence charge considered in the calculation, and Q_{Bader} the calculated Bader atomic charge. Net charges serve as a guide for the oxidation states of the corresponding atoms. Due to the approximations in the Bader charge analysis methodology, deviations from the $Sb^{3+}Ta^{5+}O^{-2}_4$ states are to be expected. In addition, not all metal-oxygen bonds are purely ionic. However, trends in deviation magnitudes can still be of use. We consider these deviations as a measure of ionicity, where the $Sb^{3+}Ta^{5+}O^{-2}_4$ ideal oxidation states represent a pure ionic limit.

3.2.2. Symmetry Groups

A route of reduced-symmetry can be seen in the distortion from tetragonal to orthorhombic, and finally down to the monoclinic structure. Both tetragonal and orthorhombic crystal structures exhibit 90° angles throughout. The difference between the two systems lies in their basal planes,

where a = b ≠ c for tetragonal, and a ≠ b ≠ c for orthorhombic. The orthorhombic system is then a direct distortion from the tetragonal system, in which the basal square planes are distorted towards rectangular planes, losing all 90° rotation symmetry[115]. Further distortion of a single 90° angle of the orthorhombic system results in a monoclinic structure, in which a ≠ b ≠ c and $\alpha = \beta = 90°$; $\gamma \neq 90°$.

The orthorhombic phases of all Sb*M*O_4 compounds studied here, referred to as o-Sb*M*O_4, are modeled on the stibiotantalite mineral[101] (fig. 3.2a). The tetragonal and monoclinic phases of $BiVO_4$ – Scheelite[116,117] and Clinobisvanite[118], respectively – are used as templates for the corresponding symmetry structures of the Sb*M*O_4 group, or t-Sb*M*O_4 and m-Sb*M*O_4 (fig. 3.2b & 3.2c). The Dreyerite[119] and Pucherite[120] phases of $BiVO_4$ – tetragonal and orthorhombic, respectively – as well as a monoclinic polymorph of $BiNbO_4$[121], were also calculated, but were at higher energies with respect to the structures of Figure 3.2. To establish motivation for the current study, we first briefly discuss some results on these Sb*M*O_4 compounds from the literature.

3.3. Background

XRD patterns of solid-state-reaction-produced stibiotantalite compounds, or Sb(Ta,Nb)O_4, have found the systems in the orthorhombic phase of space group $Pna2_1$, with {a, b, c} = {5.542, 4.918, 11.823 Å} for $SbTaO_4$, and {a, b, c} = {5.568, 4.938, 11.811 Å} for $SbNbO_4$[95]. These results agree well with other previous experimental efforts[122,123]. Estimated band gaps from UV-Vis data were found at 3.72 eV and 3.12 eV for $SbTaO_4$ and $SbNbO_4$, respectively. A subsequent DFT analysis showed that distortions in the orientation of TaO_6 octahedra as compared to NbO_6 in their respective cells affect the band structures of the two compounds, with a larger band gap of 4.1 eV found in $SbTaO_4$ compared to 3.9 eV in $SbNbO_4$. Both gaps were found to be indirect. As is typical in metal oxides[29], valence bands in both compounds were found to be dominated by O 2p states.

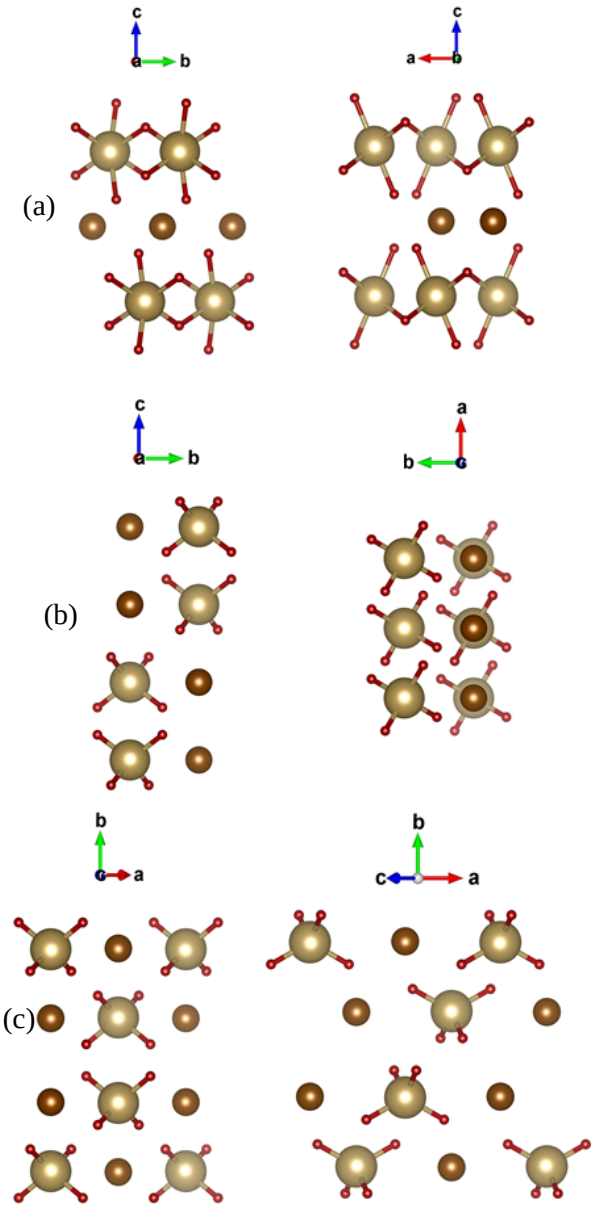

Figure 3.2. Initial geometries used for SbMO_4 compounds. (a) The Stibiotantalite mineral for o-SbMO_4, (b) Scheelite $BiVO_4$ for t-SbMO_4, and (c) Clinobisvanite for m-SbMO_4. Bonds are shown for MO polyhedra to highlight the various orientations. Sb shown in brown (medium); Ta shown in green (large); O shown in red (small).

A contribution from weak Sb 5s – O 2p hybridization was also observed at the top of the valence band. The overestimation of the calculated gaps with respect to UV-Vis estimated gaps was probably due to the implementation of higher percentage of Hartree-Fock exchange than was necessary as part of their hybrid functional.

A previous DFT study found an indirect gap of 1.9 eV for $SbTaO_4$[124] and references an experimental value of 2.28 eV[125]. Experimental lattice parameters of {a, b, c} = {5.540, 4.906, 11.807 Å}[122] were used for the calculation in ref. 124, though it is unclear if the unit cell was further relaxed under the employed GGA-PBE method. The author of ref. 95 argues that this lower value is caused by phase purity and surface defects. Nevertheless, the contrasting results of ref. 95 and ref. 124 raise a question, as varying amounts of Hartree-Fock exchange contribution may lead to overestimated values in ref. 95; and the relaxation of the highly ionic octahedra of SbTaO4 will influence the gap as well. In addition, experimental results are also questionable in regard to the phase purity of their sample, and thus require further investigation as well.

Lastly, mixed $SbTa_{1-x}Nb_xO_4$ alloys have been shown to exhibit the orthorhombic stibiotantalite structure of the same space group[126]. This is to be expected due to the proximity in atomic radii values of Ta^{5+} an Nb^{5+}. In the current study, we look at the effects of increasing Nb concentration on the electronic structure of $SbTa_{1-x}Nb_xO_4$, with emphasis on polyhedral and overall cell distortions. We decouple the effects caused by the presence of different *n*d cations from those caused by distortions and reorientation of Sb-polyhedra.

3.4. Results & discussion

3.4.1. Structural Analysis

Final GGA relaxed structures for $SbTa_{1-x}Nb_xO_4$ (x = 0, 0.25, 0.5, 0.75, 1) are found in the following space groups: (i) $I4_1/a$ for tetragonal; (ii) $Pbn2_1$ for orthorhombic; and (iii) C2/c for monoclinic (fig. 3.3). Calculated lattice constants and cell volumes are given in Table 3.1. Percent errors in o-$SbTaO_4$ lattice constants are about ~2% from the experimental results of ref. 122, and are to be expected from GGA calculations[127]. For both x = 0.25 and 0.75, there exists only one

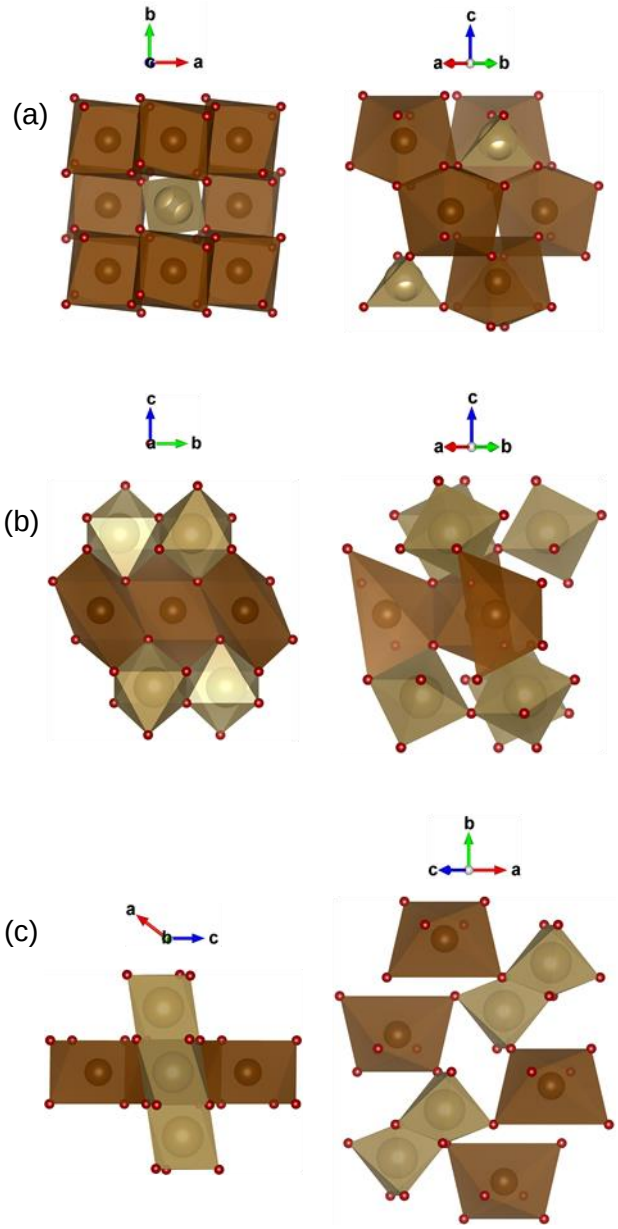

Figure 3.3. Final GGA relaxed $SbTaO_4$ unit cells. Several orientations are shown for (a) t-$SbTaO_4$, (b) o-$SbTaO_4$, and (c) m-$SbTaO_4$. Atoms are shown for Sb in brown (medium), Ta in green (large), and O in red (small). *M*O polyhedra are shown in green (light gray); SbO Polyhedra are shown in brown (dark gray).

unique configuration. For x = 0.5, the configuration with Nb-substitutions in adjacent *M*O polyhedra exhibits lower energy than the configuration with Nb-substitutions in opposing, disconnected *M*O polyhedra. Subsequent analyses refer to the lower energy configuration.

Table 3.1. Lattice parameters and cell volumes for relaxed $SbTa_{1-x}Nb_xO_4$ compounds. Lattice parameters are given in Å. Cell volumes are in $Å^3$. T –tetragonal; M – monoclinic; O – orthorhombic

x	Phase	$\boldsymbol{a}$	$\boldsymbol{b}$	$\boldsymbol{c}$	$\boldsymbol{V_{cell}}$
	T	5.282	5.282	11.180	311.953
0	O	5.018	5.624	11.977	338.014
	M	8.167	11.276	5.744	321.830
	T	5.280	5.280	11.176	311.597
0.25	O	5.024	5.631	11.974	338.697
	M	8.150	11.277	5.735	321.145
	T	5.278	5.278	11.190	311.751
0.5	O	5.030	5.637	11.969	339.424
	M	8.143	11.279	5.730	320.813
	T	5.275	5.275	11.192	311.446
0.75	O	5.035	5.645	11.961	339.962
	M	8.129	11.287	5.722	320.475
	T	5.275	5.275	11.207	311.789
1	O	5.042	5.654	11.950	340.674
	M	8.117	11.288	5.714	319.900

The tetragonal phase is highly symmetric, with near-perfect MO_4 tetrahedra, and SbO_8 polyhedra only slightly distorted from a biaugmented triangular prism. MO_4 tetrahedra exhibit a single bond length value varying monotonically between 1.90 Å and 1.89 Å for M = Ta and Nb, respectively. SbO_8 polyhedra are comprised of two distinct bond lengths – 2.43 Å and 2.38 Å, which are unaffected by the Nb concentration. SbO_8 polyhedra form edge-sharing, cross-linked chains along the orthogonal [100] and [010] directions (fig. 3.3a, right). MO_4 tetrahedra are situated interstitially between the SbO_8 chains and are entirely disconnected from one another. Altogether, this structure can be viewed as a $\{SbO_8\}_8$-cluster about a single MO_4 tetrahedron (fig. 3.3a, left), which results in a highly closed packed cell with the lowest volume among the three phases.

Distortions towards the orthorhombic phase result in octahedral coordination in both *M*O and SbO polyhedra. The MO_6 octahedra are relatively close in shape to that of an ideal octahedron, with an average bond length of 2.00 Å, and bond length variance of ~0.1 Å. Nb-substitutions

increase the variance to ~0.2 Å. Each MO_6 octahedra share four corners with adjacent MO_6 octahedra forming layers in the (001) plane (fig. 3.3b, left). Within a layer, the octahedra are tilted alternatingly in the [101] and [$\bar{1}$01] directions (fig. 3.3b, right). The central *M* cations are slightly translated away from octahedral centers in the ±y-direction. Nb-substitutions within an *M*O-layer increase cation translations. These 4d electron induced distortions increase polyhedral volumes, as well as cell volumes. Overall, o-SbMO_4 compounds exhibit the highest volumes among the three phases.

In the orthorhombic phase, *M*O-layers are separated by SbO-layers formed from edge-sharing SbO_6 octahedra. Unlike in the tetragonal phase, these SbO_6 octahedra are heavily distorted, exhibiting three distinct bond lengths. A set of ~2.24 Å and ~2.05 Å Sb-O bonds form the edge connecting neighboring SbO_6 octahedra, as well as corner connections to the neighboring *M*O-layers. A longer ~2.86 Å bond shares a corner with two MO_6 octahedra. In addition, this longer bond, together with the ~2.24 Å forms a shared edge with a MO_6 octahedra. However, these longer bonds are considerably weaker in comparison to the overall bonding network. Therefore, the electronic properties of the orthorhombic phase will most likely be affected primarily by the edge-sharing bonds. In contrast to the MO_6 octahedra, no significant effects are observed in the Sb-O bonds due to Nb-substitutions.

As distortions continue towards the monoclinic phase, SbO_6 octahedra tilting, and consequent transitions from corner-sharing to edge-sharing in MO_6 octahedra, result in a reduction in cell volumes with respect to the orthorhombic phase (fig. 3.3c, right). Furthermore, increasing Nb-substitutions in the monoclinic phase monotonically decrease cell volumes. Though SbO_6 octahedra remain relatively similar in shape to their orthorhombic phase counterparts, the MO_6 octahedra distort significantly away from the ideal octahedron. These distortions break the layer-by-layer

structure in the monoclinic phase. Instead, both octahedra form edge-sharing chains in the [101] and [001] directions, respectively for MO_6 and SbO_6 octahedra – about 110° apart (fig. 3.3c, left). No edge-sharing occurs between the two chains. MO_6 octahedral distortions increase the average bond length to 2.01 Å. Sb-O bond lengths distribute as they do in the orthorhombic phase, with the short set slightly longer at ~2.13 Å and ~2.30 Å, and the longer bond slightly shorter at ~2.66 Å. *M*-O bond lengths decrease by ~0.02 Å with Nb-substitutions. Again, Sb-O bonds remain effectively constant with respect to Nb concentrations.

As expected, cell distortions along the tetragonal-to-orthorhombic-to monoclinic route lead to internal distortions in both SbO and *M*O polyhedra. The orientations of the polyhedra with respect to one another shape the electronic landscape, and consequently the properties of these materials. We investigate these effects in the following section.

3.4.2. Electronic Properties

Calculated cohesive energies show that the overall orthorhombic phases are more stable than tetragonal and monoclinic, as expected from the experimental results of ref. 95, 122, and 123 (table 3.2). To decouple the effects of Nb 4d electrons from the effects of phase-related distortions, we note that despite the diminishing energy differences between the three phases with increasing Nb concentrations, the trend in relative stability remains. Thus, the structural properties discussed in the previous section contribute to the stability of the systems.

To investigate this further, we calculate average Bader net charges on Sb, *M*, and O sites. Figure 3.4 shows that the Sb average net charge remains relatively constant with increasing Nb concentration, as is also evident from the above discussions regarding the negligible effects of the presence of Nb on Sb-O bond lengths. In contrast, the average net charge on *M* sites decreases monotonically with x, implying a decrease in ionicity of *M*-O bonds. The effects of Nb 4d electrons

Table 3.2. Electronic properties of $SbTa_{1-x}Nb_xO_4$ compounds. E_{ground} reflects calculated total energies. Cohesive energies are calculated as described in section 3.2.1. $E_{direct\ gap}$ reflects minimum gap between highest occupied and lowest unoccupied bands at a single k-point. T –tetragonal; M – monoclinic; O – orthorhombic

x	Phase	E_{ground} (eV)	$E_{cohesive}$ (eV)	E_{gap} (eV)	$E_{direct\ gap}$ (eV)
0	T	-193.225	-94.569	2.425	2.721
	O	-197.150	-98.494	2.979	3.074
	M	-194.705	-96.049	2.575	2.705
0.25	T	-191.232	-92.941	2.113	2.431
	O	-194.888	-96.597	2.707	2.894
	M	-192.548	-94.257	2.295	2.367
0.5	T	-189.244	-91.317	2.005	2.343
	O	-192.666	-94.739	2.597	2.805
	M	-190.398	-92.471	2.192	2.285
0.75	T	-187.253	-89.691	1.988	2.310
	O	-190.406	-92.843	2.541	2.786
	M	-188.244	-90.682	2.171	2.227
1	T	-185.269	-88.072	1.982	2.303
	O	-188.185	-90.988	2.486	2.752
	M	-186.096	-88.898	2.149	2.173

are consistent among the three phases. Comparing Figure 3.4 and Table 3.2, we note that reduced *M*-O ionicity generally corresponds to a decrease in stability of the $SbTa_{1-x}Nb_xO_4$ alloy.

Differences in bond ionicity between the phases are relatively constant, unaffected by the presence of Nb. These differences correlate well with the trend in relative stability. Visualizing the charge densities of the three phases of $SbTaO_4$ (fig. 3.5), we note that, in general, charge accumulates about the *M*-O bonding network. Sb sites, on the other hand, see very little charge accumulation. This is especially apparent in the tetragonal phase, where Sb is disconnected from the overall charge density. In the monoclinic phase, some negative charge is observed on the shorter Sb-O bonds. This corresponds to the hybridized anti-bonding states of Sb 5s at the top of the valence (discussed later in connection with the density of states). A similar, though greater charge accumulation occurs in the orthorhombic phase. However, as mentioned in the previous section, the

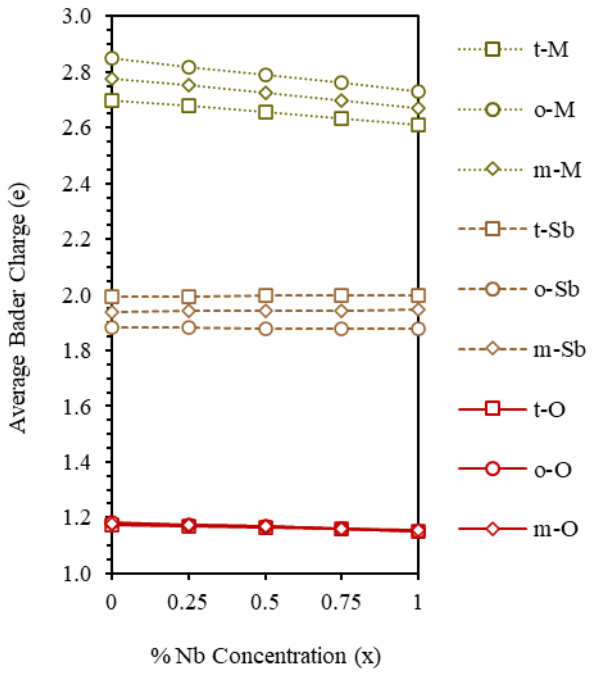

Figure 3.4. Average Bader charges for $SbTa_{1-x}Nb_xO_4$ as a function of x. O charges are given as absolute values for plotting reasons and should be understood as the negative of the given values.

shorter Sb-O bonds of the orthorhombic phase are shorter than their monoclinic counterparts. Furthermore, the Sb-Sb distance is shortest in the orthorhombic phase. Overall, SbO_6 octahedra are closer to each other, as seen in Figure 3.4. This results in higher Sb-Sb polyhedral polar interactions and may play a role in the higher stability of the orthorhombic phase.

Density of states for $SbTaO_4$ and $SbNbO_4$ are shown in Figure 3.6. The valence bands can be split into three sections. From -10 eV to -7 eV, deep valence bands are dominated by the Sb 5s lone pair hybridized with O p orbitals, and to a lesser extent with O s and *M* d orbitals. Integrating total density of states between -10 eV and -7 eV reveals the Sb 5s lone electron pair in all $SbMO_4$ structures**.** The deep valence range is relatively narrow in the tetragonal phase – spreading from -9.5 eV to -8.5 eV and is sharply peaked at the higher end. Nb-substitutions reduce the magnitude of this peak and slightly broaden the range at both ends. The deep valence region of the monoclinic phase is initially more spread – from -9.3 eV to -8 eV, shows far lower peaks, and exhibits similar

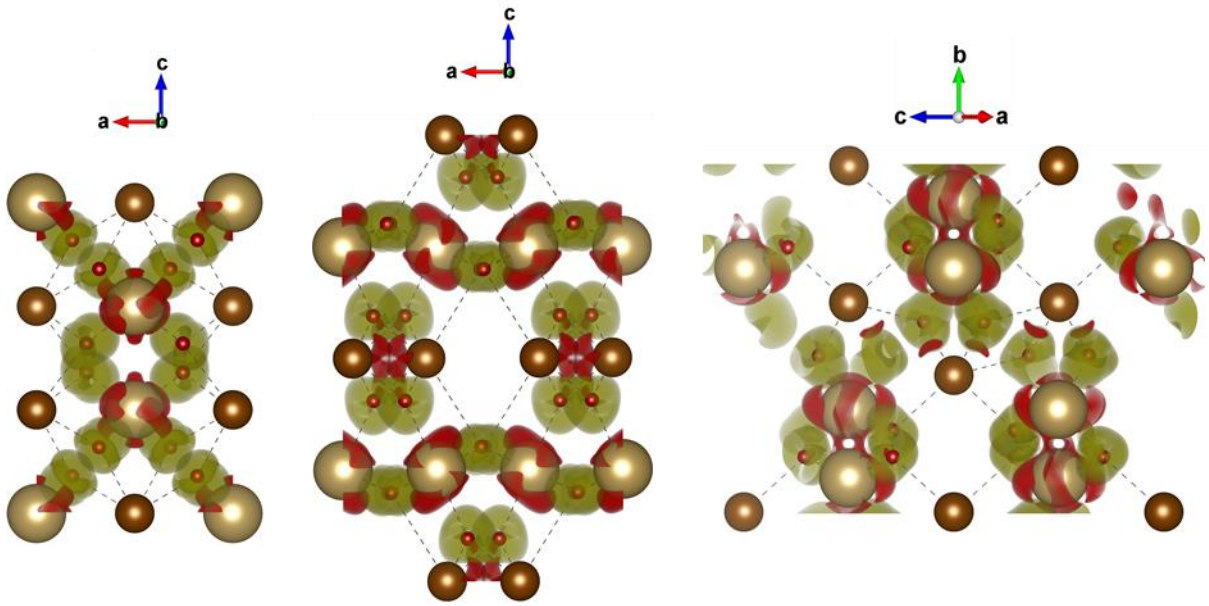

Figure 3.5. Charge density plots for (from left) t-$SbTaO_4$, o-$SbTaO_4$, and m-$SbTaO_4$. Sb shown in brown (medium); Ta shown in green (large); O shown in red (small). For a given unit cell, the density shown in the figure is calculated by subtracting from the total calculated density the sum of the individual densities from separate calculations of the same unit cell containing only a single species at a time. Positive charge shown in green (light gray); negative charge shown in red (dark gray) charge densities are shown with an isosurface level of 0.015 a_0^{-1}, where a_0 is the Bohr radius.

broadening with increases Nb concentration. In contrast, the orthorhombic phase spreads from -9.2 eV down to -7 eV, is discontinuous about -8.2 eV, and exhibits an upshift of ~1 eV between x = 0 and x = 1. No peak broadening is observed. The spreading of the deep valence region in the orthorhombic phase, as well as its broadening by ~0.1 eV with Nb-substitution in the monoclinic and tetragonal phases, is related to the nature of 4d electrons.

The next valence section is loosely defined from -6 eV to -1.5 eV. For all Sb*M*O_4 compounds, this region consists primarily of O 2p orbitals, with a contribution from *M* d, as expected in transition metal oxides. A weaker Sb 5p contribution is observed and is more pronounced towards the tail of the section, where Sb 5p and *M* d weakly hybridize with O 2p. Nb-concentration does not affect this region significantly, as Ta 5d and Nb 4d appear to have similar features. A sharp drop in available states is observed at -1.5 eV in t-Sb*M*O_4. At the valence band maxima

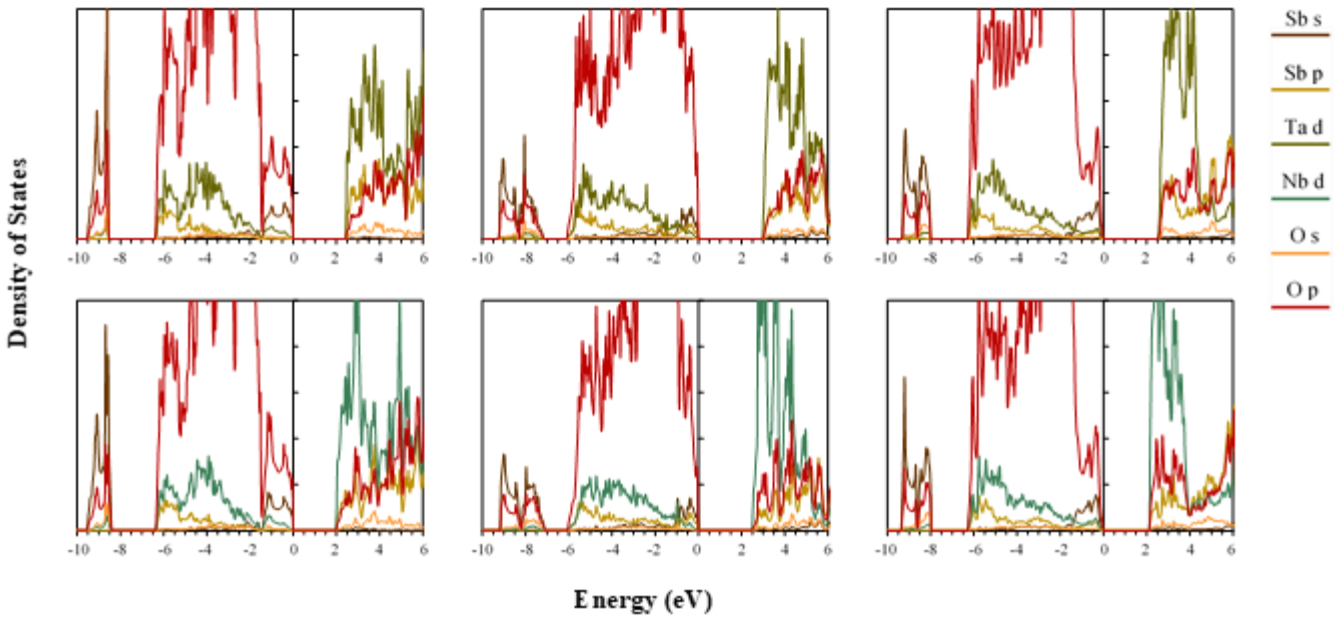

Figure 3.6. Density of states (DOS) shown for $SbTaO_4$ (top) and $SbNbO_4$ (bottom); from left: tetragonal, orthorhombic, and monoclinic. The vertical axis represents number of states per energy level and is plotted up from 0 to 5 in all plots. The x-axis range is chosen to include the deep valence states (-10 eV to -7 eV) highlighting the Sb 5s lone pair. SbO-*M*O polyhedral interaction is measured qualitatively by the degree of separation of densities around -1.5 eV.

(VBM), both the tetragonal and monoclinic phases exhibit a drop in O 2p concentration and an onset of O 2p hybridization with Sb 5s anti-bonding states. Similar results have been observed in Clinobisvanite[29], an ns^2-md^0 material. These hybridized, lower energy anti-bonding states at the VBM positively affect carrier mobility through hole formation[128,129]. In t-Sb*M*O_4, Nb-substitutions increase the magnitude of the hybridized peak at -1 eV. The O 2p drop is less steep in the monoclinic phase, with no apparent discontinuity in available states. The orthorhombic phase, however, exhibits strong O 2p levels throughout the valence, with no significant drop until the Fermi level. A weaker contribution from *M* d orbitals is observed in all three phases. The orthorhombic and monoclinic phases also exhibit a weak Sb 5p contribution.

In summary, the division of the valence bands of Sb*M*O_4 varies from phase to phase, with a degree of mixed contributions from SbO and *M*O polyhedra corresponding to the relative stability of the phases. In the tetragonal phase, the most symmetric and the least stable of the three, the

two contributions are sharply separated at about -1.4 eV. The separation blurs in the more stable monoclinic phase. In the orthorhombic phase, the most stable, the distinction between the lower valence bands of the *M*O polyhedra and the SbO polyhedra contribution at the VBM vanishes entirely. This again shows that even though the orthorhombic phase yields the largest volume of the three phases, its unique octahedral distribution results in close octahedral proximity and increased interactions. This directly affects the electronic properties, more specifically the band gap energies.

Conduction band minima (CBM) are comprised primarily of *M* d states, again as expected for these materials. *M* d states in t-Sb*M*O_4 are less peaked and more spread out about the CBM. However, Nb 4d states are more sharply peaked than Ta 5d. Near the CBM, all three phases exhibit a hybridization of *M* d and Sb 5p states with O 2p. This contribution appears to be weaker in the orthorhombic phase. In the monoclinic phase, O 2p are more concentrated on the CBM edge and increase with Nb-substitutions. Lower-energy 4d electrons pull the conduction band down towards the Fermi level and decrease band gap energy monotonically with increasing Nb concentrations. Average bond lengths remain relatively constant, which suggests that decreasing band gap values within a phase result primarily from increasing 4d electron concentration.

Band gap energy is highest in o-SbTaO4, with a gap ~0.5 eV and ~0.4 eV greater than t-SbTaO4 and m-SbTaO4, respectively. Its calculated band gap value of 2.979 eV is intermediate between those of ref. 95 and 122. As was mentioned, the value obtained in ref. 95 may be high due to the specific amount of Hartree-Fock exchange energy considered within the hybrid functional, while the value obtained in ref. 124 may be low due to improper, or a lack of cell relaxation under the methodology of that study. Using the methodology of the current study, and the experimental lattice parameters of ref. 122 without further relaxation, we calculate the band gap of o-$SbTaO_4$ at

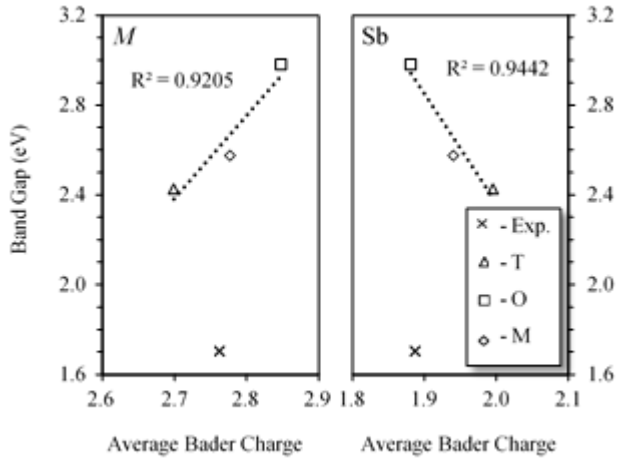

Figure 3.7. Near-linear correlation of band gap energies with calculated oxidation states derived from average Bader charges. Calculated band gap from experimental lattice is shown for reference.

1.704 eV, relatively close to that of ref. 124. We again remind the reader that DFT-calculated band gaps are an underestimated and are more so in d-electron materials. Ref. 124 did not use correction methods – perhaps another reason for its low reported value. Ref. 95 on the other hand did use the hybrid functional approximation of DFT, which is known to provide the necessary band gap energy correction. However, the large reported band gap may have been due to an excessive contribution of Hartree-Fock exchange. Bader charges and electron densities show a reduction in Sb-O covalency throughout the unit cell with experimental lattices in comparison to the GGA-relaxed cell. Comparing band gap energies against trends in Sb and *M* average Bader charges reveals near-perfect linear correlations among the three phases (fig. 3.7). However, the calculated gap from the experimental cell is significantly deviated from the trend line.

Minimum direct gaps are mostly found about the VBM (fig. 3.8). Two exceptions are seen in t-SbMO$_4$, in which for x = 0.5 and x = 1, the direct gap near the CBM is lower by ~0.1 eV than that found near the VBM. Moreover, the differences between the minimum direct gap of t-SbMO$_4$ and its indirect gap are largest among the three phases for all values of x, with x = 0.5 exhibiting

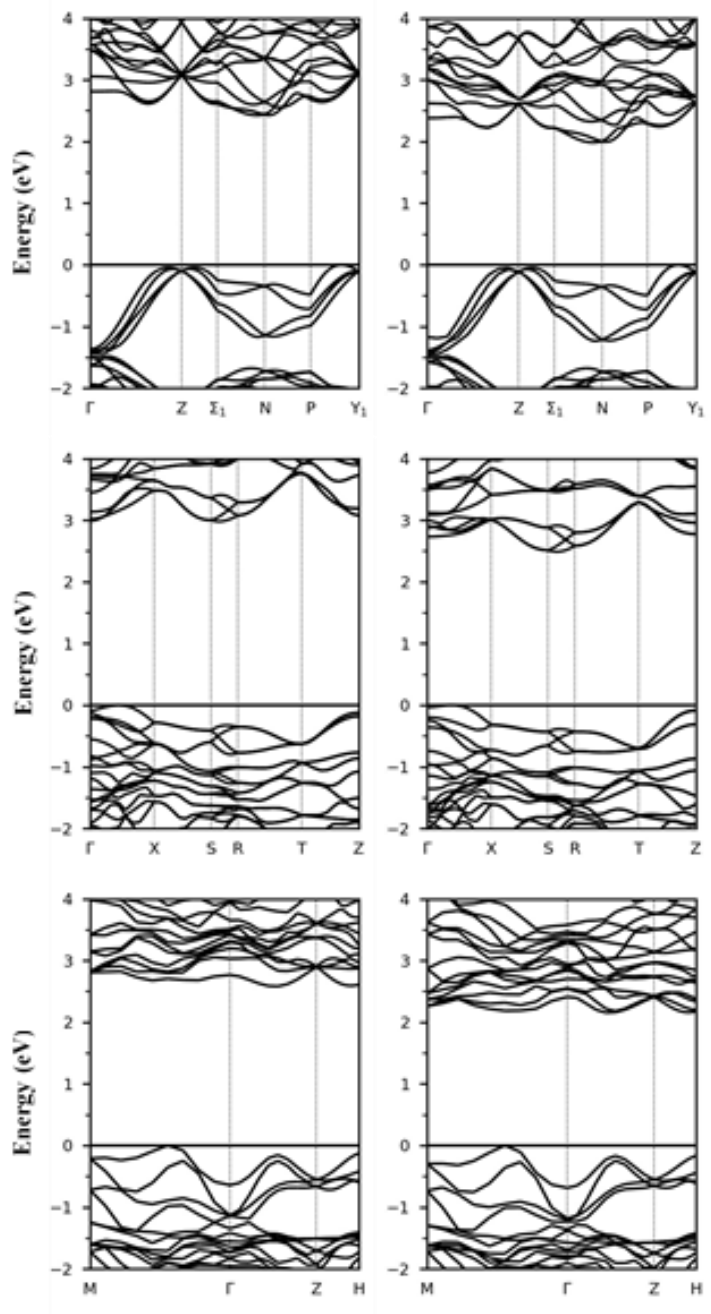

Figure 3.8. Electronic band structure plotted for $SbTaO_4$ (left) and $SbNbO_4$ (right); from top: tetragonal, orthorhombic, and monoclinic. Brillouin zones and special symmetry points are obtained from AFLOW based on GGA relaxed geometries.

the largest difference. Inversely, these differences are minimal in the monoclinic phase, with m-$SbNbO_4$ exhibiting a minimum direct gap of 2.173 eV, only 0.024 eV greater than its indirect gap. Considering that both occur at the VBM, m-$SbNbO_4$ may be considered a direct gap material.

A similar phenomenon occurs in o-$SbTaO_4$, in which the 3.074 eV minimum direct gap is only 0.095 eV greater than the indirect gap and occurs closer to the VBM.

3.5. Conclusion

We have studied $SbTa_{1-x}Nb_xO_4$ (x = 0, 0.25, 0.5, 0.75, 1) in the tetragonal, orthorhombic, and monoclinic phases. The resulting $Sb^{3+}M^{5+}O^{-2}{}_4$ material is part of the ns^2-md^0 transition metal oxide group, which has showed promise towards higher photocatalytic activity. The orthorhombic phases were found to be most stable, with higher band gap energies. Decreasing band gap energies have been shown to result from increasing 4d electron concentrations and structural distortions. It was determined that both orbital and polar interactions of MO and SbO polyhedra are responsible for the relative stability of these phases. We decoupled the two effects by studying the band gap variations between three phases of $SbTaO_4$ and $SbNbO_4$ separately. Structural distortions in both have been linked to the ionic bonding character of the materials. Near indirect-to-direct gap transitions were observed in m-$SbNbO_4$ and o-$SbTaO_4$. These results are part of a fundamental study of the stibiotantalite mineral in the scope of photoferroelectric materials.

Acknowledgements

Computations were executed locally at the High Performance Computing (HPC) center at UTA, as well as on the Texas Advanced Computing Center (TACC). This work is supported by NSF grant # 1609811.

Chapter 4

Isovalent Alloying and Lone-Pairs

Introductory Comments

The following manuscript explores the 5s/6s mixed lone-pair environment of Sb-alloyed Bi_2WO_6. The proximity of Sb $5s^2$ lone-pair electrons to O 2p is shown to upshift the VBM above the hybridized Bi 6s – O 2p antibonding state. The varying degree of VBM upshift is attributed to the different orientations of Sb 5s – O 2p antibonding states depending on the alloying scheme. The higher Sb 5s – O 2p VBM also exhibits reduced hole effective mass with respect to the pristine cell. Observed CBM upshifts are attributed to increased W 5d – O 2p hybridization in WO_6 octahedra due to distortions induced by the neighboring Sb $5s^2$ electrons. Overall, Sb alloying in Bi_2WO_6 yields favorable properties for PEC applications.

The author of the present dissertation acknowledges Dr. Aron Walsh for his careful review of the manuscript and his expertise in lone-pair electron research.

$BiSbWO_6$: PROPERTIES OF A MIXED 5s/6s LONE-PAIR-ELECTRON SYSTEM

Edan Bainglass
Aron Walsh
Muhammad N. Huda

Bainglass, E., Walsh, A. & Huda, M. N. BiSbWO6: Properties of a Mixed 5s/6s Lone-Pair-Electron System. *Chem. Phys.* 111117 (2021).

© 2021 Elsevier B.V. All rights reserved.

$BiSbWO_6$: Properties of a Mixed 5s/6s Lone-Pair-Electron System

E. Bainglass[1], Aron Walsh[2,3], and M. N. Huda[1]

[1]Department of Physics, The University of Texas at Arlington, Arlington, TX 76019, USA

[2]Department of Materials, Imperial College London, London SW7 2AZ, United Kingdom

[3]Department of Materials Science & Engineering, Yonsei University, Seoul 07322, South Korea

Abstract

We investigate the behavior of lone-pair electrons in a mixed Sb(5s)/Bi(6s) crystal environment. Density functional theory is used to calculate the electronic properties of Sb-alloyed Bi_2WO_6 and to study the effects of introducing Sb 5s orbitals to the band structure. The band edge positions, partial charge analyses, and band decomposed charge densities of $BiSbWO_6$ are used to explain the observed trends in relative stability and band edge shifts. To isolate the role of the mixed lone pairs, we consider WO_3 as a control model. We find that local distortions caused by Sb 5s lone-pair electrons lead to upshifts in both valence and conduction band edges.

4.1. Introduction

Post-transition multinary metal oxides of electronic configuration ns^2-md^0 have been highlighted as efficient photocatalysts[27,89,90] due to their favorable optoelectronic properties. They can exhibit high hole mobility arising from ns^2 – O 2p hybridization at their valence band maxima (VBM), which reduces O 2p localization. At their conduction band minima (CBM), np^0 – md^0 hybridization increases empty d-band dispersion, which improves electron mobility. Furthermore, the ns^2p^0 configuration of the post-transition cations can lead to unique crystal distortions due to the formation of stereochemically active electron lone pairs[130]. In such cases, the phenomenon has been further correlated with hybridizations of cation *s*, *p*, and anion *p* orbitals, which altogether shape the frontier orbitals and determine their energetic position[131,132].

We recently studied one such system, namely $SbTa_{1-x}Nb_xO_4$[133], in several common post-transition metal oxide phases, and found that varying the ionic/covalent character of the structure as a function of crystal phase and *n*d orbital contributions directly affected its overall stability and electronic properties. The layered structure of the orthorhombic stibiotantalite phase was found to be most stable. Moreover, its MO_6 layers (*M* = Ta, Nb) played a key role in determining the position of the band edges. These properties were influenced by the behavior of Sb 5s lone-pair electrons. In the present study, we clarify the effects of lone-pair electrons on the electronic structure of ns^2-md^0 materials. We show that variations in the lone-pair environment via isovalent alloying of the post-transition metal can shift band edge positions towards optimal values for photocatalytic water-splitting.

Of the ns^2-md^0 class of materials, none have received greater attention than $BiVO_4$. Regarded as a paradigm in photocatalytic semiconductor material research for its favorable properties, as well as its challenges[29,30,34–36,134,135], it has been extensively studied both experimentally and theoretically and is often used as a platform for designing new photocatalysts[32,37,136,137]. Due to the localized V 3d conduction orbitals, $BiVO_4$ charge transport properties are affected by the formation of small polaronic states[34,35,135]. Due to the poor transport properties, experimentally measured currents in $BiVO_4$ under visible light have come up short with respect to theoretically predicted values[35,36]. Alternatively, one may consider materials with more delocalized conduction bands, such as W $5d^0$ compounds. Here, the probability of forming polaronic trap states may be reduced allowing for higher charge carrier mobilities. One such example is the russellite mineral, or Bi_2WO_6, which itself has enjoyed a great deal of attention in photocatalysis research, though mostly under an experimental lens[138–143]. It has a suitable band gap range of 2.6-2.9 eV, with a VBM situated below the O_2 reduction potential allowing for oxygen evolution[144,145]. Its CBM,

however, is slightly short of the H_2 reduction potential necessary for hydrogen evolution. Moreover, Bi_2WO_6 suffers from a high recombination rate, which limits its photocatalytic efficiency. This is often rationalized from the perspective of bulk defect states and/or surface morphologies that can lead to charge transfer paths longer than the carrier lifetime. Heterojunction design-schemes have been proposed to improve charge separation and mobility in Bi_2WO_6[146–155]. Moreover, selective alloying has been shown to affect its band gap and band edge positions[145,156–158], improving its photocatalytic efficiency. We aim to combine and expand on these results.

The room-temperature γ-phase of Bi_2WO_6, known as the Aurivillius phase[159] – space group $P2_1ab$ (29) – is uniquely characterized by perovskite-like MO_6 layers (M = W, Mo) sandwiched between bismuth oxide layers. Various post-transition metals have been shown to retain the Aurivillius layered structure when introduced to the bismuth oxide matrix[160–164]. Interestingly, in the case of antimony, bismuth layers may be entirely replaced. This has led to the discovery of the Aurivillius-related phases Sb_2WO_6[162] and Sb_2MoO_6[165]. Castro et al. studied the structural evolution of the $Bi_{2-x}Sb_xWO_6$ solid solutions and determined its stability up to x = 1.5, with larger values incurring a phase transition towards the ferroelastic triclinic phase of Sb_2WO_6[163]. These solid solutions have also been studied for lithium ion battery applications[166] and photocatalysis[167]. To the best of our knowledge, the effects of isovalent Sb alloying on the electronic properties of Bi_2WO_6 have yet to be studied theoretically. Furthermore, the electronic structure of a mixed environment of varying stereochemical activities has not been explored. Lone-pair electrons of higher period post-transition cations tend to be less stereochemically active for a fixed anion species. Therefore, Sb 5s lone-pair electrons are expected to interact more strongly with the O environment compared to their Bi 6s counterpart, affecting both the crystal and electronic structures. In the present work, we investigate the electronic properties of $BiSbWO_6$, limiting the alloy composition to within the

experimentally verified stable range[163], with emphasis on the effects of the mixed 5s/6s lone-pair environment on the band gap and band edge positions. The choice of Bi_2WO_6 as a design candidate addresses both abundancy and safety concerns, while the isovalent alloying scheme is expected to allow for simple processing. We briefly address the viability of $BiSbWO_6$ as a component in a proposed heterojunction architecture to facilitate charge transport and mobility.

4.2. Methodology

We probe the crystal and electronic structures based on first-principles density functional theory (DFT)[56,57]. The Vienna ab initio Simulation Package (VASP 5.4.4)[103,104] plane-wave implementation of DFT is employed in calculating total energies, density of states, and electronic band structures for Bi_2WO_6 and its Sb-alloyed derivatives. The generalized gradient approximation formalism of Perdew, Burke, and Ernzerhof (GGA-PBE)[66,67] is used to approximate exchange and correlation contributions to the energy functional. The following valence electron configuration is considered: Bi{$6s^2 5d^{10} 6p^3$}, W{$5p^6 6s^2 5d^4$}, O{$2s^2 2p^4$}, and Sb{$5s^2 5p^3$}. Remaining core electrons are modeled using the projector augmented wave methodology (PAW)[84,102]. Brillouin zone integrations are performed using a gaussian-like finite temperature approach[168] with σ (k_BT) = 0.01. The same is done for band structure calculations along high symmetry points. The tetrahedron method[106] is utilized for density of states (DOS) calculations. Monkhorst-Pack[83] *k*-space sampling of the Brillouin zone is implemented for all structures. Total energies are calculated with a 7×7×3 *k*-mesh. DOS calculations are performed on a finer 11×11×5 mesh. A plane wave cutoff of 600 eV is applied in all calculations. Both the *k*-mesh and plane wave cutoff values were systematically converged within a 1 meV difference in total energy. We apply a $[abc] \rightarrow [cab]$ transformation to the pristine Bi_2WO_6 unit cell (space group $Pc2_1b$) aligning the long lattice vector with the z-axis. Planes and directions are referenced with respect to this orientation. Unit cells are

relaxed until ionic forces are less than 0.01 eV/Å. Symmetry constraints are applied in light of previous experimental findings[163]. Lastly, the known underestimation of band gaps by DFT-GGA[73,108,169] is ignored due to the comparative nature of the present study.

4.3. Results & discussion

The relaxed crystal structure of Bi_2WO_6 is shown in Figure 4.1(a). Calculated lattice parameters (a = 5.563 Å, b = 5.605 Å, c = 16.857 Å) are in good agreement with experimental diffraction measurements[170] considering the standard overestimation by GGA functionals[127]. The electronic structure of pristine Bi_2WO_6 is shown in Figure 4.2. The width, dispersion, and spherical distribution of Bi 6s – O 2p bonding states between -10 and -7 eV, as well as the small O 2p contribution to the DOS at this range, all point to the weak stereochemical activity of Bi 6s lone-pair electrons. Bi 6s – O 2p antibonding densities form the upper valence band (inset) and project out into the spatial voids observed in Figure 4.1(b) along the y-axis. Weak Bi 6s – O 2p interactions do not lead to high VBM band dispersion predicted in ns^2-md^0 materials, with a calculated hole

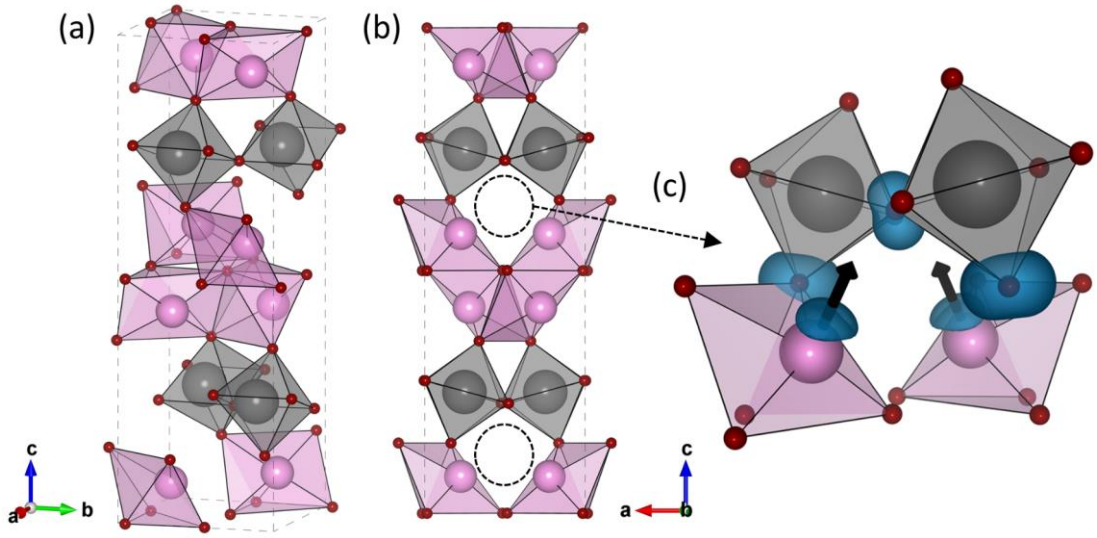

Figure 4.1. (a) Bi_2WO_6 relaxed crystallographic unit cell. Pink polyhedra (top, bottom, and center) represent Bi_2O_2 layers; oxygen atoms are represented by dark red (smallest) spheres; WO_6 layers are shown in dark grey. (b) Bismuth lone-pair induced spatial voids are marked by dashed circles. (c) Lone-pair antibonding densities are drawn with an isosurface value of 0.015 $Å^{-3}$ (blue). Vectors mark lone-pair projections.

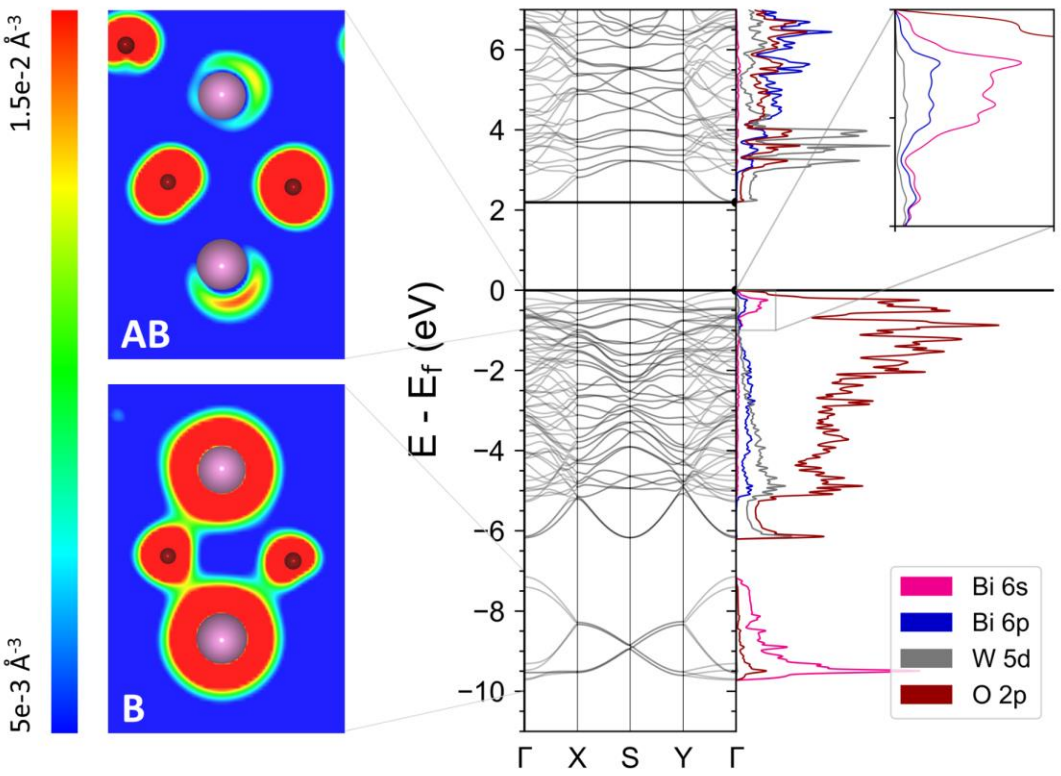

Figure 4.2. Electronic band structure and density of states (right) for Bi_2WO_6. Band decomposed charge densities (left) are drawn for Bi 6s – O 2p bonding (B) and antibonding (AB) states. Antibonding contributions to the VBM are shown in the inset.

effective mass of 3.5 m_0 (along the Γ-Y direction). In contrast, the CBM is less dependent on lone-pair electrons, as it is primarily comprised of W 5d – O 2p hybridized orbitals, with a calculated direct band gap of 2.19 eV about the Γ-point and an electron effective mass of 0.9 m_0 (along the Γ-Y direction). Based on this analysis, the introduction of Sb 5s electrons is likely to affect the upper valence band primarily while retaining the high dispersive nature of the lower conduction band. However, structural distortions due to substitutional alloying may affect the electronic structure. As seen in Figure 4.1(c), Bi 6s – O 2p antibonding densities lead to tilting of adjacent WO_6 octahedra. MO_6 octahedral tilting has been shown to affect the band gap and band edge positions in ns^2-md^0 materials[95,133]. Radha et al. attributed a 0.1 eV difference in conduction band energy between Bi_2WO_6 and pyrochlore $BiFeWO_6$ to the influence of Fe 3d electrons on nearby WO_6

octahedra[145]. Hence, the CBM may indirectly depend on the mixed lone-pair environment via local structural distortions.

To explore the configurational space of $BiSbWO_6$, we selected six representative input geometries, each designated as Sb *i*. In configurations Sb 1-3, dopants are placed into (001) layers to probe the layered nature of the Aurivillius phase. In Sb 4-6, Sb is intermixed within Bi_2O_2 layers. The relaxed $BiSbWO_6$ structure models are shown in Figure 4.3. Their relative stability is measured through calculated formation enthalpies, ΔH_f, obtained from[45]

$$\Delta H_f(m) = E(m) - \sum_x n_x E(x)_{bulk} \tag{4.1}$$

where $E(m)$ is the calculated total energy of configuration m, and $E(x)_{bulk}$ is the total energy of the common bulk phase of constituent x multiplied by the number of sites n_x. Note that for oxygen, we consider the total energy of an oxygen dimer in the calculation. A more negative formation enthalpy indicates greater relative stability. Figure 4.4 shows that calculated formation enthalpies for the six configurations lie within a narrow ~30 meV window, on the order of $k_B T$ at room temperature. Additional calculations were performed on four 2 × 2 × 1 Bi_2WO_6 supercells, each with a random sample of half its Bi sites substituted for Sb. The calculated formation enthalpies

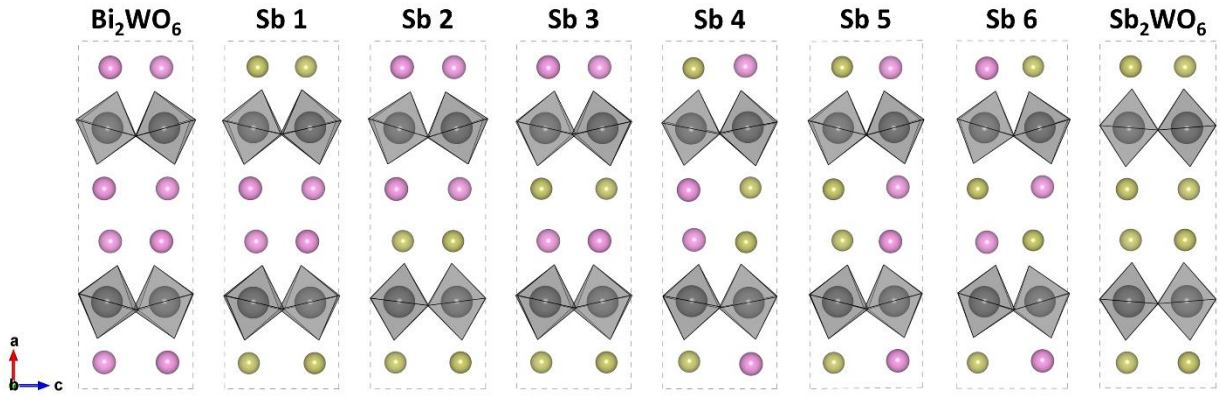

Figure 4.3. Optimized unit cells of $Bi_{2-x}Sb_xWO_6$. $BiSbWO_6$ (x = 1) configurations are labeled as Sb i. Oxygen sites are not shown for clarity. Sb is shown in green. WO_6 octahedra are shown to highlight variations in octahedral tilt in the presence of Sb 5s lone-pair electrons.

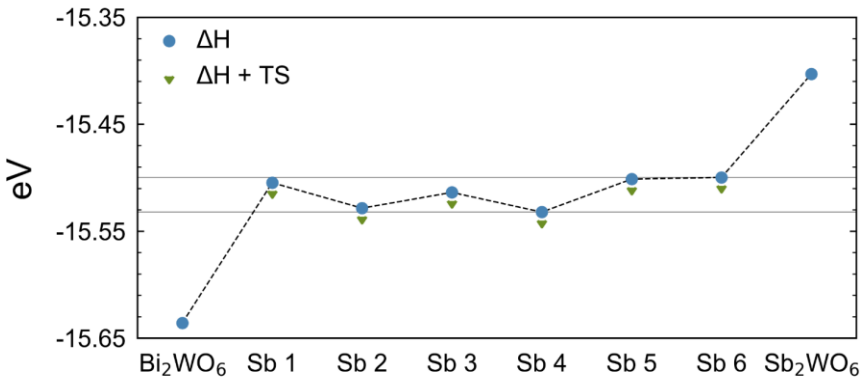

Figure 4.4. Calculated formation enthalpies. Configurational entropy (TS) is added for $BiSbWO_6$ via eq. 4.2. Formation enthalpies for $BiSbWO_6$ lie within a narrow ~30 meV band marked by solid lines.

of the four supercell lie within an even-narrower range of ~10 meV roughly in the middle of the ~30 meV window. Hence, we argue that during synthesis, $BiSbWO_6$ may form as an ensemble of many possible configurations resulting in a homogeneous distribution of Sb and W ions. This suggestion merits an examination of configurational entropy in the system. An approximation of configurational entropic contributions to the overall stability of a compound in the presence of substitutional impurities can be obtained from[171]

$$S = -k_B \sum_{i=1}^{N} x_i \log(x_i) \tag{4.2}$$

where N is the number of sites available for substitution – taking limiting factors into account such as the oxidation states of the relevant species and charge neutrality – x_i is the relative composition of species i, and k_B is Boltzmann's constant. The maximum entropy occurs at equal compositions. For $x_{Bi} = x_{Sb}$, configurational entropy lowers energies by ~8 meV at 300 K, which is not significant enough to shift the relative stability band of $Bi_{2-x}Sb_xWO_6$ beyond its extreme configurations (x = 0, 2).

Although Bi and Sb both have the same formal oxidation state of 3^+ in this system, Bader partial charge analysis[87,111–114] gives a lower effective charge for Sb compared to Bi (fig. 4.5),

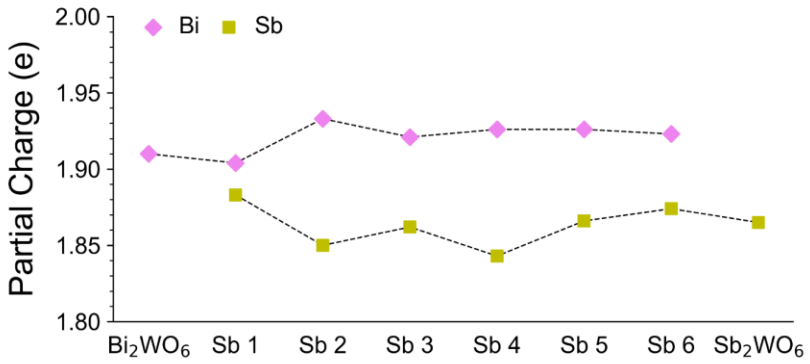

Figure 4.5. Partial charge of post-transition sites calculated by subtracting average Bader charges from the number of valence electrons per element. Sb partial charge follows the same trend as formation entahlpies in the six selected $BiSbWO_6$ configurations (fig. 4.4). W and O exhibit constant partial charges of 2.87 and -1.11, respectively.

which agrees with their relative electronegativities. Despite the small differences in formation enthalpies, comparing Figures 4.4 and 4.5 suggests they may be correlated with the partial charge of Sb, as both follow a similar trend across the six selected configurations of $BiSbWO_6$. We attribute this to the degree to which Sb 5s – O 2p orbitals overlap. The closer proximity of Sb 5s and O 2p energy levels[131] provides a path for stabilizing the given configuration through orbital hybridization. Increased proximity of Sb and O sites leads to greater orbital overlap and consequently a more stable system. In Figure 4.6, we measure Sb cationic shifts in $BiSbWO_6$ via Baur distortion indices[172] and Sb-O bond lengths. Distortion indices mirror formation enthalpies across all

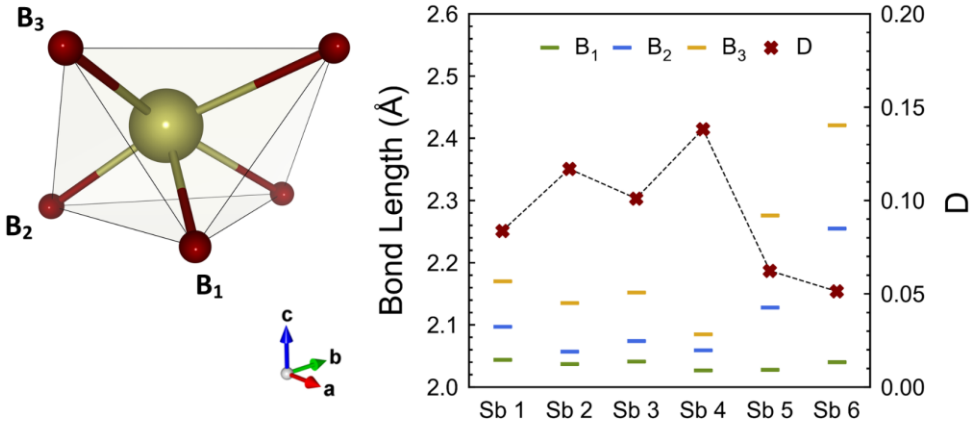

Figure 4.6. Baur distortion indices (D) and selected bond lengths for a represantative Sb polyhedron across the six $BiSbWO_6$ configurations. Higher distortion reflects a larger Sb cationic shift towards one end of the polyhedron.

configurations. We note that Sb 4 – the most stable configuration – exhibits the highest distortion, indicating the largest Sb cationic shift resulting in the shortest Sb-O bonds. Similar reasoning explains the poor stability of the Sb 6 configuration. The electronic structure of Sb 4 is given in Figure 4.7. Bi 6s – O 2p bonding states retain their spherical distribution in the mixed lone-pair environment. Sb 5s – O 2p bonding states, on the other hand, are asymmetric, with delocalized charge shifting towards the nearest O sites. The magnitude of the Sb 5s – O 2p antibonding charge density is significantly larger and takes over the VBM with near double the density of states (inset). This results in a narrower, though now indirect band gap (1.98 eV). The stronger Sb 5s – O 2p interaction also reduces the hole effective mass to 3.1 m_0 (X-S). W 5d – O 2p states retain their high dispersion, with an electron effective mass of 0.8 m_0 (Γ-X). Overall, Sb-in-Bi substitution improves carrier mobility.

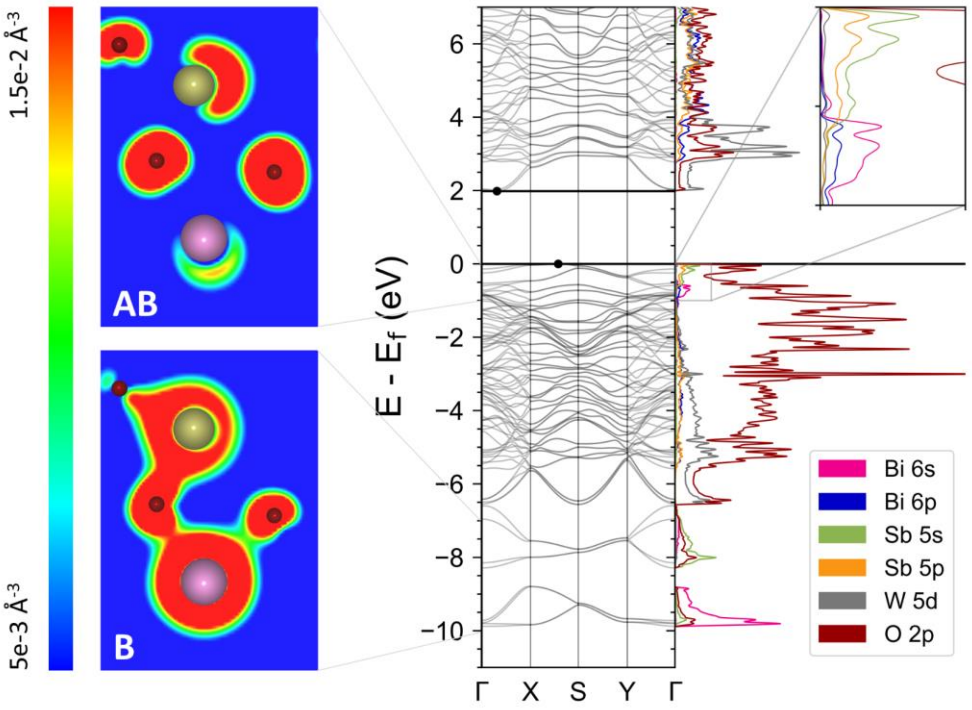

Figure 4.7. Band structure and density of states (right) for the Sb 4 configuration of $BiSbWO_6$. Band decomposed charge densities (left) show the contrast between the spherically symmetric Bi 6s – O 2p and asymmetric Sb 5s – O 2p bonding (B) states. A significantly larger antibonding (AB) density is projected away from Sb sites and contributes more states near the valence band maximum (inset).

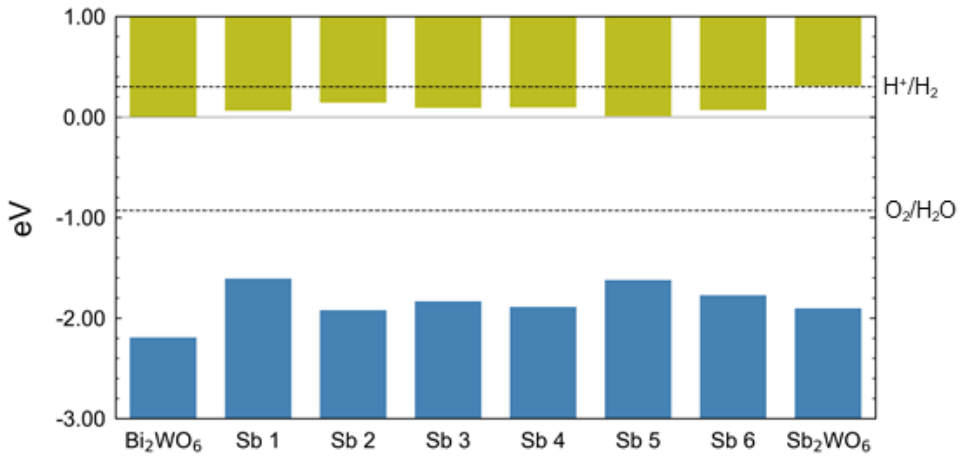

Figure 4.8. Aligned valence (blue) and conduction (green) band energies for the Sb/Bi end member compounds and six alloy models (alloy symbols Sb *i* are defined in Figure 4.3) . A globally averaged O 1s core state is used as a reference. The Bi_2WO_6 conduction band is set to 0 eV. The water redox potentials are shown in dashed lines and are positioned with respect to the empirically derived conduction band edge of Bi_2WO_6 (see text for reference).

To compare $BiSbWO_6$ band edge positions on an equal footing, we align the bands by referencing VBM/CBM levels to the deep O 1s core level. This reference state was averaged over all O sites and across all $Bi_{2-x}Sb_xWO_6$ configurations. The results are shown in Figure 4.8. The water redox potentials are shown with respect to an empirically derived CBM level for Bi_2WO_6[145]. In all cases, Sb 5s – O 2p antibonding states upshift the valence band with respect to the pristine cell. We note that the largest upshift (0.57 eV) leaves the VBM well below the water oxidation potential. More interestingly, conduction band upshifts are also observed across the board and follow a similar trend of the distortion indices. This suggests that local structural distortions about Sb sites do exert an influence on the nearby WO_6 layers and indirectly affect the conduction band energy. The largest upshift among the $BiSbWO_6$ configurations is seen in Sb 2 (0.14 eV). We note that in the Sb 2 configuration, one WO_6 layer is sandwiched between Sb_2O_2 layers (fig. 4.3), which appears to decrease octahedral tilting in the WO_6 layer. This configuration is effectively doubled in the Sb-rich Sb_2WO_6 case, where the CBM upshift is 0.31 eV. We showed in Figure 4.1(c) that WO_6 octahedral tilting occurs in the presence of lone-pair antibonding densities. We investigate

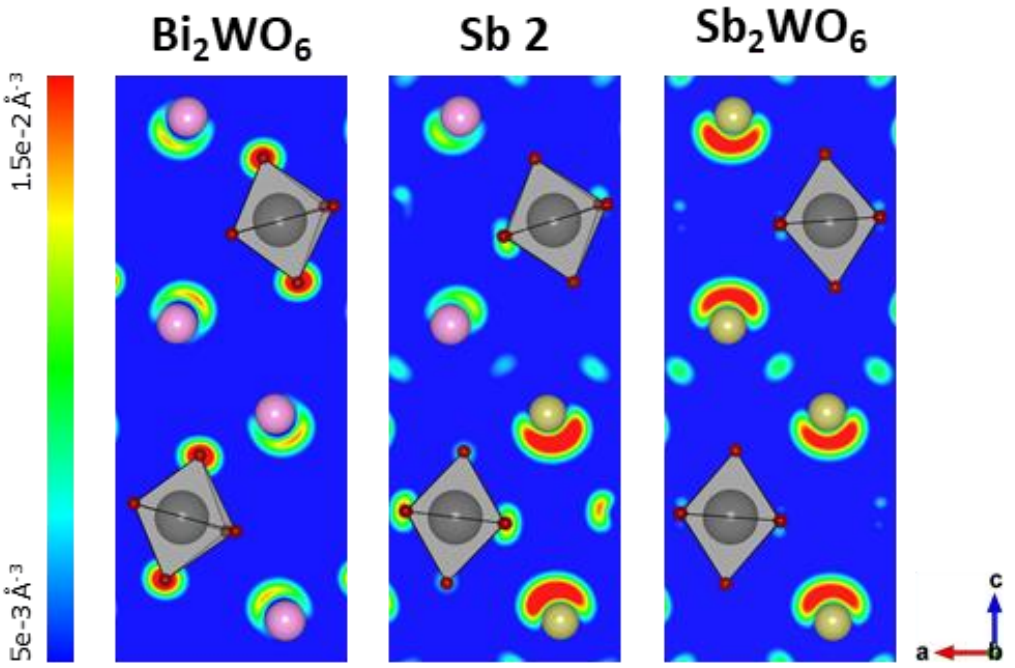

Figure 4.9. Band decomposed charge densities showing the dependency of WO_6 octahedral tilt on the magnitude of neighboring *n*s – O 2p antibonding densities. Sb 2 refers to the mixed Sb/Bi model shown in Figure 4.3.

this further by comparing the charge densities of Bi_2WO_6, Sb 2, and Sb_2WO_6 antibonding states (fig. 4.9). Sb 5s – O 2p antibonding densities align more strongly along the z-axis and interact with O sites at the nearest corners of WO_6 octahedra, which consequently reduces their tilt. This Sb-O-W interaction can be seen in the DOS of Sb 4 (fig. 4.7), where Sb 5s – O 2p and W 5d – O 2p bonding states overlap at the bottom edge of the valence band. We later show that this overlap is directly proportional to the CBM upshift.

To better understand how WO_6 octahedral tilting affects the band structure, we manually tilt a single layer of WO_6 octahedra in monoclinic WO_3. The binary oxide is chosen for its similar W-O environment and the absence of s^2 lone-pair cations. In Figure 4.10, we compare the band structure of three WO_3 unit cells. The fully relaxed unit cell represents the control case. In the other two cells, we manually twist WO_6 octahedra in a single layer, keeping the adjacent layer in its relaxed geometry. In the band structure, we mark three bands of interest. The W 5d – O 2p

antibonding state is shown in green. The bonding state of the frozen (distorted) layer is in blue (orange). Reducing the applied distortion back towards the relaxed geometry – from Figure 4.10(a) to Figure 4.10(c) – causes a downshift of the distorted bonding state. Its antibonding counterpart at the CBM near the Γ-point gradually upshifts and becomes degenerate with that of the frozen layer. We attribute this to bonding-antibonding splitting due to increasing W 5d – O 2p hybridization. This is apparent both in band decomposed charge densities, as well as in average W-O bond

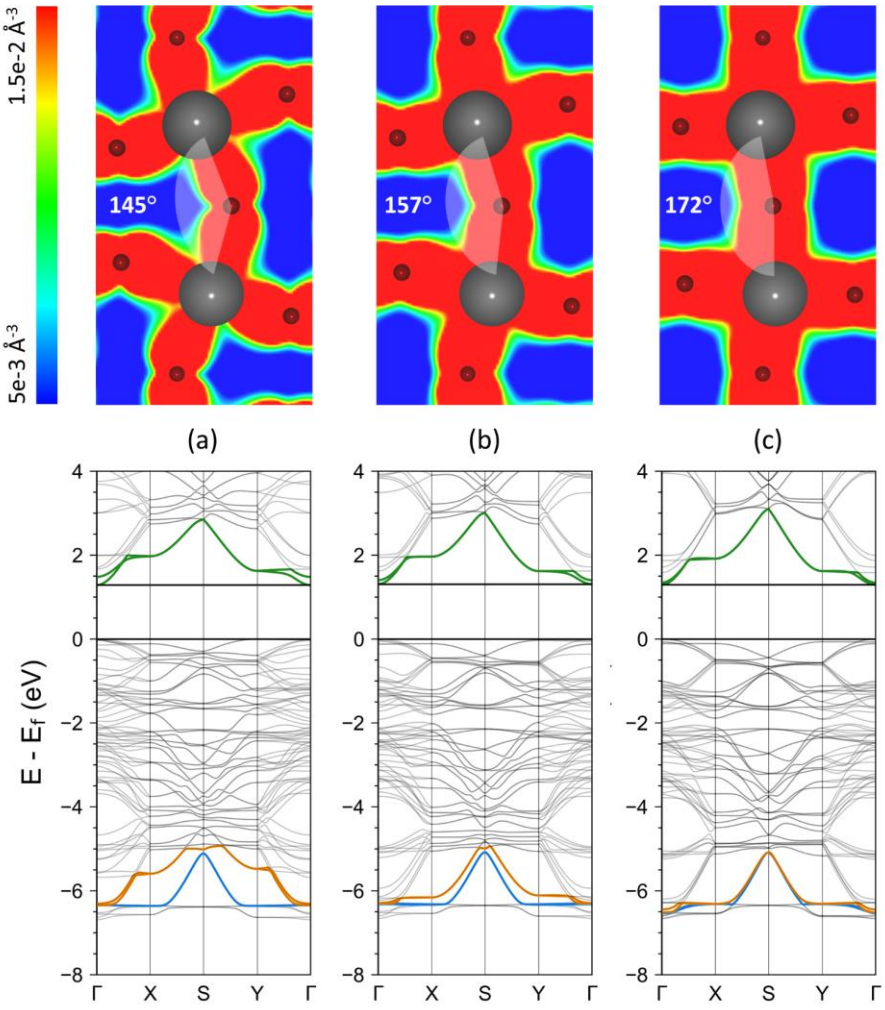

Figure 4.10. Band structures and band decomposed charge densities for monoclinic WO_3 with manually applied tilting resulting in (a) 145° and (b) 157° W-O-W angles. The relaxed unit cell (c) exhibits a W-O-W angle of 172° and is used for control. Charge densities are projected onto the bonding states at the bottom of the valence band. The W 5d – O 2p bonding state for the distorted (fixed) layer is shown in orange (blue). The corresponding antibonding state is in green.

lengths, with 2.006 Å at the highest distortion and 1.945 Å in the relaxed cell. Hence, reduced tilting of WO_6 octahedra with respect to one another results in shorter W-O bond lengths and increased W 5d – O 2p hybridization. This in turn raises the conduction band.

We now apply the same reasoning to the relaxed models of Bi_2WO_6, Sb 2, and Sb_2WO_6. In Figure 4.11, we project the charge density of each unit cell onto the bonding state of its lower WO_6 layer. We first note that in $Bi_{2-x}Sb_xWO_6$, the natural driving force behind the twisting of WO_6 octahedra is the apparent onset of hybridization about the W-O-Sb bonding network clearly

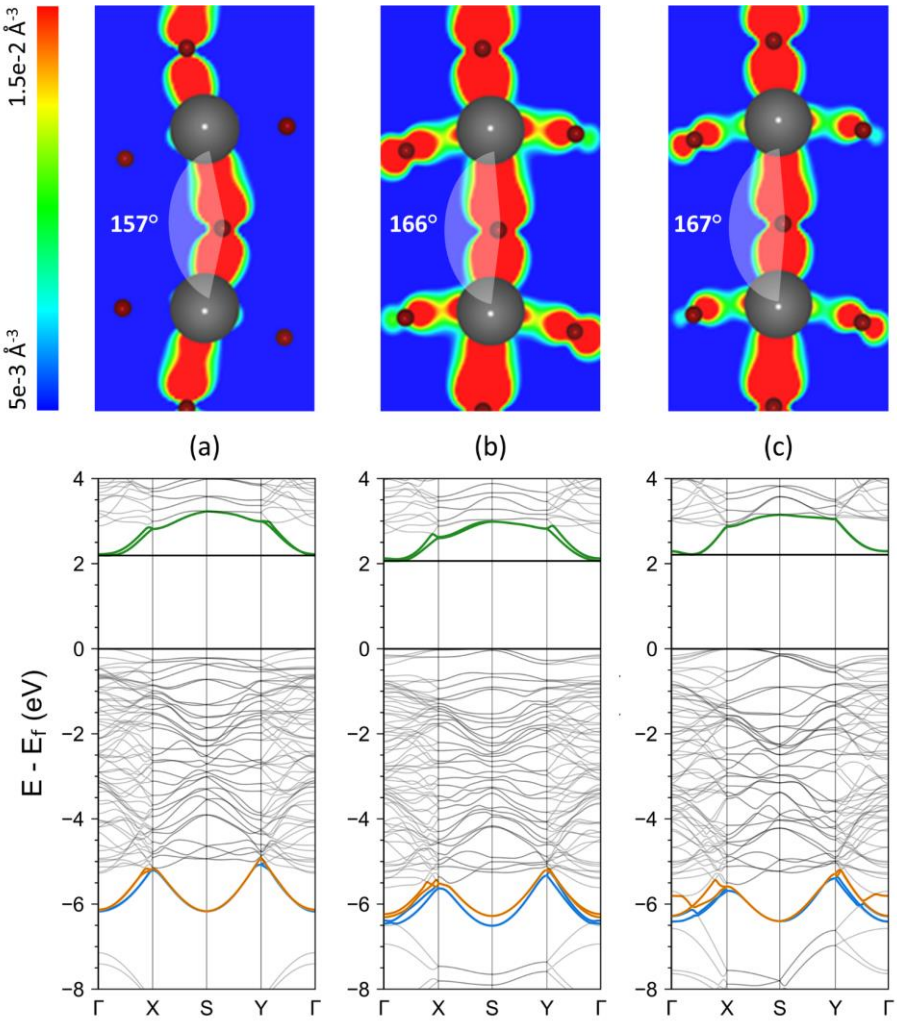

Figure 4.11. Band structures and band decomposed charge densities for (a) Bi_2WO_6, (b) Sb 2, and (c) Sb_2WO_6. Charge densities are projected onto the bonding state of the lower WO_6 layer. The W 5d – O 2p bonding state for the top (bottom) WO_6 layer is shown in orange (blue). The corresponding antibonding state is in green.

missing in the Bi_2WO_6 charge density. This does appear to increase hybridization within the WO_6 layer. However, unlike in monoclinic WO_3, the average W-O bond lengths do not decrease monotonically – 1.977 Å in Bi_2WO_6 (fig. 4.11a), 1.971 Å in Sb 2 (fig. 4.11b), and 1.984 Å in Sb_2WO_6 (fig. 4.11c). Similarly, the hybridization about the W-O-W bonding network increases in Sb 2 but decreases slightly in Sb_2WO_6. To explain the position of their conduction band edges, we point to the asymmetric alloying scheme of Sb 2. The WO_6 layer surrounded by Sb has a W-O-W bond angle of 166°, greater than the 153° angle measured in Bi_2WO_6. However, the WO_6 layer surrounded by Bi exhibits a 151° angle, as well as longer average W-O bond lengths (1.990 Å). Therefore, the stronger hybridization in the lower WO_6 layer of Sb 2 does lead to a bonding-antibonding splitting of W 5d – O 2p states observed in Figure 4.11(b), but the lack of Sb 5s interactions in its upper WO_6 layer leaves the corresponding bonding and antibonding states lagging behind. This reduces the overall magnitude of the CBM upshift. Though Sb_2WO_6 exhibits reduced hybridization in the lower WO_6 layer – resulting in a lesser bonding-antibonding splitting – the identical splitting occurring in its upper WO_6 layer results in both conduction bands shifting upwards. The larger 167° W-O-W in the lower WO_6 layer of Sb_2WO_6 compared to the 151° in the upper WO_6 layer of Sb 2 suggests that the degenerate CBM of the former is situated above the conduction band of the latter. This explains its higher CBM.

The configuration of Sb 2, in which WO_6 layers are sandwiched between single-post-transition-metal species, offers an interesting opportunity for facile heterojunction design as a natural extension of the pristine cell. Such crystal engineering could be used to enhance both light absorption and charge carrier separation, reducing non-radiative losses and improving photocatalytic efficiency. We find that the Sb 2 configuration is well-suited for forming a heterostructure, as its in-plane lattice parameters (a = 5.558 Å; b = 5.682 Å) are within 1% of Bi_2WO_6 (a = 5.563 Å; b =

5.605 Å). Although it is not the most stable configuration (within the 30 meV group), it may be accessible through epitaxial growth. This is a valuable direction for further study.

4.4. Conclusion

In studying the configurational space of $BiSbWO_6$, we provided new insight into the behavior of lone-pair electrons in mixed post-transition metal oxides. We showed that the band gap and band edge positions of Bi_2WO_6 can be controlled by manipulating the chemical interactions of WO_6 layers via Sb-in-Bi substitutions. We found that the higher stereochemical activity of Sb 5s lone-pair electrons led to stronger Sb 5s – O 2p hybridization, which upshifted the VBM by up to 0.57 eV. We also showed that local structure distortions due to Sb 5s lone-pair antibonding densities reduced WO_6 octahedral tilting. Increased W 5d – O 2p hybridization in response to the alignment of WO_6 octahedra resulted in greater bonding-antibonding splitting. This was shown to upshift the conduction band edge of $BiSbWO_6$ by up to 0.14 eV. In the case of Sb_2WO_6, reduced octahedral tilting led to a CBM upshift of 0.31 eV. Overall, $BiSbWO_6$ band shifts resulted in narrower band gaps with respect to Bi_2WO_6.

The narrow stability range observed for the six studied $BiSbWO_6$ configurations, with a contribution of 8 meV due to configurational entropy stabilization, suggests a possible mixture of phases during synthesis, which may result in an ensemble averaging of the electronic properties. We suggest one candidate for heterojunction formation due to its low lattice mismatch with Bi_2WO_6. These insights may be further extended and applied to mixed post-transition metal oxides more generally in pursuit of new efficient solar absorbing materials.

Acknowledgements

This work was supported by the National Science Foundation (NSF) grant #1609811. All calculations were performed on Texas Advanced Computing Center (TACC) servers. Additional

support was received from a National Research Foundation of Korea (NRF) grant funded by the Korean government (MSIT) (No. 2018R1C1B6008728).

Chapter 5

Anion Doping

Introductory Comments

The following article investigates the viability of anion doping as a mechanism for VBM upshift and delocalization. S-in-O substitution is carried out in the recently synthesized, theoretically predicted quaternary metal oxide $CuBiW_2O_8$ (CBTO) to improve its low hole mobility, as observed in the experimental study. It is found that, at 50% concentration, the presence of S 3p states significantly upshift the VBM, as well as lower the CBM, and reduce carrier effective masses at both band edges. Hence, anion doping/allotting is determined to improve the PEC properties of CBTO.

The author of the present dissertation is responsible for the abstract, sections 5.1 and 5.2, the introduction of section 5.4, section 5.4.2, and section 5.5.

PHOTOVOLTAIC MATERIALS DESIGN BY COMPUTATIONAL STUDIES: METAL SULFIDES

Edan Bainglass
Sajib K. Barman
Muhammad N. Huda

E. Bainglass, S. K. Barman and M. N. Huda, in Solar Cells, Springer International Publishing, Cham, 2020, pp. 123–138.

Permission has been granted by Springer Publishing Company

Photovoltaic Materials Design by Computational Studies: Metal Sulfides

E. Bainglass, S. K. Barman, and M. N. Huda

Department of Physics, The University of Texas at Arlington, Arlington, TX 76019, USA

Abstract

Materials design for next generation solar cell technologies requires an efficient and cost-effective research approach to supplement experimental efforts. Computational research offers a theoretical guide by applying cutting edge methodologies to the study of electronic structures of newly predicted materials. In this chapter, we present a brief discussion on oxides and sulfides, two promising material groups for photovoltaic applications, and conduct a density functional theory (DFT) study of two sulfide systems: acanthite Cu_2S, and S-doped triclinic $CuBiW_2O_8$. In Cu_2S, we investigate the effects of various cation doping in Cu sites, namely Zn, Sn, Bi, Nb, and Ta, and contrast their electronic structures with that of a previously studied Ag-doped Cu_2S system. A subsequent charge analysis provides a correlation between dopant charge states and detrimental mid-gap trap state concentrations. We then present our best dopant choice for Cu_2S-based photovoltaic systems. Finally, for $CuBiW_2O_8$, a new experimentally-verified DFT-predicted quaternary oxide, the effects of S anion doping in O sites are studied and results indicate favorable photovoltaic properties. This highlights the potential of S anion doping as a mechanism for engineering suitable band gaps for solar cell applications.

5.1. Introduction

Highly efficient, yet cost-effective materials suitable for solar-to-electric energy conversion applications remain both elusive and in great demand, as continued dependence on fossil fuel risks the health of both the environment and the global population[173–175], and energy independence becomes a necessity beyond the economic aspect. Photovoltaic technology is well-established as

one of the most viable candidates for tackling future energy demands. However, the challenge of designing new materials that can meet the host of properties required for efficient solar power conversion is a formidable one. Extensive research has been conducted over the decades in this pursuit, and though advances have been made, photovoltaic technology contributes less than 5% of the electric grid[176]. In part, this is due to the balance required between high efficiency and cost-effectiveness. New materials must be stable and reliable, Earth-abundant, environmentally safe, and inexpensively scalable to meet global demands. To achieve the cost requirement, device efficiencies must be improved beyond the current state. Commercially available Si-based solar cells, for example, range from 18-22% power conversion efficiency[177]. Devices that surpass this efficiency tend to rely either on novel designs[178,179], rare components, isolated conditions, or all of the above, and exist outside of any commercial markets. Other designs utilize inexpensive and abundant components but suffer from efficiencies too low for global scalability. Hence, additional research must be conducted to obtain a better understanding of material properties in hopes of increasing the utilization of solar energy.

Traditionally, scientific breakthroughs in material science and engineering has been achieved primarily through experimental efforts. However, as computational resources became increasingly available, a significant theoretical effort has pushed for deeper investigations of the physical and chemical inner workings of materials[180,181]. Today, computational studies are a common and often essential component of new materials research. They offer a cost-effective and efficient method for large scale materials design and study and have produced countless new materials, as evident in crystallographic databases such as the Inorganic Crystal Structure Database (ICSD), or the Materials Project[121]. In the following sections, we briefly discuss the history of oxides and sulfides, two promising material groups at the frontier of photovoltaic materials

research. We highlight the inherent difficulties and challenges of metal oxides in solar energy conversion applications and introduce sulfides as a promising alternative. Lastly, we present a computational investigation of the electronic properties of Cu_2S, a pure metal sulfide, and a study of the effects of S-doping in $CuBiW_2O_8$, a recently discovered novel quaternary oxide.

5.2. Metal Oxides

Many aspects of PV devices incorporate metal oxide compounds, from transparent conductive layers to transport barrier layers and photoactive light-harvesting layers. Oxides have been utilized in solar cells as insulators, semiconductors, and conductors due to their large range of conductivities[182]. They are non-toxic and abundant in nature due to their ability to form stable chemical bonds with most elements[183]. Many structural flavors of oxides exist including non-crystalline amorphous forms. This overall flexibility is highlighted in the emerging all-oxide solar cell field[15]. Of the various oxide materials, transition metal oxides are especially suited for PV applications. Their partially filled d-orbital character yields properties both unique and complex. Many binary transition metal oxides exhibit band gap energies larger than that of silicon (1.12 eV) and have thus been considered for transparent conducting layers (TCO)[184–186]. However, the requirement of both a wide gap and high conductivity is often at odds due to the band gap property.

For this reason, much research has gone into the effects of dopants on the properties of transition metal oxides in attempt to tailor suitable band gaps. Most doped oxides in solar cells are n-type materials, especially for TCOs[187], due to intrinsic oxygen vacancies, and exhibit high electron mobilities due to strong metal-oxygen orbital overlap[188]. In contrast, highly electronegative O 2p states mixed with localized 3d states at oxide valence band maxima (VBM) hinders shallow acceptor states required for p-type doping and tends to instead result in large hole effective masses[189–191]. In some cases, such as Cu_2O, this challenge is resolved due to the proximity of Cu

3d and O 2p energy levels and intrinsic Cu^{1+} vacancies. Additionally, the ns^2 electronic configuration, e.g. Bi^{3+}, has shown the presence of anti-bonding states at the VBM, which, through hybridization with O 2p states, can lead to reduced effective masses and higher hole mobilities[192]. This is analogous to the chemical modulation technique[193] of O 2p – Cu 3d VBM hybridization, which has yielded dispersive valence bands in Cu(I) ternary oxides. The technique has since been extended to the chalcogen group, as Cu 3d orbitals hybridize better with S, Se, and Te p orbitals[194,195]. Cu_2O has also been utilized as a light-absorbing layer due to its 1.4 – 2.2 eV band gap[196] resulting in power conversion efficiencies of ~8%[197]. According to the Shockley-Queisser detailed balance limit[198], the band gap of Cu_2O can, at best, reach a ~22% theoretical conversion efficiency. On the other hand, cuprous oxide (CuO) has a theoretical efficiency limit of ~31% owing to its 1.4 eV band gap[199]. However, CuO has yielded poor efficiency thus far, which has been attributed to high defect concentration or interface recombination[200,201]. Some improvements to CuO efficiencies were found in the nanoscale, reaching an efficiency of 2.88%[202].

To enhance the efficiencies of Cu-based oxides, we must pay careful attention to the challenges inherent in the oxide group. Oxides tend to be wide-gap semiconductors due to the high electronegativity of oxygen. Furthermore, 3d transition metal oxides suffer from greater localization at the band edges which generally results in large carrier effective masses. Thus, a study of different anion species may be required. Several of these have been studied in the scope of solar fuel generation, including the nitride and sulfide groups, as well as Se (CIG(S,Se)) and Te (CdTe). Theoretically, the reduced electronegativity of these species with respect to oxygen is expected to upshift the VBM, thus providing a mechanism for band gap engineering.

5.3. Sulfides

Cu-chalcogenides are well-known energy harvesting materials, especially in photovoltaic applications. These materials are composed of Cu^{1+} cations and chalcogen anions such as S, Se, Te. Chalcogenides may also include other cations along with Cu from groups IIB, IIIA, IVA and VA. Such compounds include $Cu(In,Ga)(S,Se)_2$ and $Cu_2ZnSn(S,Se)_4$, or CIG(S,Se) and CZT(S,Se), respectively, both regarded as prominent solar cell absorbers. Apart from these complex multinary compounds, the binary Cu-chalcogenide Cu_2S has also been found to be a promising solar absorber due to its suitable band gap of 1.2 eV. Of these, a CIGS-based solar cell was found to be superior due to its high solar conversion efficiency of nearly 20%, which was first reported by NREL[203]. Several other materials have shown similar efficiencies, including Si, GaAs, CdTe, and the perovskite group. However, Ga, In, Cd and Te are relatively scarce and very expensive. And even though Si-based technologies are widespread around the globe, pure grade Si is not cost-effective, and thus unsuitable to meet the global solar energy demand. In contrast, CZTS- and Cu_2S- based solar cells, with reported solar-to-light conversion efficiencies of 12.6%[204] and nearly 10%[205], respectively, can be cost-effective alternatives in this respect due to the abundance of Cu, Zn, and Sn in Earth's crust, and their eco-friendly, non-toxic nature.

To meet future energy demands and replace fossil fuel with cost effective alternatives, thin film based solar cells are so far the best candidate since they require less material and provide a pathway to go beyond the established Si-based solar cell technology[206,207]. However, both CZTS and Cu_2S suffer from some intrinsic drawbacks which require careful attention and proper study to develop the necessary solutions. Defect-free synthesis of CZTS is rather challenging. Due to the similar ionic radii and tetrahedral coordination of Cu and Zn, the cations may swap their lattice sites with relative ease. In addition, annealing multinary compounds at high temperatures during

synthesis results in defects to the crystal and electronic structures, which would eventually impact device activity[208]. In an earlier study, we have shown by thermodynamic consideration, that defects would destabilize single phase stability of CZTS[45]. Although Ba-substitution in Zn sites, leading to the chalcogenide family $BaCu_2SnSe_xS_{4-x}$ (BCT(S,Se)), provides a mechanism for controlling the coordination environment, the resulting conversion efficiency is well below expectation[209]. As a counterpart to multinary complex chalcogens, Cu_2S itself suffers from intrinsic p-type defects due to spontaneous Cu vacancy formations in the crystal. Hence, the performance of Cu_2S-based thin-film solar cells degrades in air over time. Careful crystal stability and electronic structure studies, along with possible doping effects on this material, may shine light on the prospect of its photovoltaic use in the near future.

5.4. Case Studies

The density functional theory (DFT) methodology shifts the quantity of interest in electronic calculations from the wavefunction, a multidimensional complex vector quantity, to the 3-dimentional electronic density scalar. It establishes a one-to-one correlation between the two quantities, and defines an energy functional of the latter, which can then be variationally minimized under constraint leading to the ground state density of the system. With this quantity in hand, and via the one-to-one correlation with the wavefunction, all properties of the system are now obtainable. The mathematical rigor of the theory is encapsulated in the Hohenberg-Kohn theorems[56]. Applications of it involve iterative solutions of the so-called Kohn-Sham equations[57], a set of one-electron Schrödinger-like equations describing a fictitious non-interacting system that, by construction, leads to the same ground state density as the real, interacting system of interest. The theory has seen tremendous growth over the past 50 years and has since become a staple in the

study of electronic structures of materials[52,210–213]. One of its many success is the reproducibility of experimental results[214].

In the following subsections, we discuss results from two separate DFT studies of Cu(I) systems with a focus on photovoltaic properties. First, we address the properties of sulfides by studying the effects of doping on the relatively new acanthite phase of Cu_2S. Then we present a study of the effects of S-doping on the novel $CuBiW_2O_8$ quaternary oxide, dubbed CBTO. In both studies, the generalized gradient approximation of Perdew-Burke-Ernzerhof (GGA-PBE)[66,67] was used to model exchange-correlation effects. The Kohn-Sham equations were solved in plane wave form, as implements in the Vienna *ab initio* Simulation Package (VASP 5.4.4)[103,104], under the pseudopotential frozen-core approximation of the projector augmented wave (PAW)[84,102] method. Plane wave kinetic energy cutoff values of 520 eV and 600 eV were used for Cu_2S and CBTO, respectively. Reasonable convergence criteria were used for ionic relaxations (≤ 0.01 eV/Å in ionic forces) and electronic densities ($\leq 10^{-6}$ eV in total energy). Brillouin Zone (BZ) integrations were performed on a $7 \times 3 \times 3$ Γ-centered k-point mesh for Cu_2S, and a $7 \times 7 \times 7$ Monkhorst-Pack[83] mesh for CBTO. A smaller $5 \times 5 \times 5$ mesh was deemed sufficient for S-doped CBTO via convergence testing. Due to the well-known underestimation of band gap energies by pure DFT calculations, further exacerbated in localized d-electron systems[73,108,169], the Hubbard U parameter was applied (DFT+U) on Cu 3d to enhance on-site Coulomb interactions following the methodology of Dudarev[77]. An effective U value of 7 eV was used in the case of Cu_2S, while a value of 6 eV was used for CBTO, both adopted from previous studies[49,215]. The different values are due to the unique chemical environments of the two systems. We note that the Bader charge analysis[87,111–114] conducted on doped Cu_2S was derived from a pure GGA-DFT calculation.

5.4.1. Cu_2S

Of the many experimentally known phases of Cu_2S[216–220], only the monoclinic low chalcocite structure forms below 104 °C (fig. 5.1a). Cu_2S-based thin film solar cells have previously shown efficiencies near 10%[205,221]. However, the tendency to spontaneously form Cu vacancies in all phases, and the consequent excessive p-type doping in the crystal, makes Cu_2S behave as a degenerate semiconductor[222,223]. Hence, the efficiency of Cu_2S-based solar cells degrades over relatively short time periods[224,225]. Recently, a new phase of Cu_2S known as acanthite[226] (fig. 5.1b) was computationally derived from a materials database search and found to be thermodynamically more favorable than its naturally occurring counterpart (low chalcocite). Despite the new phase not showing any indication that its tendency for Cu vacancy formation is any less than that of low chalcocite, a theoretical study did show that Ag alloying in the acanthite phase can reduce this tendency, as well as control the diffusion of Cu ions inside the crystal structure[215]. The study also found that the electronic band gap of the acanthite phase may be increased with Ag alloying without introducing any intermediate or defect states to its band structure. This suggests the potential for tailoring a suitable band gap for photovoltaic applications via Ag alloying in Cu_2S.

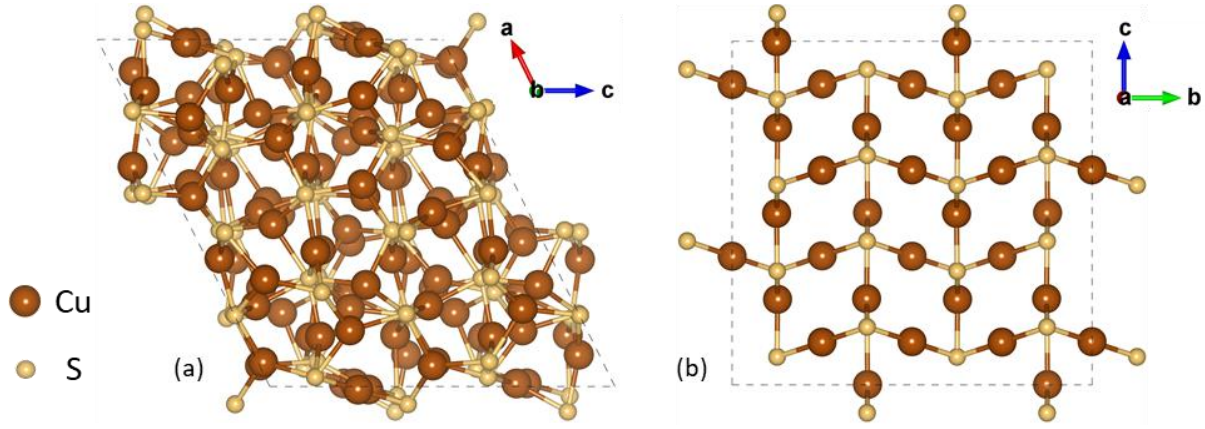

Figure 5.1. The crystal structures of (a) low chalcocite and (b) acanthite phases of Cu_2S. The low chalcocite has 96 Cu and 48 S atoms. The acanthite phase is presented as a 3 x 2 x 2 supercell for comparison. The unit cell of acanthite has 8 Cu and 4 S atoms.

Experimentally reported band gaps for Cu_xS ($1 \leq x \leq 2$) are all within 1.1-1.2 eV. A recent study of silver copper sulfides comprising both experimental and theoretical efforts demonstrated promising electronic structures for AgCuS (stromeyorite) and Ag_3CuS_2 (jalpaite), both suitable for high efficiency solar cells[227]. Hybrid density functional theory was implemented in band gap calculations yielding 1.27 eV and 1.05 eV, respectively for AgCuS and Ag_3CuS_2. Hence, Ag doping of Cu sites, or Ag alloying in the crystal structure, offer an opportunity to tune the band gap of Cu_xS-based materials for photovoltaic applications.

It was also reported in a separate study that favorable growth of Cu_2S thin-film interfaces with suitable metal oxide thin-films such as TiO_2 and Al_2O_3 could help stabilize the intrinsic Cu vacancy formation and minimize the Cu diffusion in the system[228]. As an earth abundant, non-toxic, and relatively cost-effective alternative, this material may provide the best outcomes compared to other ternary and quaternary materials currently available. However, understanding the fundamental characteristics of the electronic structures of the different phases of Cu_xS and the effects of various doping schemes requires more attention. For example, it is known that the low chalcocite phase of Cu_2S has a very complex crystal structure consisting of 96 Cu and 48 S atoms per unit cell. The Cu atoms are distributed in 24 symmetrically inequivalent sites within the crystal structure. This renders computational studies highly expensive and inefficient. On the other hand, the acanthite phase has only two inequivalent Cu sites. Hence, defect related studies in this phase are far easier and become computationally feasible. Our recent investigation[229] shows that doping Cu sites in the acanthite phase reproduces the effects of doping on the low chalcocite phase. Thus, the simpler acanthite phase presents a computationally feasible alternative for defect related electronic structure studies. Furthermore, the established structural correspondence allows results to be extrapolated to the more complex low chalcocite phase. We next present band structures and

corresponding density of states for Ag, Zn, Sn, Bi, Nb, and Ta doping of Cu sites in the acanthite phase of Cu_2S.

Results Show that Ag doping does not introduce any intermediate or defect mid-gap states, as was previously shown[215]. (fig. 5.2). The DOS plot shows that the compositions of both the valence band maximum (VBM) and the conduction band minimum (CBM) are similar to those found in pristine acanthite and low chalcocite phases (fig. 5.2). Added Ag 4d states are found deep in the valence band and do not contribute to the band edges. Under Zn doping, the Fermi level shifts up in energy, as the higher charge state of Zn with respect to Cu causes Zn 4s electrons to partially occupy the CBM. This adds extra charge carriers to the system, making it an n-type semiconductor. For Sn doping, a defect related, or intermediate mid-gap state is observed about the Fermi level. The DOS plot shows that the band is primarily composed of Sn 5p and Cu 3d. This kind of band is known to affect the photo-absorption of the system. A similar effect occurs in Bi doping, where Bi 6p shows significant contributions to both band edges. These phenomena become more pronounced in Nb and Ta doping, which suggests that the higher the charge states of the dopant, the more defect bands it introduces to the system, causing the material to tend towards a metallic character. We note that these effects appear to be limited to the CBM, as the shape of the VBM is retained in all doping scenarios. A Bader charge analysis of Cu_2S (table 5.1) shows that Ag and Cu have near identical charge states, while Sn is almost twice that value. It is now evident that the coordination of a dopant in the system correlating to its charge state will have a direct effect on the electronic structure of the system. Thus, due to the proximity of the charge states of Ag and Cu, we conclude that the defect-free band gap and favorable crystal structure of Ag-doped acanthite Cu_2S makes it the best candidate to tailor for a suitable band gap and optical absorption.

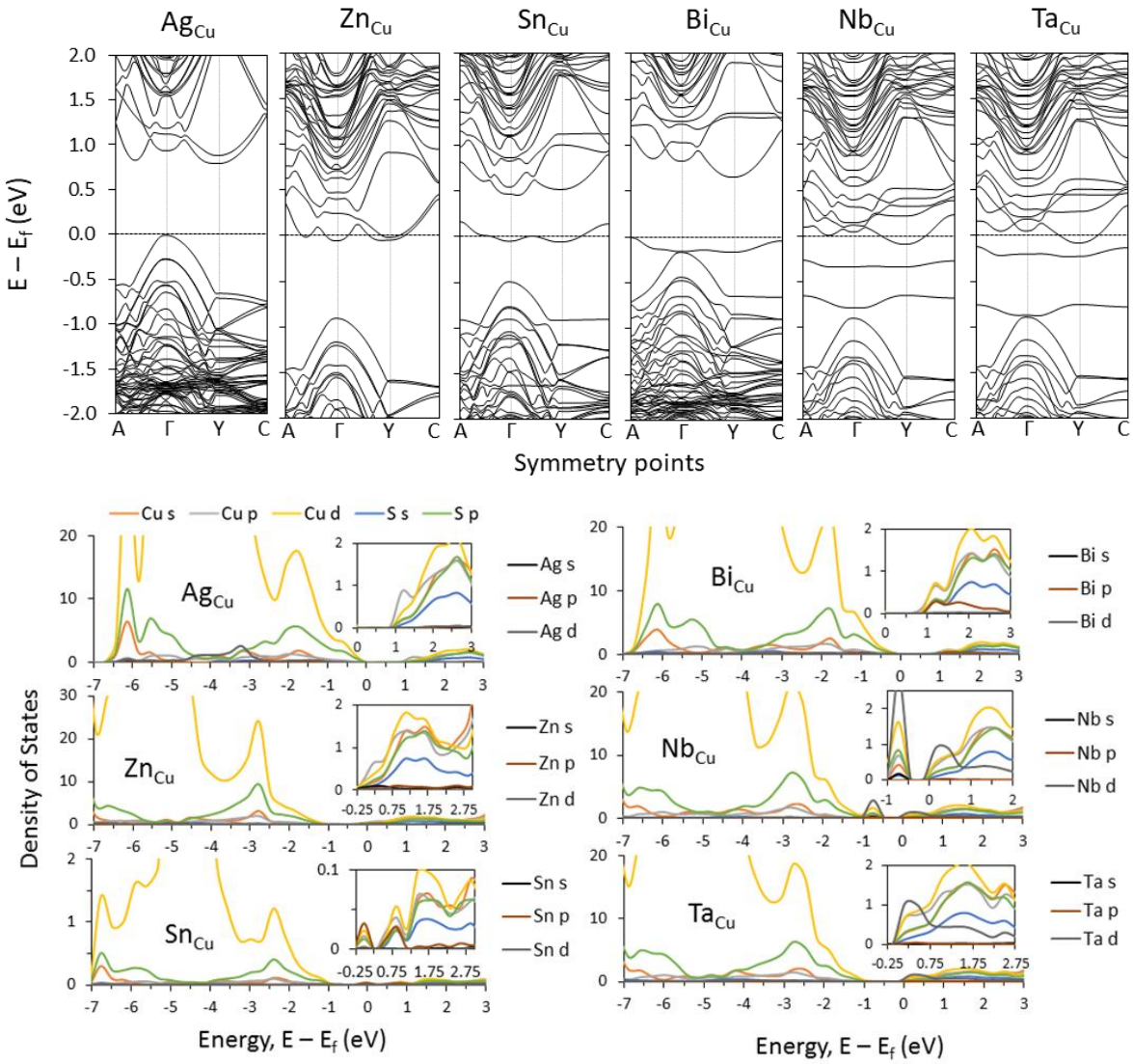

Figure 5.2. GGA+U calculated band structures (top) and density of states plots (bottom) for Ag, Zn, Sn, Bi, Nb, and Ta doping (Separately) of a single Cu site, denoted as M_{Cu}, in 2 × 2 × 2 supercells (64 Cu and 32 S atoms) of Cu_2S acanthite. The Fermi level is set to 0 eV. The density of states (DOS) is given in arbitrary unit. Ag plots are included for comparison. Ag_{Cu} and Zn_{Cu} introduce no intermediate or defect mid-gap states. However, the CBM in Zn_{Cu} shifts to a lower energy and intercepts the Fermi level. For Sn_{Cu}, an intermediate band is introduced at the Fermi level, which is composed of both occupied and unoccupied states. Meanwhile, Bi_{Cu} occupies a band from the CBM and moves it below the Fermi level. For Nb_{Cu} and Ta_{Cu}, the system shows near-metallic characteristics.

Table 5.1. Calculated average Bader charge states of different species in doped Cu_2S.

Average Bader charge states							
Cu	Ag	Zn	Sn	Bi	Nb	Ta	S
+ 0.37	+ 0.30	+ 0.71	+ 0.66	+ 0.52	+ 1.23	+ 1.28	- 0.74

5.4.2. $CuBiW_2O_8$:S

A recent computational materials prediction study by Sarker et al. suggested a triclinic ground-state structure for the quaternary Cu(I)-oxide CuBiW2O8[49], or CBTO, for potential photovoltaic application. For the DFT-predicted structure, an indirect band gap was calculated at 1.43 eV, well suited for absorptions in the visible range. Calculated optical absorption spectra showed a slightly higher optical band gap of ~1.49 eV, which was attributed to O 2p – W 5d transitions with O 2p situated slightly below the VBM. This is because the Cu 3d (VBM) – W 5d (CBM) transitions are forbidden by quantum selection rules, and Bi 6p contributions at the CBM are relatively small. Analysis of the band structure of CBTO found no mid-gap Cu 3d states, as compared to those found in $CuWO_4$ thought to cause its high resistivity. Furthermore, dispersive bands were found at the CBM, indicating low electron effective mass and high mobility. However, the top of the valence band was quite flat, indicating less favorable hole mobilities. The ns^2-md^0 electronic configuration, exhibited by Bi-W-O systems, has been suggested as a mechanism for reducing hole effective masses via the introduction of dispersive anti-bonding s orbitals at the top of the valence[27,89]. The contrary result in CBTO may then be due to occupied and highly localized Cu 3d states at the VBM, which are slightly higher in energy than Bi 6s states.

CBTO was previously synthesized over 27 years ago[230], though no data regarding its optical and electronic properties was provided in the report. However, a recent collaborative study[50] of the quaternary compound successfully yielded the predicted triclinic structure via solid state synthesis methods performed in a Cu-rich environment. Moreover, the study provided the first measurements of the optical, electrical, and photoelectrical properties of CBTO. Light absorption measurements yielded an indirect band gap of 1.46 eV, as compared to the 1.43 eV gap produced from photoluminescence spectroscopy – both in excellent agreement with the theoretical value.

Hall effect measurements determined CBTO to be a p-type semiconductor, as expected for Cu(I)-oxides, with hole majority carrier mobility of 0.32 $cm^2V^{-1}s^{-1}$ and carrier lifetime of 2.12 ns. The diffusion length was calculated at ~42 nm, a value comparable to that of $BiVO_4$[231], an ns^2-md^0 material well known for its good light absorption and transport properties.

To improve hole carrier mobility, as well as the band gap energy, we look towards S-doping in CBTO. These improved outcomes are expected from the lower electronegativity and ionization potential of sulfur with respect to oxygen. Thus, as a dopant, S is expected to upshift the VBM and narrow the band gap. Additionally, due to the proximity of their energy states, S 3p is expected to hybridize with Cu 3d at the VBM. Therefore, the localized Cu 3d character of the VBM should give way in part to the more dispersive S 3p states, consequently reducing hole effective mass. The electronic properties of CBTO:S are investigated within the framework of DFT under similar conditions considered in the original CBTO study, as outlined earlier. However, since the publication of the original computational work, a lower ground state structure of CBTO was derived from $CuBi_2O_4$[232–234]. Calculated XRD peaks for the new triclinic structure were found to be a better match with the experimental diffraction patterns. For this reason, the new $CuBi_2O_4$-derived CBTO structure was used in the current study (fig. 5.3).

The affinity of S to Cu becomes apparent at the single S-in-O site doping level, with S pulling Cu towards it, hybridizing its 3p orbitals with Cu 3d states at the VBM. This is due to the proximity of Cu 3d and S 3p electron energies, as mentioned above. Moreover, as S distorts the Bi octahedron, the now closer Cu 4s orbitals hybridize with Bi 6p and significantly decrease in density at the VBM. The linear O-Cu-O bond found in the pristine cell bends towards angles reminiscent of the S-Cu-S network of the low chalcocite Cu_2S phase, which leads to sharper, more localized

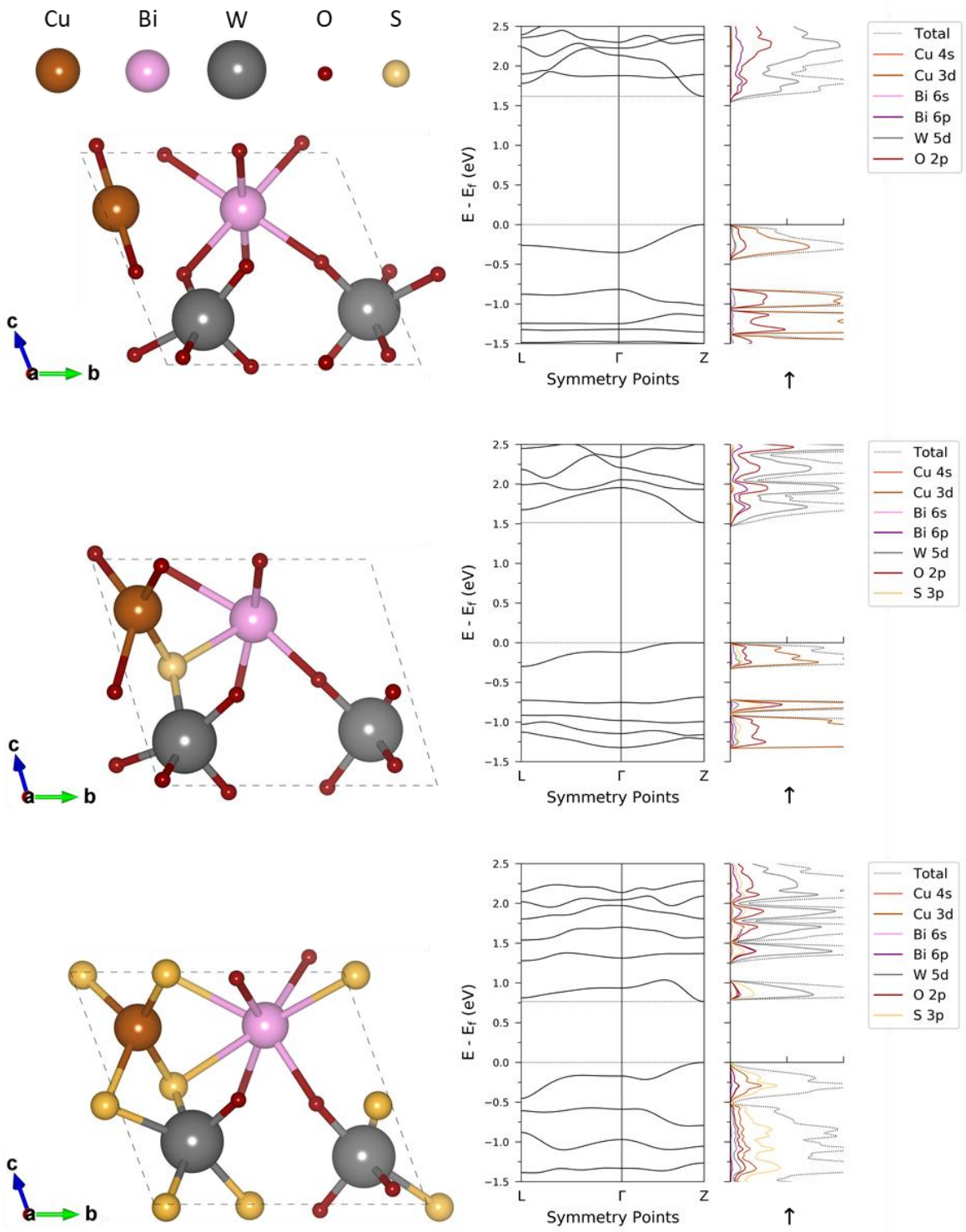

Figure 5.3. Unit cells, band structures, and density of states plots for pristine CBTO (top), single S-in-O doped CBTO (center), and 50% S-doped CBTO (bottom). Symmetry points were obtained from AFLOW[110]. Densities are plotted in arbitrary units. Pristine CBTO contains 1 Cu, 1 Bi, 2 W, and 8 O atoms. Doping was applied to the unit cell to model high S concentrations. Band gap energy decreases from 1.618 eV (pristine) to 0.766 eV (50% doping) due to increasing interactions along the Cu-S-W network. S 3p hybridization at both VBM and CBM reduces effective masses of both charge carriers.

Cu 3d and W 5d densities. The top of the valence flattens, with a calculated hole effective mass of 7.19 m_0, as compared to 2.16 m_0 in pristine CBTO. Electron effective mass increases slightly from 0.68 m_0 to 0.87 m_0. The band gap is reduced to 1.534 eV, compared to the 1.618 eV calculated for the new CBTO structure. The narrowing of the gap is not due to an increase in the VBM, as expected, but rather a decrease of both band edges. This may be due to asymmetric distortions caused by the 1:3 ratio of S-to-O coordination about Cu atoms. The gap remains direct about the high symmetry Z point. The CBM character exhibits similar localization, with a slight increase in Cu 4s and Bi 6s contributions, though far less than the primary contributions from empty Bi 6p, O 2p, and W 5d states.

The localization effect is not limited to Cu and W orbitals and is observed throughout the electronic landscape. This effect intensifies with additional S-doping as the cell is transitioned to a 50/50 S-in-O doping level, where the lowest energy configuration is obtained with Cu fully bonded to the 4 S sites (fig. 3). More pronounced effects are observed at this level of doping. All cation-cation distances are increased as the larger S pushes atoms away from previously O-occupied sites. This is true for all but neighboring Cu and W atoms, where the distance decreases with respect to the pristine structure. This is caused by the increased attraction of the Cu-S environment. With the now fully coordinated CuS_4 cluster, the Cu-S-W network becomes the primary photoactive site. This is highlighted in the density of states, in which, as expected, the VBM sees a primary S 3p contribution over that of Cu 3d. At the conduction band, Bi 6p and O 2p hybridize more strongly than at the single S-doping level. More importantly, as the S 3p density of states increases about the Cu-S-W network, the W-S bond length decreases by ~0.2 Å leading to greater W 5d – S 3p hybridization at the CBM. As a result, the CBM detaches from the rest of the conduction band and shifts down below 1 eV, reducing the band gap to 0.766 eV. Here, the narrow

gap is indeed caused by a VBM upshift of 0.461 eV, as expected, in addition to a CBM downshift of 0.391 eV. Despite the increased localization, both electron and hole effective masses are reduced with respect to the pristine cell, with 1.99 m_0 for holes and 0.43 m_0 for electrons, suggesting an overall increase in carrier mobility for CBTO:S_4. Hence, S-anion-doping in CBTO may lead to improved electronic properties suitable for photovoltaic applications.

5.5. Summary & Conclusions

In this chapter, we have outlined the benefits and effectiveness of computational studies applied to new materials research for photovoltaic applications. An overview of oxides was provided including the success of the material group, as well as some of the remaining difficulties it faces. As a viable alternative, sulfur-based solar absorbers were discussed in detail, with emphasis on their potential for suitable photovoltaic material properties. Two case studies were presented, discussing first the electronic properties of the pure sulfide compound Cu_2S, and second, the effects of S-doping in the novel quaternary oxide CBTO. In Cu_2S, we showed that Zn doping leads to partial occupation of conduction band minima by 4s electrons, increasing charge carrier concentrations resulting in a n-type material, while the remaining dopants introduce intermediate defect states leading to metal-like characteristics. A correlation between dopant charge states and mid-gap defect state concentrations was suggested, with lower charge state dopants deemed favorable for photovoltaic applications. By comparing these results to Ag, which has previously been shown to minimize intrinsic Cu vacancies and diffusion, as well as increase the band gap without introducing detrimental mid-gap trap states, we conclude that Ag alloying is the best candidate for band gap engineering in Cu_2S systems. For S-doped CBTO, S-in-O anion doping was shown to cause distortions in the pristine unit cell forming a photoactive Cu-S-W network through S 2p – Cu 3d and S 2p – W 5d hybridizations at the VBM and CBM, respectively. These interactions lead

to widespread localization of electron densities in the material. Despite the localization, S 3p hybridizations reduce overall charge carrier effective masses and narrow the band gap below 1 eV. This suggests that anion doping may provide an additional mechanism for tailoring suitable photovoltaic material properties.

Acknowledgements

All computations were performed on Texas Advanced Computing Center (TACC) servers. We acknowledge Dr. Pranab Sarker for the discovery of the new triclinic ground state of CBTO. This work was partially funded by NSF grant # 1609811.

Chapter 6

Surface Analysis

Introductory Comments

As mentioned in chapter 5, low hole mobility was measured in $CuBiW_2O_8$ (CBTO). This was attributed to the presence of Bi_2WO_6 impurities on the surface of CBTO. Subsequent theoretical calculations carried by the author of the present dissertation determined that the persistence of the impurity is a thermodynamic artifact and not related to the particular experimental setup. Additionally, theoretical calculations of the band offset between CBTO and Bi_2WO_6 suggest that the latter may act as an electron trap and recombination site. To better understand the effects of Bi_2WO_6 on the electronic properties of CBTO, a more thorough study of their interface is warranted. The following manuscript provides the preliminary surface analysis of CBTO stoichiometric surfaces required to develop such an interface. The study also offers a guideline for obtaining accurate surface energies computationally when investigating complex oxide surfaces.

The theoretical contributions of the author of the present dissertation to the manuscript addressing the experimental synthesis of CBTO are not included in the present dissertation. The full author list of that manuscript is added here as a footnote[1].

[1] L. Zhou, B. Giri, M. Masroor, E. Bainglass, L. Guangjiang, A. Carl, R. L. Grimm, M. N. Huda, L. V. Titova and P. M. Rao, *Submitted*.

LOW-INDEX STOICHIOMETRIC SURFACES OF $CuBiW_2O_8$

Edan Bainglass
Muhammad N. Huda

Bainglass, E. & Huda, M. N. Low-Index Stoichiometric Surfaces of $CuBiW_2O_8$. *Surf. Sci.* **705**, 121762 (2021).

© 2020 Elsevier B.V. All rights reserved.

Low-Index Stoichiometric Surfaces of $CuBiW_2O_8$

E. Bainglass and M. N. Huda

Department of Physics, The University of Texas at Arlington, Arlington, TX 76019, USA

Abstract

$CuBiW_2O_8$ (CBTO), a theoretically predicted, recently synthesized novel quaternary metal oxide, has been identified as a promising solar light absorber. In the present paper, the surface properties of CBTO are studied to further examine the applicability of the material for solar energy applications. Surface studies of quaternary oxides via first principles methods are rare in the literature. We present here a systematic approach to identifying stable surfaces and the origin of their stability. First, the emergence of the electronic properties from the interplay of cations is explored in bulk CBTO. Calculated XRD data is used to label the surfaces on the experimental XRD plot. For the dominant low-index stoichiometric surfaces, we calculate surface bond strengths, cleaving energies, and surface energies via the slab model within periodic boundary conditions. To calculate the surface energies of a quaternary oxide such as CBTO, we review the existing methodologies and propose a guideline for defining the lower and upper bounds of the slab thickness used in the linear fit model. Surface energies are then used to predict the equilibrium crystal shape via Wulff construction.

6.1. Introduction

Quaternary oxides offer wide-range tunability of their electronic properties due to their large chemical composition space. Recently, there have been efforts to predict and synthesize multi-cation oxides possessing desirable electronic properties for applications in diverse fields. One such novel quaternary oxide, $CuBiW_2O_8$ (CBTO), which has been identified as a promising solar absorber, was theoretically predicted[49], and has recently been synthesized for the first time

using a tailored Cu-rich solid-state synthesis method[50]. Light absorption and photoluminescence measurements both showed a direct band gap of 1.92 – 1.97 eV. Hall Effect measurements found holes as the majority carrier, with p-type conductivity attributed to the spontaneous formation of Cu-vacancies, a known tendency of Cu^{1+} p-type semiconductors[235–237]. The relatively low Hall mobility of 0.32 $cm^2V^{-1}s^{-1}$ measured for CBTO was identified as a challenge to its solar absorbing performance. Furthermore, the carrier diffusion length was found to be shorter than the optical absorption depth. This was explained as the result of defect-associated trap states both in the bulk and at the surface. Our theoretical calculations determined that Bi_2WO_6 impurities are thermodynamically stable at synthesis conditions. These impurities were experimentally detected via X-ray diffraction (XRD) analysis of the synthesized CBTO sample. Scanning electron microscopy (SEM) and energy-dispersive X-ray spectroscopy (EDS) analyses confirmed the presence of Bi_2WO_6 impurities at the sample surface, which, as determined by subsequent calculations of the band offset at the CBTO/Bi_2WO_6 interface, may act as recombination sites. However, though repeated annealing cycles were unable to completely eliminate Bi_2WO_6, they did greatly reduce its concentration.

To efficiently extract charge carriers from CBTO, one approach would be to make it a thin-film absorber, in which surface properties would play a dominant role. In addition, a heterojunction between p-type CBTO and an n-type material would further facilitate carrier extraction. For optimal charge injection through a p-n junction interface, the band offset between the interfacing materials would need to be aligned in a favorable manner. In general, band offsets depend on the electrostatic potential across the interface, which is sensitive to the specific terminations of the interfacing surfaces. From a theoretical and practical perspective, a low degree of lattice mismatch between the interface components is desired to avoid excessive surface strain. Thus, to study an

interface involving CBTO would first require a good understanding of its surface properties, for all possible stable and cleavable surfaces, which have yet to be explored. Surface studies of quaternary oxides via first principles methods are rare in the literature due to complexities related to the modeling of low-index stoichiometric surfaces and the estimation of their stability from calculated surface energies. Computationally, periodic slab model calculations can be exceedingly expensive for metal oxides and pose a significant challenge for complex quaternary oxides.

In the present work, we investigate a large set of CBTO stoichiometric surfaces and discuss their relative stability, atomic structure, and electronic properties. First, we explore the emergence of the electronic properties from the interplay of cations in bulk CBTO. The structural results are then used to develop a labeled theoretical XRD diffraction pattern and predict the crystalline shape of CBTO. Both are compared against the recent experimental results. To address the complexity of calculating surface energies for CBTO, we first review the existing methodologies from the literature, discuss their limitations when applied to complex oxides, and propose a modified strategy. We then perform a systematic and thorough study to understand the trend of surface energies among the several stable stoichiometric surfaces of CBTO. The quaternary nature of CBTO offers multiple layers of complexity arising from its specific surface terminations. The propensity to compensate the unsaturated charges on surface ions drives the stability competition among the surfaces. Hence, the number of broken metal-oxygen bonds at the terminated surface plays an important role not only to its stability, but also to its electronic signature. The consequent processes of surface relaxation and surface reconstruction are discussed from the perspective of atomic displacements at the surface. We highlight their role in determining the resultant surface stability trend in CBTO. Surface effects on the electronic structure are also used to justify the most stable surfaces.

6.2. Methodology

6.2.1. Computational Details

Total energies are calculated using the plane wave formulation of density functional theory (DFT)[56,57], as implemented in the Vienna *ab initio* Simulation Package (VASP 5.4.4)[103,104]. We consider the following valence electron configurations: Cu $\{3d^{10}3p^{6}4s^{1}\}$; Bi $\{6s^{2}5d^{10}6p^{3}\}$; W $\{5p^{6}6s^{2}5d^{4}\}$; O $\{2s^{2}2p^{4}\}$. Core electrons are treated with the projected augmented wave (PAW) method[84]. The generalized gradient approximation formalism of Perdew, Burke, and Ernzerhof (GGA-PBE)[66,67] is used to account for exchange and correlation effects. A DFT+U approach is taken to better account for d-electron localization and correct for the known underestimation of band gap energies by GGA functionals. Following the original predictive work of Sarker et al.[49], we apply an effective U of 6 eV to Cu 3d orbitals as an on-site Coulomb correlation. Bulk Brillouin zone integrations are performed on $3 \times 3 \times k_3$ Monkhorst-Pack[83] k-point grids utilizing gaussian finite temperature smearing with σ (k_BT) = 0.01. For slab calculations, k_3 is set to 1 due to the broken symmetry at the surface. The tetrahedron smearing method[106] is utilized for density-of-states (DOS) calculations on finer $7 \times 7 \times 1$ k-point grids. A plane wave cutoff of 600 eV is used in all calculations. Total slab energies are converged to within 1 meV with respect to both the size of the k-point grid and the plane wave cutoff value. Band structures are calculated along special symmetry k-points in the $B_1 \times B_2$ reciprocal lattice plane. Charge density difference plots are drawn with an isosurface level of $\pm$ 0.035 $Å^{-3}$. The Henkelman group implementation[111–114] of the Bader charge analysis[87] is used to estimate partial charges.

6.2.2. Surface Bonding Strength

As a first approximation, we employ a measure of surface bond strength by considering the following: (i) shorter bond lengths tend to indicate stronger bonds; and (ii) surfaces with higher

bond density are more resistant to cleaving. The bond strength per unit area, S, can then be expressed as

$$\mathrm{S} = \frac{1}{\mathrm{A}} \sum_{\mathrm{i}} \left(\frac{\mathrm{n}}{\mathrm{l}} \right)_{\mathrm{i}} \tag{6.1}$$

where n and l are respectively the number and length of the i^{th} unique bond cleaved, and A is the area of the given slab. Though this does not account for the unique properties of each element, it can provide a general trend for the work involved in cleaving a surface from the bulk.

6.2.3. Surface Energy

The standard definition for the surface energy σ of a material modeled as a symmetric, semi-infinite, vacuum-terminated, N-layer slab, is given by

$$\sigma = \lim_{\mathrm{N} \to \infty} \frac{1}{2} \left(\mathrm{E}_{\mathrm{slab}}^{\mathrm{N}} - \mathrm{NE}_{\mathrm{bulk}} \right) \tag{6.2}$$

where E_{slab}^{N} is the total energy of the slab, and E_{bulk} is the energy of the bulk material normalized to a single slab layer. The $1/2$ term accounts for the top and bottom surfaces of the slab arising from periodic boundary conditions. The vacuum thickness is chosen to be large enough such that the periodic surfaces do not interact across the vacuum. In the present study, a vacuum of 20 Å is added to all slabs along the finite axis. In similar fashion, the slab thickness, a function of N, is chosen such that a central region of the slab may be defined as the "bulk" and considered to be negligibly affected by the broken periodic symmetry at the surface. Though not a requirement, in the current study, we choose to work with odd N slabs. Each slab is of $N = 2M + 1$ thickness, with M being the number of layers on either side of the central "bulk" layer, which is kept frozen during relaxation. Lastly, slab symmetry is required to avoid dipole moments[238] across the slab, as well as to maintain the validity of the second term in eq. 6.2. In complex systems, achieving symmetry is often a challenge. Though CBTO is centrosymmetric and thus affords some ease in this

matter, we do include a dipole correction term[239,240] in the DFT Hamiltonian for all surfaces to reduce any modeling-related dipole moments.

Surface energies obtained from eq. 6.2 using E_{slab}^{N} calculated for an unrelaxed slab are representative of cleaving energies. Cleaving energy is that energy necessary to separate the two surfaces from a continuous bulk. This assumes that at the instant of cleaving, the atomic configuration of the cleaved surfaces is that of the bulk material. Hereafter, when surface energies are not explicitly referred to as cleaving energies, they are to be understood as obtained from eq. 6.2 using E_{slab}^{N} calculated for relaxed slabs. It then follows that the surface energy of a given surface represents the sum of its respective cleaving energy and relaxation energy – that energy incurred in the process of relaxing the surface.

It is known that σ tends to diverge with increasing N when E_{bulk} is obtained from a separate bulk calculation[241]. Several methods have been developed to overcome this problem. Of these, the most often used is the linear fit method of Fiorentini and Methfessel[242]. Here, eq. 2 is first rearranged as follows

$$\mathrm{E_{slab}^{N}} = \lim_{\mathrm{N}\to\infty}(2\sigma + \mathrm{NE_{bulk}}) \tag{6.3}$$

and understood to be exact in the infinite slab limit. Using this linear relation, one can extract E_{bulk} by plotting the total energies of slabs of increasing thickness, excluding the thinnest slabs, until convergence of E_{bulk} is achieved. The divergence problem vanishes due to the use of a single model – the slab model – in obtaining both slab and bulk energies. Some uncertainty lies in the choice of the initial slab thickness considered in the linear fit model. Similarly, the value of N corresponding to sufficient slab thickness is, in general, not easily surmisable. There is also a significant computational cost associated with the use of multiple slab calculations. For these reasons, other methods have aimed at reducing the cost by limiting the number of necessary calculations.

Da Silva et al.[243] argued that the origin of the divergence problem lies in inconsistencies between the levels of accuracy used to compute the energies of the slab and bulk models. They showed that the problem could be avoided by using identically high levels of accuracy for both models. Though their results support the argument and were obtained from a single calculation per model, the computational cost associated with the use of densely packed k-point grids required for high accuracy can surpass the total cost of multiple lower-level slab calculations. This was addressed in a study by Sun and Ceder[244], in which the authors argued that the inconsistencies between the two models arise primarily from an unequal sampling of the Brillouin zone. Specifically, the k-point grid in the surface plane on which the Kohn-Sham integrals are evaluated is unequally generated in the two models due to the unique geometry of surface planes. To overcome this, Sun and Ceder suggested obtaining E_{bulk} from a transformed-bulk model with a basal plane matching the lattice of the slab model parallel to the surface. An automatically generated k-point grid would then yield the same $k_1 \times k_2$ grid in the basal plane as the slab model. Following this approach, they showed that a similar accuracy may be reached as that of the Da Silva method, though with far smaller grids, and at a more reasonable cost.

Though enticing, we note that Sun and Ceder only tested their method on metallic surfaces, as did Da Silva et al., likely for the availability of experimental data. This raises a question: how well do these methods handle simple oxide systems, let alone a quaternary metal oxide such as CBTO? To test this, we calculated σ for several CBTO surfaces, obtaining E_{bulk} from appropriately transformed unit cells. We found, in all cases, a total unit cell energy of -92.202 eV ± 3 meV on well-converged k-point grids (3 × 3 in the basal plane). Using the linear fit approach, the same k-point grids yielded E_{bulk} values ranging from -92.206 eV to -92.210 eV. In the most deviated cases, using the transformed-bulk value resulted in divergence of σ versus N. However, $\Delta\sigma$

between the two methodologies was calculated at just 0.032 J/m^2. This suggests that the method of Sun and Ceder may be valid beyond elemental systems. We believe that further testing of the Sun and Ceder method is warranted and may lead to a more efficient means of obtaining accurate surface energies for complex oxides. However, for the present study, we decided to proceed with the well-established linear fit approach in obtaining E_{bulk}, as it has been tested more thoroughly on non-elemental systems[245,246] and completely eliminates the divergence problem.

Regarding the computational cost of the linear fit model, we offer this: if one considers the thickness threshold to be a criterion for reliable calculations of surface energies, the aforementioned reasoning for the choice of N provides us with a guiding principle. If a slab is said to be of sufficient thickness, we argue that atomic coordinates adjacent to its "bulk" region will vary minimally while its surface atoms relax. Hence, the threshold can be selected by monitoring lattice distortions in bulk-adjacent layers of a slab. We set the thickness threshold for the linear fit to N such that atomic displacements in the bulk-adjacent layers of the N-layer slab are reasonably negligible during slab relaxation. We found this approach to quickly converge E_{bulk} when slabs with bulk-adjacent layers exhibiting atomic displacements greater than 5 pm were removed from the dataset. Furthermore, surface relaxation diminishes relatively quickly away from the surface, often within 2-3 layers depending on the interplanar separation distance of the surface plane. Hence, we suggest that the initial N-layer slab in the set $\{N\}$ covers at least these many layers, allowed to relax, then used as an initial guess geometry for the slab of $N + 2$ layers to reduce computational resources. The latter process is repeated until bulk-adjacent layers remain unaffected. We present in Figure 6.1 a summarized test case for the (101) surface of CBTO. Surface energies calculated using E_{bulk} terms obtained from the conventional bulk unit cell and the transformed unit cell both diverge with increasing slab thickness. In contrast, the linear fit method predicts consistent surface

energies throughout the range of N. Average atomic displacements in bulk-adjacent layers (plotted on the right y-axis) fall below 5 pm at $N = 9$ and effectively vanish at $N = 11$. We then conclude that $\{N\}$ for the linear fit model limited between 9 and 13 layers is sufficient for obtaining a converged surface energy for the (101) surface at a minimal cost. These guidelines supplement the work of Frankcombe and Løvvik[247], in which the authors suggest a so-called "bottom" fit to the thickest slabs in a dataset as the most reliable means of calculating σ. We provide here a more systematic approach for determining the extrema of the linear fit, avoiding both unreliably thin, and costly thick slabs**.**

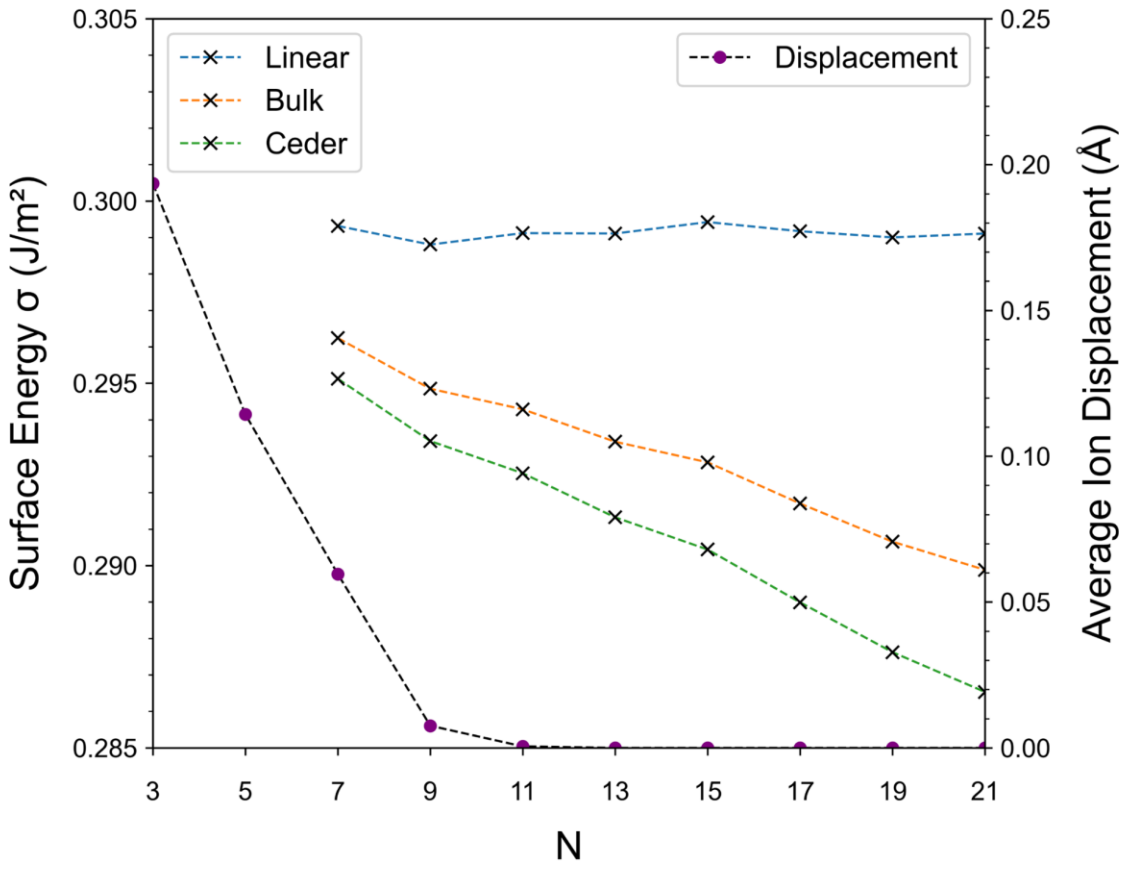

Figure 6.1. Surface energies (left axis) and average ion displacements in bulk-adjacent layers (right axis) – "bulk" being the central layer of the slab – are presented here with respect to the number of layers N in the slab model for the (101) surface of CBTO.

6.3. Results & Discussion

6.3.1. Structural and Electronic Properties of Bulk CBTO

The lowest energy phase for CBTO is shown in Figure 6.2a. Calculated lattice parameters are a = 5.094 Å, b = 6.137 Å, and c = 6.249 Å (α = 109.5°, β = 91.8°, γ = 113.2°). Though experimental lattice parameters are not yet reported, we can compare our results by superimposing our calculated XRD spectra[248] onto the experimental XRD plot. This is shown in Figure 6.2b with (hkl) labels corresponding to stoichiometric (green) and non-stoichiometric (red) CBTO surfaces. The calculated XRD pattern is in sufficient agreement with experimental data to confirm our

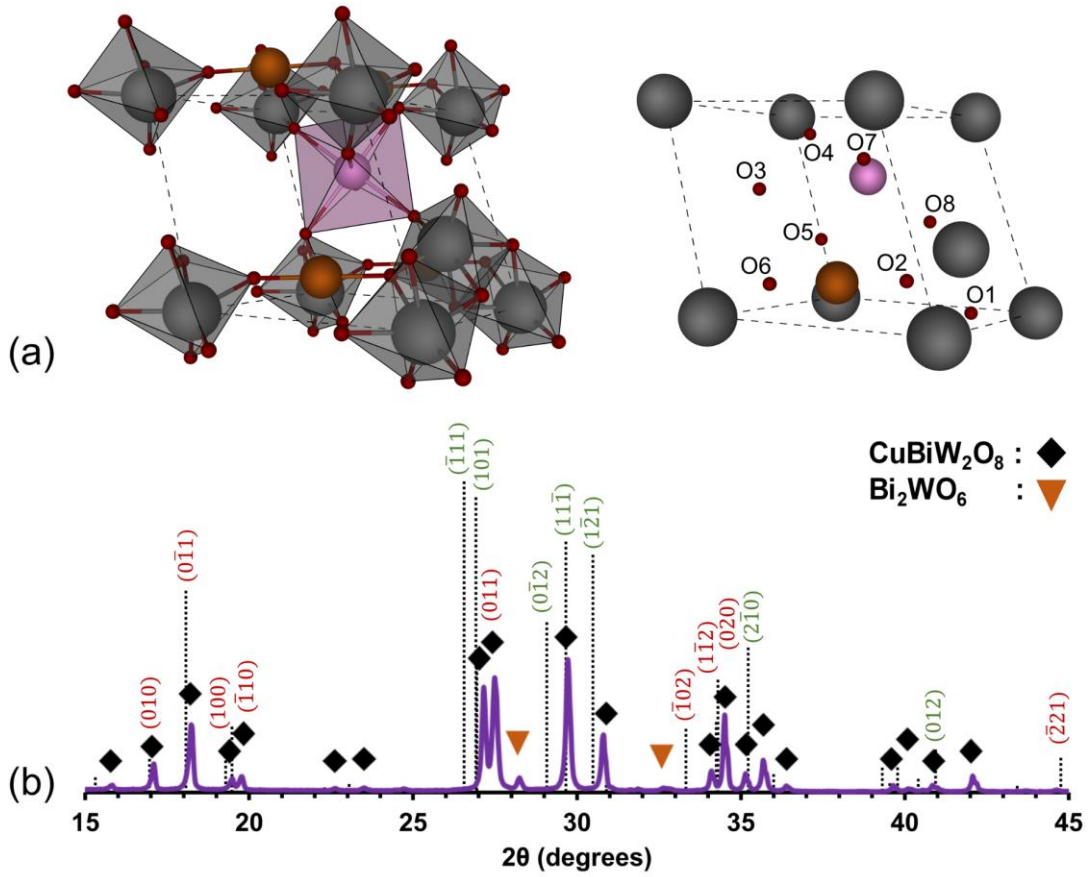

Figure 6.2. (a) CBTO unit cell polyhedral view (left) and labeled O sites (right). Atomic species are represented as follows: Cu (brown, two sites); Bi (pink, single polyhedron); W (dark grey, remaining polyhedra); O (maroon, smallest spheres). (b) Theoretical (dotted black) and experimental (solid purple) CBTO XRD pattern. Persistent Bi_2WO_6 impurity phase peaks are marked on the experimental plot. Reflection plane labels for stoichiometric (green) and non-stoichiometric (red) surfaces are obtained using VESTA.

crystal structure model for CBTO. The overall apparent leftward shift of the calculated data from the experimental XRD pattern is a consequence of the well-known tendency of GGA functionals to overestimate lattice parameters[127]. Differences in relative peak intensity are to be expected due to the pristine bulk nature of our calculation. Bi_2WO_6 impurities (peaks marked by orange triangles in the experimental XRD plot) are not represented in the calculated XRD data. Also, potential mechanical stress rendered during synthesis may result in higher concentration of defects along certain directions affecting structure factors. These defects in the synthesized sample can affect the relative peak intensity.

The highly triclinic crystal structure of CBTO (space group $P\bar{1}$ #2) exhibits inversion symmetry about Cu and Bi sites. Additional inversion symmetry exists about the shared edges of W octahedra. Four O sites are deemed symmetrically unique. We summarize the bonding and charge characteristics of CBTO with respect to these sites in Table 6.1. Bond lengths are in good agreement with previous experimental and computational values[132,249–251]. The larger variation in W-O bond lengths is a result of significant off-center displacement observed in W octahedra (fig. 6.3a). This is a known phenomenon in perovskite-like octahedra[252,253], in which the system reduces its energy by decreasing nearest-cationic-neighbor repulsion while increasing cation-anion orbital hybridization. The calculated 2.840*e* charge on W ions is countered by two O sites with a maximum

Table 6.2. CBTO unit cell bond lengths (Å) and calculated Bader charges (*e*) with respect to the four unique O sites. Symmetric O sites are given in parentheses. Cation Bader charges are as follows: Cu (0.744*e*); Bi (2.065*e*); W (2.840*e*).

	Cu-O	Bi-O	W1-O*	W2-O*	Charge
O1(5)	-	2.386	2.119	1.999	-1.15
O2(6)	1.878	-	1.878	2.274	-1.08
O3(7)	-	2.364	1.808	**	-1.01
O4(8)	-	2.404	**	1.796	-1.00

* Bonds for W1-O1/2 are identical for W2-O5/6

** Identical W-O bond as neighboring W-(O)

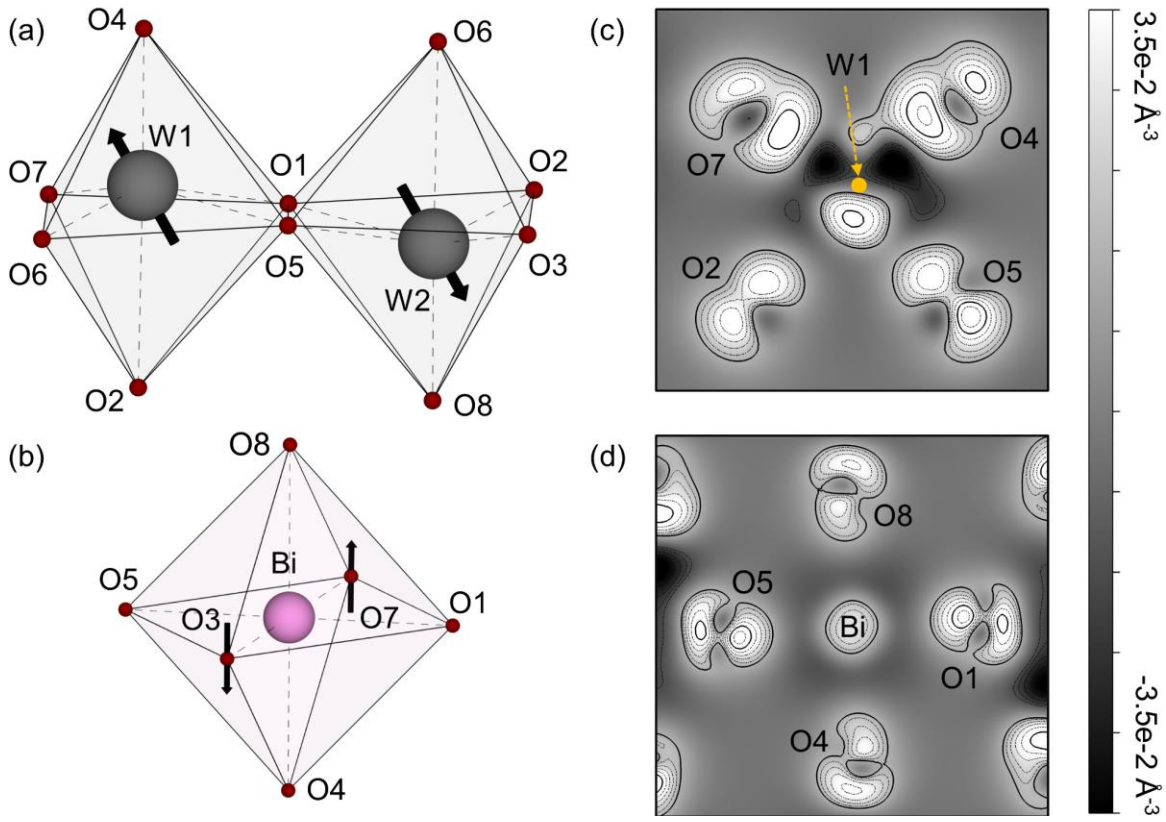

Figure 6.3. (a) W octahedral off-center displacement towards O4(8) – O7(3) edges shown as vectors. (b) Bi cation remains in its octahedral centroid due to its lower electronegativity and the weak stereochemical activity of its 6s lone-pair electrons. In/out-of-plane tilting is shown vectorially for O3(7) sites. (c-d) charge density difference plots show increased W 5d – O 2p hybridization about the O4 – O7 edge, as compared to the symmetric charge distribution about Bi octahedral O sites. The weak stereochemical activity of Bi 6s lone-pair electrons is reflected in a central electron density about the Bi site. In contrast, the W cation (yellow dot) exhibits a tail electron density indicative of sp^3d^2 hybridization.

combined charge of -2.232*e*. The leftover charge repels W ions towards the unshared O4(8) – O7(3) edges to maximize their separation. In doing so, W 5d – O 2p orbital overlap and bond covalency increase along those edges (fig. 6.3c). This is also reflected in the calculated Bader charges for the O sites, with those sites involved in the increased hybridization exhibiting charges further away from the O^{-2} ionic limit. The lack of cation displacement in Bi octahedra (fig. 6.3b) is attributed to the lower electronegativity of Bi (2.02) compared to W (2.36), as well as to the known weak stereochemical activity of its $6s^2$ lone-pair electrons[131]. The latter is observed as a

localized electron density about the Bi site (fig. 6.3d). Hence, W is more likely to pursue covalent bonding with its local anions than Bi.

The effects of increased W 5d – O 2p hybridization can be seen in Figure 6.4, where we present the electronic band structure of CBTO. Here, we compare two scenarios: (i) the fully relaxed CBTO unit cell with W ions in their equilibrium distorted position (fig. 6.4a), and (ii) a hypothetical modification of the same relaxed CBTO unit cell, with W ions manually shifted to the centroid of their respective octahedra (fig. 6.4b). In CBTO, the top of the valence band shows a strong contribution from O 2p, as is common for metal oxides. The conduction band maximum (CBM) is primarily W 5d. Hence, as W shifts away from the centroid and towards the edge of its octahedron, W 5d – O 2p hybridization results in an increase in bonding-antibonding splitting, which widens the band gap by ~0.7 eV. Further hybridization can be seen deep in the valence band, with the coupling and consequent delocalization of W 5d – O 2s orbitals around -18 eV. Overall, the downshifting of O states bounds the system and lowers its total energy. Though Bi remains undisturbed with respect to its octahedral centroid, Bi 6s – O 2p hybridization is affected by the redistribution of charge in response to W displacements. The Bi 6s – O 2p bonding state is slightly downshifted from -10 eV (fig. 6.4b) to about -10.5 eV (fig. 6.4a). Meanwhile, its antibonding counterpart near -2 eV becomes more pronounced (fig. 6.4a, inset). At the CBM, unoccupied Bi 6p states weakly hybridize with W 5d and O 2p states. We recently studied the behavior of lone-pair electrons in $Bi_{2-x}Sb_xWO_6$ and found a strong connection between Bi/Sb lone-pair stereochemical activity and WO_6 octahedral distortions[254]. Local distortions about Bi/Sb sites directly contributed to a bonding-antibonding splitting of W 5d – O 2p orbital energies, consequently upshifting the conduction band edge position. The charge density analysis detailed here for CBTO highlights the significant role of W in shaping the electronic properties of its host materials.

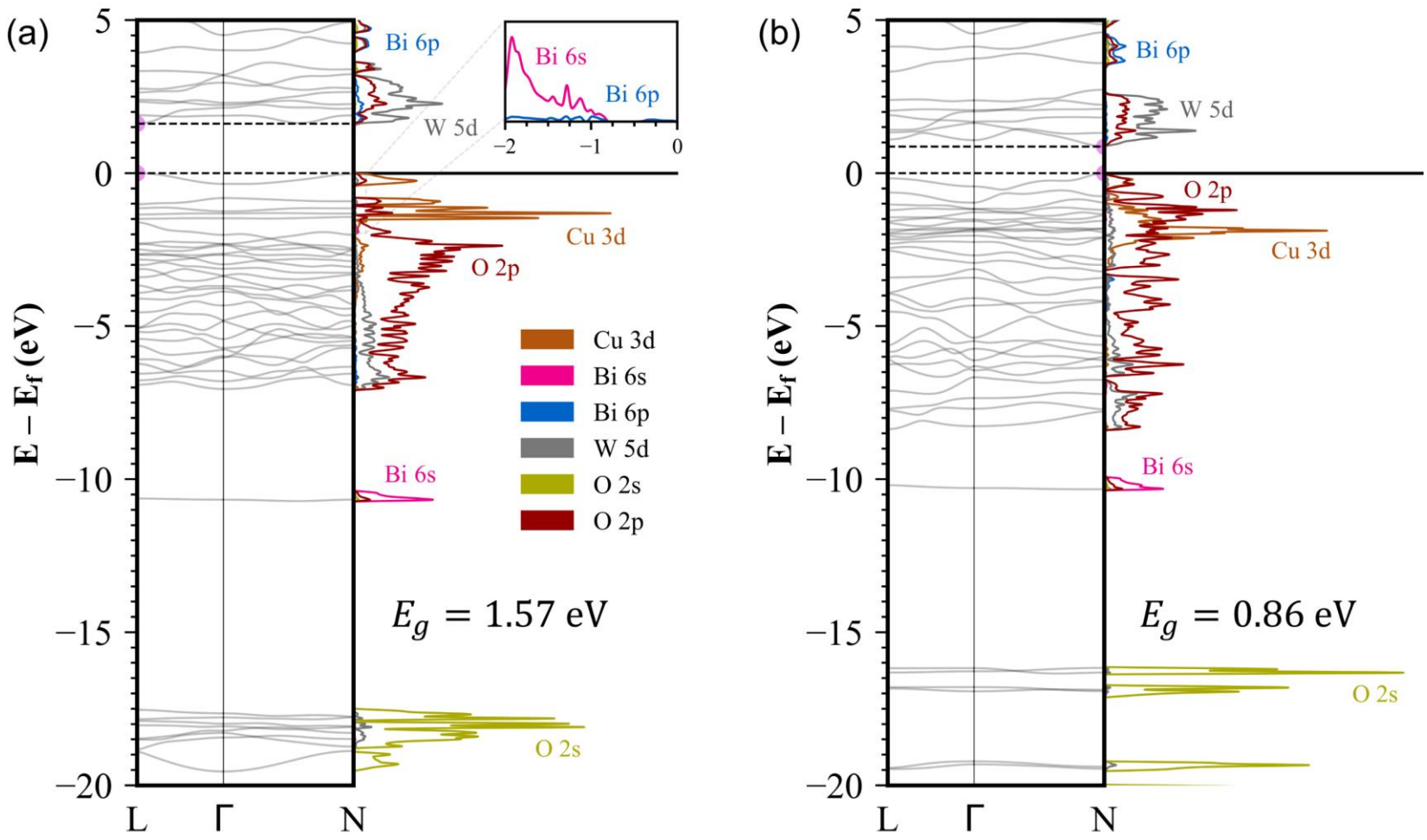

Figure 6.4. DOS plots and band structures for (a) CBTO fully relaxed unit cell and (b) a hypothetical CBTO unit cell with W cations shifted back to their respective octahedral centroids (all other atoms maintained in their relaxed coordinates). The Fermi level corresponds to the highest occupied energy level and is set to 0 eV. W 5d – O 2s/2p orbital coupling arising from increased W-O proximity tends to lower the total energy of the system.

As W displacements effectively pull O 2p down to lower energies, highly localized Cu 3d states become the primary contributor to the VBM. The strongly correlated 3d orbitals are expected to reduce hole mobility. Indeed, we calculate a hole effective mass of 2.24 m_0 for pristine CBTO. In contrast, the W 5d – O 2p hybridized CBM, with additional contribution from Bi 6p, gives an electron effective mass of 0.69 m_0. This suggests good photoexcited electron mobility in CBTO. The band gap is calculated at 1.57 eV. We note, however, that, in the present study, Cu vacancies were not explicitly considered. Our calculations in the experimental paper show that, in the presence of Cu vacancies, the VBM shifts to the acceptor state about the Γ-point, resulting in a Γ-L indirect gap of 1.70 eV. However, as d-d transitions are forbidden, the optical gap was calculated at a slightly higher value of 1.81 eV, representing direct O 2p to W 5d transitions about the Γ-point. This is in good agreement with the experimental measurements [50]. The acceptor state shows increased dispersion, with a calculated effective mass of 1.74 m_0. The CBM remains at the L-point, with an increased electron effective mass of 1.10 m_0. We discuss surface effects on the electronic structure in section 6.3.4.

6.3.2. Low-index Stoichiometric Surfaces

Due to the low-symmetry triclinic space group, a large set of symmetrically unique surfaces is expected. To minimize the dataset, we follow the available XRD data. The highest computational XRD peak is assigned to the $(\bar{1}11)$ plane. All intensities greater than a tenth of this peak and within the range of the experimental XRD data are labeled in Figure 6.2b. In the current study, we focus exclusively on the stoichiometric surfaces of CBTO, avoiding at the present time the added complexity of handling non-stoichiometric surfaces[255–258] that is further exacerbated in quaternary oxides. We do note, however, that relatively strong experimental XRD peaks approximately assigned to the non-stoichiometric $(0\bar{1}1)$ and $(1\bar{1}2)$ surfaces suggest that these surfaces

may play an important role in CBTO morphologies and warrant further investigation. As mentioned in the introduction, their relatively strong peaks may arise from the mixed-phase of CBTO and Bi_2WO_6.

For those stoichiometric surfaces presently considered, calculated surface energies (eqs. 6.2 and 6.3), relaxation energies, and surface bond strengths (S) (eq. 6.1) are shown in Figure 6.5. Exact values and additional surface details are given in Table 6.2. Following the requirements discussed in section 6.2.3, each slab was cleaved in such a way that yields a surface termination

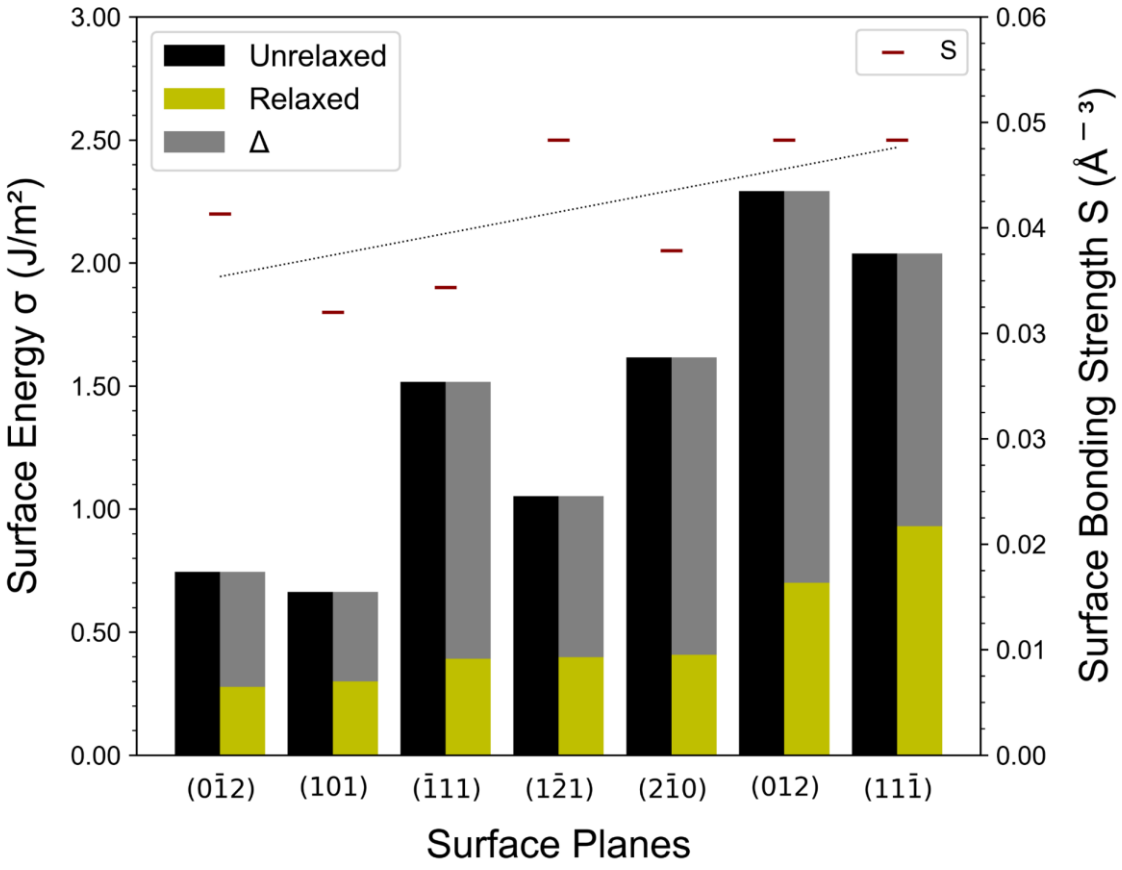

Figure 6.5. Unrelaxed (cleaving) and relaxed surface energies for stoichiometric CBTO surfaces obtained from eqs. 6.2 and 6.3. Also shown is the difference between cleaving and relaxed energies (Δ) defined as the relaxation energy associated with the process of surface charge self-compensation. Surface bond strength estimates (S) calculated using eq. 6.1 are given along with their least-square fit.

Table 6.2. Surface details for selected stoichiometric CBTO surfaces. $M = (N - 1)/2$ represents the vacuum-to-bulk separation in number of layers used in obtaining well-converged energies; d is the interplanar separation distance; A is the surface area; O_T is the set of O sites terminated at the surface; Surface unrelaxed (cleaving) and relaxed energies (σ) are obtained from eqs. 6.2 and 6.3. Δ represents their difference, or relaxation energy; S is the surface bond strength estimated using eq. 6.1.

					σ (J/m2)			
	M	d (Å)	A (Å^2)	O_T	unrel.	rel.	Δ	S (Å^{-3})
$(0\bar{1}2)$	5	3.068	59.935	1^1,2^2,4^b	0.745	0.277	0.469	0.044
(101)	5	3.310	50.232	1^1,3^b	0.663	0.300	0.364	0.036
$(\bar{1}11)$	5	3.354	49.572	1^b,2^1	1.517	0.392	1.125	0.038
$(1\bar{2}1)$	5	2.930	58.118	1^2,2^c,4^b	1.052	0.398	0.654	0.050
$(2\bar{1}0)$	5	2.546	70.529	1^2,2^1,3^b	1.616	0.408	1.208	0.041
(012)	9	2.203	79.080	1^b,1^1,2^1,3^1	2.292	0.700	1.592	0.050
$(11\bar{1})$	6	3.010	56.731	2^2,3^b,4^2	2.038	0.930	1.109	0.050

* Bonds for W1-O1/2 are identical for W2-O5/6
** Identical W-O bond as neighboring W-(O)

which minimizes structural deviations between the two slab surfaces, thus minimizing model-related dipoles. For each slab, the number of surface layers $M = (N - 1)/2$ required for surface energy convergence appears to follow the interplanar separation distance d of the slab. This suggests a relatively constant range for surface electrostatics in CBTO. The top three layers of the five most stable surfaces are shown in Figure 6.6.

From a thermodynamic perspective, the $(0\bar{1}2)$ and (101) surfaces are equally the most stable. This agrees with their relative peak intensities in the experimental XRD data (fig. 6.2b). Their comparable cleaving energies (as defined in section 6.2.3) also suggest a similar surface termination. Terminal O sites (O_T) are given in Table 6.2. The terminated Bi-O bonds in the two surfaces are of different lengths but of like-charges (table 6.1). The $(0\bar{1}2)$ surface terminates an additional W2-O2 bond. However, both the length of this bond – the longest in W octahedra – and the larger $(0\bar{1}2)$ surface area weaken its overall surface bond strength, which explains the near-

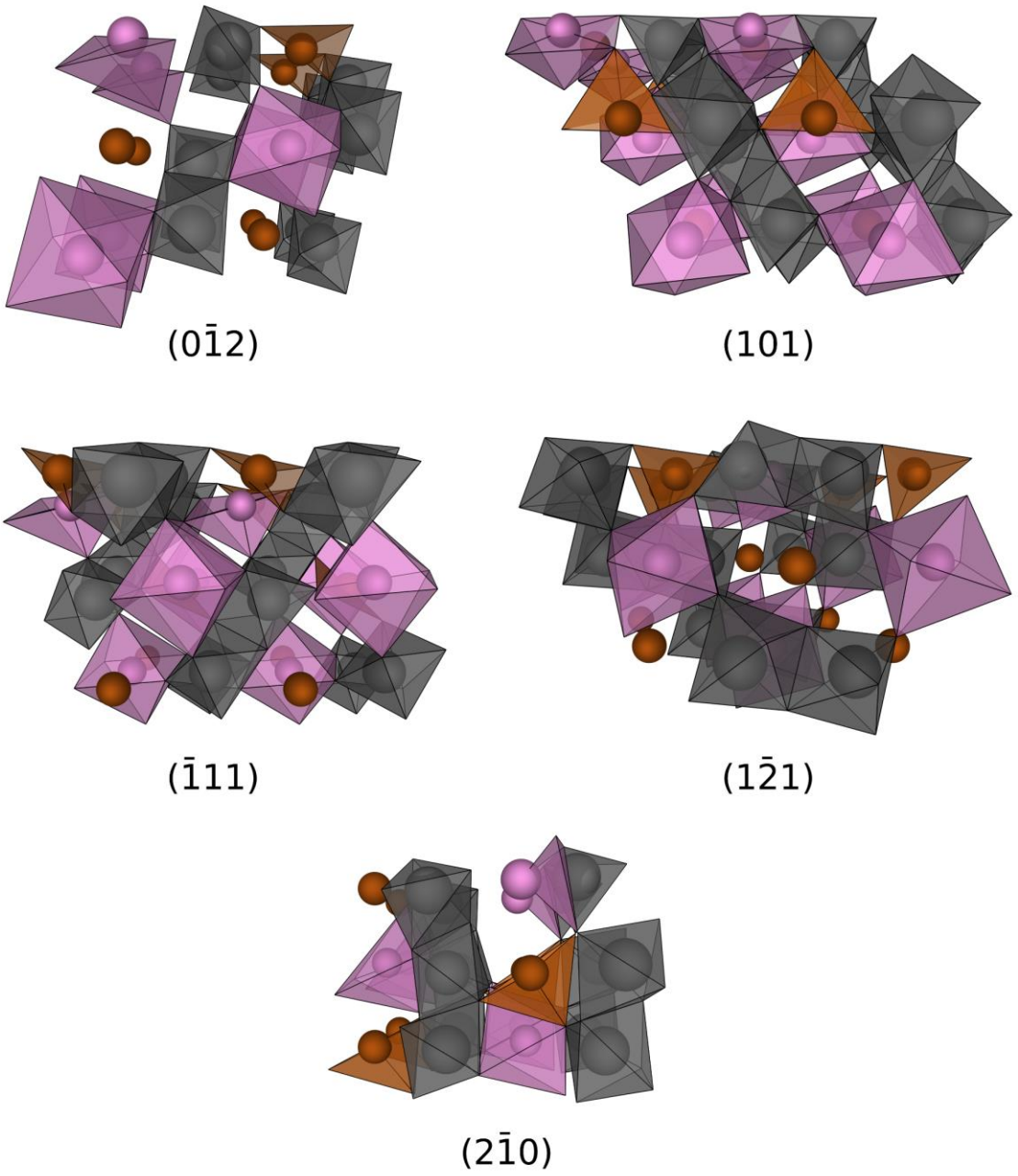

Figure 6.6. Top three slab layers of the five most stable CBTO surfaces. Polyhedra are shown for Cu (brown), Bi (pink), and W (gray), with corners representing O sites. Surface reconstruction is observed about Cu sites, with the formation of an additional Cu-O bond seen across the dataset. Reduced coordination in W polyhedra results in increased W 5d – O 2p hybridization, which tends to stabilize the system. A similar effect is attributed to the newly-formed Cu polyhedra.

identical cleaving energies for the two surfaces. The slightly higher cleaving energy of the $(0\bar{1}2)$ surface is reflected in its S value. The stability of the $(0\bar{1}2)$ and (101) surfaces is attributed to a redistribution of surface O sites leading to surface reconstruction which yields tightly bound W2 tetrahedra (fig. 6.6). As discussed in the previous section, shorter W-O bonds stabilize the system by lowering its total energy through the coupling of W 5d and O 2s/2p states (fig. 6.4).

In contrast, the less stable (012) surface terminates three W-O bonds and one Bi-O bond. Though the four bonds are spread over the largest surface area in the dataset, the relatively higher charge on the terminated O1 and O2 sites likely results in significant perturbations of surface electrostatics, which explains its highest cleaving energy in the dataset. The $(11\bar{1})$ surface breaks one less W-O bond, but its smaller surface area raises the density of dangling bonds, which explains its identical S value and comparable cleaving energy to the (012) surface. Surface relaxation in both the (012) and $(11\bar{1})$ surfaces retains the bulk 6-fold coordination of W octahedra, though with relatively longer bonds (fig. 6.6). This weakens the W 5d – O 2p hybridization resulting in higher surface energies. The $(11\bar{1})$ surface terminates the shortest W2-O4 bond, significantly diminishing the stabilizing effect of W 5d – O 2p hybridization, which explains its highest surface energy.

A study by Zhao et al.[259] of the stoichiometric surfaces of $BiVO_4$ found that the most important factor in determining surface stability is surface dangling bond density. However, even though eq. 6.61 does explicitly account for bond densities, our calculated surface bond strength estimates (S) do not appear to provide a complete picture, instead producing fluctuating S values with increasing surface energy (fig. 6.5). This is likely due to the lack of proper accounting of surface bond chemistry. For example, within its current definition, eq. 6.1 does not differentiate between W-O and Cu-O bonds of similar length, an added layer of complexity in quaternary oxides

such as CBTO. Nevertheless, S does exhibit a positive linear trend with increasing surface energies. This is also true for cleaving energies, which exhibit similar fluctuations. As mentioned in section 6.2.3, relaxed surface energies are sums of cleaving energies and relaxation energies. Therefore, the fluctuations in cleaving energies may be explained through a closer examination of surface relaxation.

In Figure 6.7, we plot site displacements and partial charges as functions of slab height for the five most stable surfaces. Site displacements represent a redistribution of surface atoms along electric field lines as part of the surface relaxation process self-compensating unsaturated charges arising from surface cleaving. Hence, the fluctuation of cleaving energy with respect to surface energy may be explained by the different degrees of freedom and unique electrostatics at each surface reflected in its site displacement magnitudes. The two most stable surfaces exhibit the least overall displacement corresponding to their low relaxation energies. In contrast, the remaining surfaces exhibit pronounced O displacements reflecting their more significant surface relaxation. The $(\bar{1}11)$ and $(2\bar{1}0)$ surfaces also exhibit W and Bi displacements explaining their higher relaxation energy. Though these displacements are lower in the $(1\bar{2}1)$ surface, it exhibits twice as large of a displacement in its Cu ions, resulting in an intermediate relaxation energy.

Cu displacements can be seen across the dataset, in all cases leading to the formation of a third Cu-O bond with its nearest O4 site (fig. 6.6). The two existing Cu-O bonds elongate slightly to accommodate the newly-formed Cu-O4 bond. The average Cu-O bond length at the CBTO surface is about 2 Å. This type of surface reconstruction occurs only about Cu sites, as the mostly ionic CBTO metal-oxide bonding network hinders large displacements for W and Bi ions from their bulk octahedral geometries. In contrast, the linear O-Cu-O bonding geometry affords Cu some local diffusive freedom. Moreover, the proclivity of Cu^{1+} ions to seek out their more natural

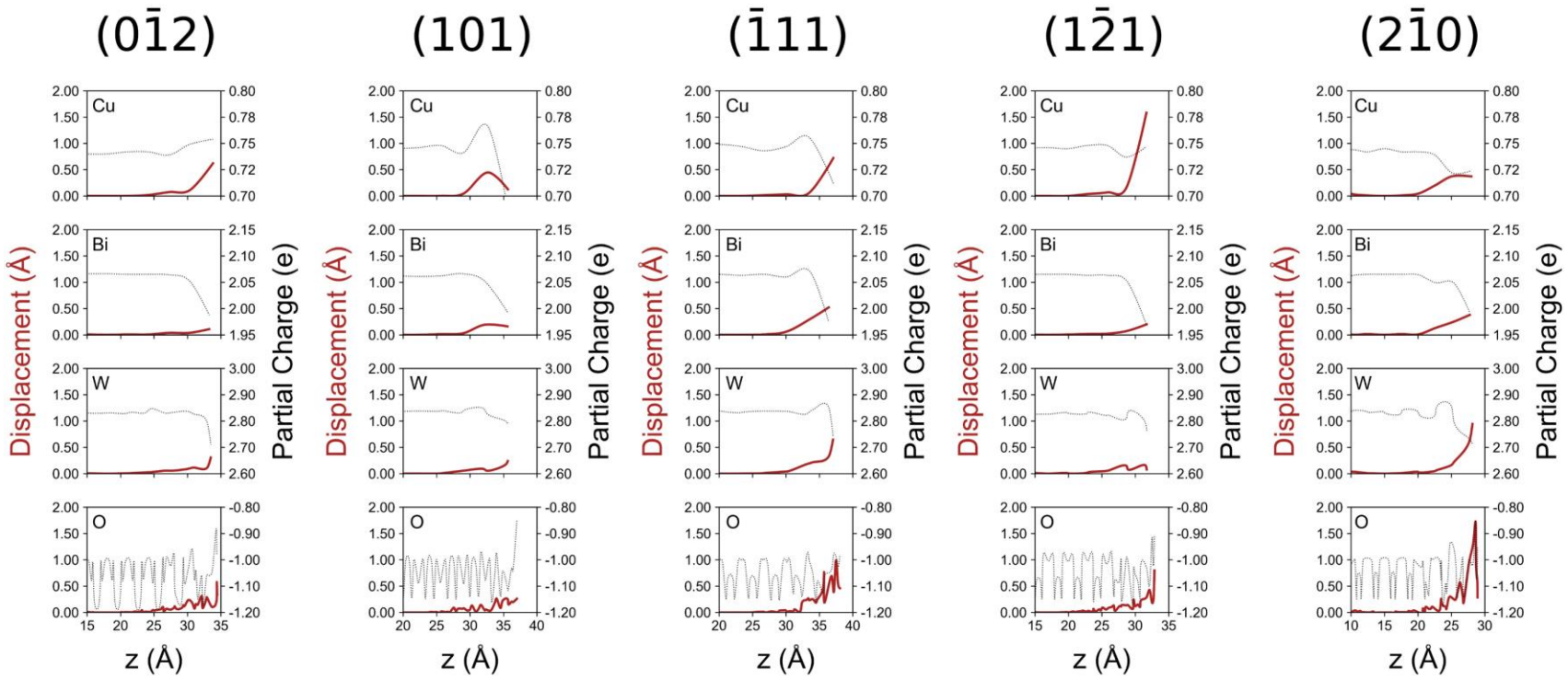

Figure 6.7. Site displacements (solid red line) and calculated Bader partial charges (dotted line) as functions of slab height z.

Cu^{2+} oxidation state further drives the motion of Cu ions. Interestingly, 3-fold coordinated Cu ions exhibit their highest partial charge in the most stable $(0\bar{1}2)$ and (101) surfaces. With Cu 3d – O 2p hybridization occurring directly at the VBM, we determine that the energy-lowering effect observed for W octahedra in the bulk is also taking place along the newly formed Cu-O bonds. We note, however, that the self-compensation of unsaturated surface charge via surface relaxation is a limited process, with larger cleaving energies resulting in unstable surfaces even after full relaxation. For example, the (012) surface, which exhibits the largest relaxation energy, remains one of the least stable CBTO surfaces due to its highest cleaving energy. This explains the overall positive linear trend in both cleaving energy and S with diminishing surface stability despite their fluctuations.

6.3.3. Crystal Shape

The crystal shape of a material can be predicted from fully relaxed surface energies via Wulff construction[260,261]. In this approach, it is understood that lower energy surfaces should constitute larger portions of the resultant crystal surface area. This follows from the conclusions of Gibbs regarding the minimum total surface energy of an equilibrium crystal[262]. The construction proceeds as follows: (i) the lowest energy surface is normalized to unity; (ii) all other (hkl) surfaces of interest are rescaled by

$$\mathrm{m_{hkl}} = \left(\frac{\sigma_{\mathrm{hkl}}}{\sigma_0}\right)\left(\frac{\mathrm{d_{hkl}}}{\mathrm{d_0}}\right) \tag{6.4}$$

where σ_{hkl} (σ_0) and d_{hkl} (d_0) are the surface energy and interplanar separation distance of the (hkl) surfaces (lowest energy surface), respectively; (iii) m_{hkl}, the fractional normal distance from the origin of the crystal to an (hkl) surface, is then used in available visualization software to define the (hkl) planes (and their symmetrically equivalent planes) forming the crystal shape. In

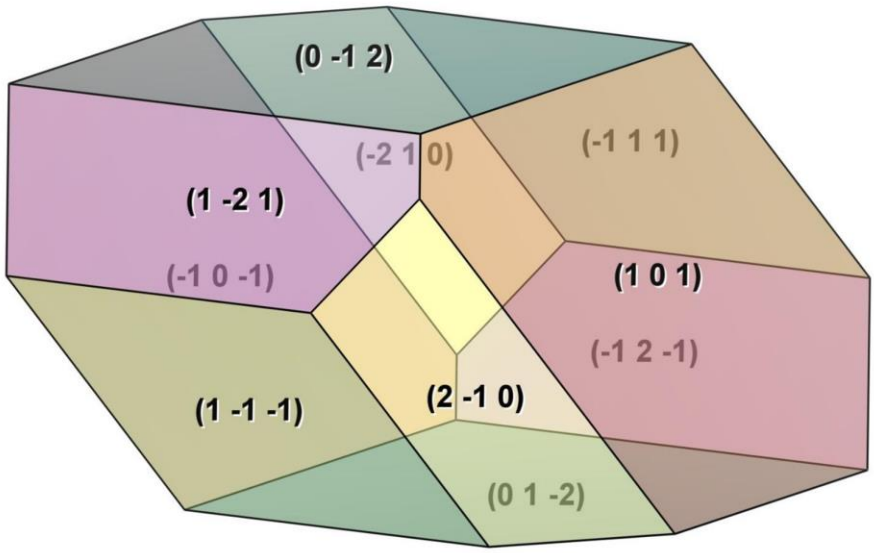

Figure 6.8. CBTO equilibrium (0 K) crystal shape obtained via Wulff construction. Surface contributions are: $(\mathbf{0\bar{1}2})$ 31%; $(\mathbf{101})$ 32%; $(\mathbf{\bar{1}11})$ 15%; $(\mathbf{1\bar{2}1})$ 14%; $(\mathbf{2\bar{1}0})$ 8%. The two most stable surfaces constitute nearly two-thirds of the CBTO surface area. Hence, electronic structure variations due to surface effects are attributed primarily to the structure of the $(\mathbf{0\bar{2}1})$ and $(\mathbf{101})$ surfaces.

the present work, this was done using the VESTA visualization software[88]. The resultant crystal shape shown in Figure 6.8 corresponds well to calculated surface energies, with surface area contributions of 31% for $(0\bar{1}2)$, 32% for (101), 15% for $(\bar{1}11)$, 14% for $(1\bar{2}1)$, and 8% for $(2\bar{1}0)$. The (101) surface has a slightly larger surface area than the lowest energy $(0\bar{1}2)$ surface – 47.584 $Å^2$ compared to 47.155 $Å^2$ – due to its higher (hkl) index, resulting in a steeper surface[261].

6.3.4. Surface Electronic Structure

Lastly, we investigate the effects of surface relaxation on the electronic structure at the CBTO surface. In Figure 6.9, we present orbital-projected density-of-states (PDOS) analyses separately localized on the central three layers (Bulk) and remaining outer layers (Surface) of the slab models of the five lowest energy CBTO surfaces. PDOS plots are accompanied by their respective band structures calculated along high symmetry paths in Brillouin zone planes parallel to the respective surfaces.

The overall distribution of states is retained at the surface, though a significant localization can be observed at the VBM with a large contribution from Cu 3d states. The localization appears to shift slightly away from the VBM following increasing surface energies. This again highlights the primary role of Cu in surface relaxation and the resulting surface energies. Band structures also show a narrowing of the fundamental gap with respect to the bulk (fig. 6.4) across all surfaces, which is to be expected. An exception is observed for the $(2\bar{1}0)$ surface, which exhibits a slightly wider band gap of 1.61 eV. Additionally, all but the (101) surface exhibit a direct-to-indirect band gap transition. The (101) surface exhibits a direct gap of 1.49 eV at the L-point. Interestingly, the (101) surface – the most exposed (fig. 6.8) – also exhibits larger valence band dispersion, suggesting a reduced hole effective mass and improved mobility. In contrast, the lowest energy $(0\bar{1}2)$ surface exhibits a rather flat band closer to the VBM due to the increased surface Cu 3d localization. As mentioned in the introduction, CBTO mobility is attributed to hole carriers (p-type) and is higher than comparable oxides[33].

6.4. Conclusion

In this paper, we studied the surface properties of CBTO, a newly predicted, recently synthesized, novel quaternary metal oxide identified as a potential high-efficiency solar energy absorber. First, we performed a DFT analysis of the CBTO bulk unit cell to facilitate surface modeling. From the calculated lattice parameters, we developed a labeled theoretical XRD pattern for CBTO in its standard crystallographic orientation. This was found to be in good agreement with the experimental XRD data. We then studied the crystal and electronic structures of bulk CBTO and found that a W 5d – O 2s/2p increased orbital overlap due to W off-center displacements within its octahedra plays a key role in stabilizing the system and widening the band gap to 1.57 eV.

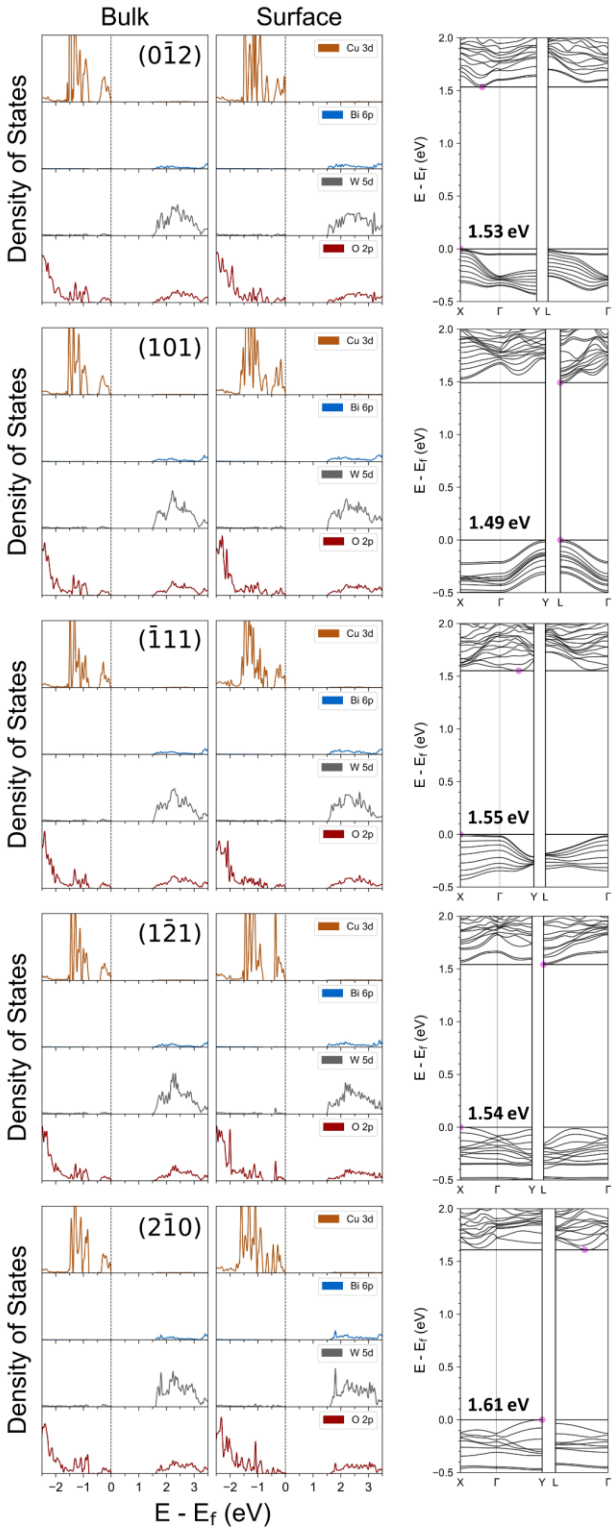

Figure 6.9. Electronic structure of the five most stable stoichiometric CBTO surfaces. Left panel: PDOS plots split into "bulk" sites defining the central three layers and "surface" sites covering the remaining outer layers of the slab; right panel: band structures are calculated in the surface-parallel Brillouin zone plane ($B_1 \times B_2$). Band gap energies are also given.

From the theoretical XRD plot, several low-index stoichiometric surfaces were identified for further investigations. To determine the relative stability of these surfaces, we calculated their bond strength, cleaving energy, and relaxed surface energy. We first compared several methodologies for computing surface energy and found that the method of Sun and Ceder, though still resulting in surface energy divergence with increasing number of layers, yields surface energies for CBTO with only minor deviations from those produced by the more established linear fit method. We then recommend further testing of the Sun and Ceder methodology on additional complex oxides to verify its potential as an efficient means of obtaining reliable surface energies. In the present study of CBTO, we proceeded with the linear fit method. To address its associated computational cost, we developed a physical criterion to establish the lower and upper bounds of slab thickness used in the linear fit model, allowing for the efficient calculation of well-converged surface energies while eliminating the need for unnecessary expensive computations. The general guideline delineated here for calculating surface energies may be applied to any system, including complex, multi-component compounds.

Calculated surface energies were used to predict the CBTO equilibrium crystal shape via Wulff construction. The $(0\bar{2}1)$ and (101) surfaces were found to be equally the most stable, each constituting about 30% of the crystal shape. The surface stability trend was explained from the perspective of surface site displacements representative of surface relaxation and surface reconstruction driven by electrostatics and charge self-compensation at the surface. As was seen in the bulk, the relaxation process led to displacements in W octahedra, which were again found to play a key role in determining surface stability via the energy-lowering mechanism of W-O hybridization. In addition, large Cu displacements were observed at the surface due to their proclivity of seeking out a Cu^{2+} oxidation state. These displacements led to surface reconstruction about Cu

sites via the formation of a third Cu-O bond. With a significant contribution at the VBM, it was concluded that hybridization along newly formed Cu-O bonds was further contributing to the overall stability of the surfaces. Due to the mostly ionic metal-oxide bonding network and W and Bi octahedral geometries, further surface reconstruction in CBTO is not expected.

Acknowledgements

We acknowledge useful discussions with Prof. Pratap Rao and Dr. Pranab Sarker. All calculations were performed on Texas Advanced Computing Center (TACC) servers. This work was supported by the National Science Foundations, award no DMR-1609811.

Chapter 7

Conclusions

The aim of the present dissertation was to explore the ns^2-md^0 metal oxide class and assess its viability in producing materials of favorable properties for solar energy conversion applications, with emphasis on electronic properties pertaining to the photoelectrochemical (PEC) process. The challenge of obtaining p-type metal oxides for photoanode/photocathode PEC cell design was highlighted as the problem of interest. The depth of the O 2p energy level was identified as the leading cause of spontaneous "acceptor-killer" defect formation preventing p-type doping. In addition, the localization of O 2p orbitals in metal oxide was shown to lead to poor hole mobility and high recombination rates. Various alloying schemes were investigated under the general hypothesis that the O 2p dominated valence band maxima (VBM) in metal oxides may be upshifted via orbital hybridization with d^{10} and/or ns^2 orbitals. Alternatively, p-orbitals of higher principal quantum number may be introduced via anion doping to form higher energy VBM states. Material properties were investigated via first principles calculations carried out under the density functional theory framework, as described in chapter 2.

In chapter 3, the ns^2-md^0 class was explored from the perspective of crystal structure and d-orbital effects. The stibiotantalite mineral, Sb(Ta,Nb)O4, was designed in three common ns^2-md^0 crystal phases – tetragonal, orthorhombic, and monoclinic – and its band gap, band dispersion, and band edge position properties examined. Furthermore, in each crystal phase, the d-orbital character was varied between Ta (5d) and Nb (4d) to study its effects on the crystal and electronic structure. The introduction of Nb 4d states gradually lowered the conduction band minima (CBM) of all three phases by up to 0.5 eV. Moreover, in the tetragonal and monoclinic phases, Nb 4d states also yielded greater band dispersion. An opposite trend was found in the orthorhombic

phase. Overall band dispersion in stibiotantalite was found to be lower than ns^2-md^0 system of m = 3, such as $BiVO_4$, due to reduced orbital localization. The presence of Nb 4d electrons had no significant effect on the shape and position of the valence band. As such, it was concluded that the ns^2-md^0 stibiotantalite system affords a degree of freedom in CBM engineering. Regarding the position of the VBM, all three crystal phases yielded an upshift of the VBM by at least 1 eV through the formation of occupied antibonding orbitals. The greatest shift was seen in the tetragonal phase, followed by the monoclinic phase, and lastly by the orthorhombic phase. The higher VBM states in tetragonal phases narrowed the band gap with respect to orthorhombic phases by about 0.6 eV, independent of the d-orbital character. Interestingly, due to the varying degree of ns2 – O 2p orbital hybridization, the opposite trend was found in crystal stability, with all orthorhombic phases exhibiting the lowest cohesive energy. These findings highlight the complexities involved in designing efficient metal oxides for PEC applications.

In chapter 4, the behavior of lone-pair electrons in the 5s/6s mixed lone-pair environment of Sb-alloyed Bi_2WO_6, or $BiSbWO_6$, was investigated. As Sb $5s^2$ orbitals are higher in energy, their hybridization with O 2p was expected to upshift the VBM with respect to the Bi 6s – O 2p hybridized antibonding state. Several configurations of $BiSbWO_6$ were studied to examine the effects of lone-pair projections on the crystal and electronic structure. It was found that, thermodynamically, all $BiSbWO_6$ lie within a narrow stability range. As such, configurational entropy was determined to further stabilize the alloy by 8 meV. It is thus assumed that when synthesized, $BiSbWO_6$ would exhibit an ensemble-like mixture of electronic properties. The lowest energy configuration was examined further for its lone-pair influenced electronic properties. As expected, greater hybridization was observed between Sb 5s and O 2p orbitals yielding a VBM state 0.5 eV higher – with a hole effective mass 0.4 m_0 lower – than its Bi 6s counterpart. Higher VBM states

were observed in general for $BiSbWO_6$ with respect to Bi_2WO_6, resulting in narrower band gaps. More interestingly, CBM upshifts were also observed. These were determined to be the cause of W 5d – O 2p increased hybridization as a consequence of the reorientation of Sb $5s^2$ lone-pair projections, which reduced octahedral tilting in WO_6 perovskite-like layers. Overall, these observed band edge upshifts are favorable for the PEC application and suggest a potential route for stoichiometric water-splitting.

In chapter 5, the viability of anion doping/alloying was examined via S-in-O substitutions in $CuBiW_2O_8$ (CBTO). The introduction of sulfur to the oxygen matrix was expected to upshift the VBM and improve hole mobilities due to its higher, more delocalized p-orbital and proximity to Cu 3d levels. However, it was found that at lower concentrations, though the band gap did decrease by about 0.1 eV, effective masses at both band edges increased substantially. This is detrimental to efficient carrier transport. Interestingly, at a S concentration of 50%, S 3p states overtook Cu 3d as the primary contribution at the VBM, which resulted in reduced carrier effective masses with respect to the pristine cell. It is worth noting, however, that at this concentration, the band gap narrowed below 1 eV, which may be detrimental to the PEC application. Additionally, high S concentrations may destabilize the system. Nevertheless, these results highlight the band engineering potential of anion substitution schemes.

In chapter 6, the stoichiometric surfaces of CBTO were studied. Due to the unique complexities of the quaternary oxide, the methodology involved behind obtaining accurate surface energies was discussed and a guideline for future surface energy calculations was proposed. The CBTO unit cell was first discussed from the perspective of polyhedral distortion and orbital hybridization. A W polyhedral off-center distortion was suggested as an energy lowering path taken by the CBTO triclinic system, which in turn opens the band gap due to increased W 5d – O 2p

orbital overlap. From the CBTO unit cell, a theoretical XRD pattern was developed within the standard crystallographic orientation. Agreement between theoretical and experimental XRD patterns confirmed the predicted triclinic unit cell for CBTO. Using the proposed methodology, surface energies were obtained, and the equilibrium crystal shape was predicted. The $(0\bar{1}2)$ and (101) surfaces were found to be most stable. These preliminary results serve as the first set of data needed in determining the effects of experimentally observed surface impurities on the electronic properties of CBTO.

Chapter 8

Future Directions

The results obtained in this dissertation highlight the flexibility and viability of ns^2-md^0 materials for use in solar energy applications. The various alloying schemes explored were found suitable in addressing the inherent shortcomings of metal oxides. As such, the following avenues of further research are of particular interest.

The stibiotantalite system showed flexibility in its electronic structure and properties across the three studied crystal phases. Though the more favorable properties for solar energy applications were observed in the tetragonal and monoclinic symmetries, these were not as energetically stable as the orthorhombic phase. The higher energy of the tetragonal and monoclinic phases does not, however, preclude their formation, as cohesive energies remain negative. Hence, one may explore means in which these metastable phases may be attained. The application of pressure during synthesis may shift the relative stability trend in favor of the metastable phases. Hence, further computational studies should explore the effects of applied pressure on the electronic properties of the stibiotantalite system.

The band edge upshifts observed in $BiSbWO_6$ with respect to the russellite mineral are favorable for PEC applications. Additional calculations are needed to determine the thermodynamic conditions for synthesizing a single phase of the alloy, free of secondary phase impurities. Furthermore, an interface may be constructed of the pristine and alloyed materials and studied to determine their band offset and potential for heterojunction design to improve charge transport. Also, the effects of lone pair electrons on band edges in mixed lone-pair systems should be explored in more systems. The stibiotantalite mineral shows strong lone-pair signatures and should be investigated further from this perspective.

As for CBTO, with surface energies in hand, the CBTO-Bi_2WO_6 interface may be constructed and studied to better understand the effects of Bi_2WO_6 impurities on the surface of CBTO. Additionally, the general results given in the present dissertation regarding band edge engineering in ns^2-md^0 materials may be applied to CBTO to manipulate its properties further towards optimal solar energy conversion efficiency. Similar quaternary oxides may be constructed following the overall findings discussed here.

Appendix A

Stability of Si Fullerene Structures

The following manuscript regards the stability of Si variants of carbon fullerenes. The primary contribution of this paper is a theoretical method for computing and comparing the stability of unpassivated and H-passivated fullerene cages with respect to their bonding network. We show that at a sufficiently large cage radius, the surface curvature flattens and allows for the formation of stabilizing double bonds. At such cases, passivation is no longer energetically favorable.

The author acknowledges the contributions of the late Dr. Cedric Mayfield. This work would not be possible without his insight and guidance. He is greatly missed.

WEAKENING OF Si-Si BONDING IN EXOHYDROGENATED Si_{60} NANOCLUSTERS

Edan Bainglass
Cedric L. Mayfield
Muhammad N. Huda

Bainglass, E., Mayfield, C. L. & Huda, M. N. Weakening of Si-Si bonding in exohydrogenated Si60 nanoclusters. *Chem. Phys. Lett.* **684**, 60–66 (2017).

© 2017 Published by Elsevier B.V.

Weakening of Si-Si Bonding in Exohydrogenated Si_{60} Nanoclusters

Edan Bainglass, Cedric L. Mayfield, and Muhammad N. Huda
Department of Physics, The University of Texas at Arlington, Arlington, TX 76019, USA

Abstract

We performed density functional theory (DFT) analyses of several hollow cage-like Si_{60} nanoclusters and found a favoring of exohydrogenation in terms of reduced binding energies in all the structures except the Si_{60} fullerene. Further investigation into the effects of exohydrogenation on the Si-Si bonding network revealed a level of weakening in Si-Si bonds. A correlation was established between the magnitude of this weakening and the success of exohydrogenation in stabilizing the nanocluster. In addition, we found a slightly bent chain of individual Si_{20} units to exhibit the lowest binding energy among the present group of Si_{60} clusters studied here.

A.1. Introduction

It is well known that bulk silicon takes on a diamond cubic phase. However, at smaller cluster sizes, at which surface states begin to affect stability[263], different geometries become possible. Much work has been done in determining the behavior and stability of Si clusters[264–271]. Our previous work on Si_n clusters (n=75, 150, 300) in both the diamond cubic and Wurtzite phases found the Wurtzite phase to be more stable at these sizes[272]. In the current study, we extended the investigation to n = 60 in order to include the C_{60} fullerene geometry and its derivatives. The unique I_h symmetry of C_{60} has been heavily studied in the past several decades[271,273,282–287,274–281] and has been determined to be unstable for Si_{60} under finite temperature, distorting down to lower symmetries[283,285]. These lower-symmetry, core-shell geometries have been investigated in recent years, and the lowest-energy configuration for Si_{60} has been determined[280,288]. Our interest was to further investigate the mechanics behind the instability of Si hollow cages.

In general, Si cage-like clusters are not expected to be stable at higher symmetry and require a stabilizing component. In endohedral cages[274,278,295,280,281,289–294], an internal support structure is added. The above mentioned lowest energy Si_{60} cluster belongs to this group. An alternative geometry, exohedral cages[276,277,282,286,296], involves the termination of surface states via various species. In particular interest to us was the stabilization properties of exohydrogenation. Due to a strong interaction between Si and H, hydrogen passivation is postulated to be a favorable process in Si clusters and is a viable stabilizing agent[278]. The previous work on Si_n clusters found both the Diamond Cubic and Wurtzite phases to be more stable under exohydrogenation[272]. Preliminary results found passivation favorable in all Si_{60} clusters excluding the Si_{60} fullerene geometry. C_{60} is well known to be extremely stable. Its electronic structure exhibits a mix of sp^2-sp^3 type bonding, with a higher ratio of sp^2 bonding, which plays a role in its stability. Though double bonds are generally not expected in third row elements or greater, rendering a pure Si cage structure presumably unstable, we have found in our study the existence of such bonds in the pristine Si_{60} fullerene geometry. This result may in part explain why the Si_{60} fullerene favors its pristine, unpassivated state.

Noting that unlike its derivatives, in which there exists some level of fully coordinated Si-Si bonding, the fullerene geometry is comprised entirely of surface atoms. This motivated a study of the Si-Si bonding network of the Si_{60} clusters. We found that upon surface passivation, some loss of binding strength occurred in Si-Si bonds. The highest magnitude of this effect was found in the S_{60} fullerene geometry. Further investigation into the electronic structures of the Si_{60} clusters revealed that geometries containing some level of fully-coordinated Si-Si bonding were able to balance the loss of Si-Si bonding strength with the stability gain from passivation of the surface states by concentrating electronic states around the fully-coordinated bonds, consequently favoring

their passivated states. This finding suggested a connection between the presence of such bonding and the final stability of the passivated cluster. We asked the following questions: (i) is the higher stability in exohydrogenated nanoclusters mainly due to the presence of strong Si-H bonds? (ii) How is the core Si-Si bonding strength affected by the presence of hydrogen in the outer layer of the clusters?

In this paper, we present three categories of Si_{60} clusters: (i) bulk-like networks, (ii) C_{60}-like fullerene, and (iii) small Si_n fullerene unit chains (n = 20, 30) – both pristine and passivated with hydrogen. We show that at the 60-atoms size structures based on smaller Si fullerene units are energetically more favorable, and that passivation further stabilizes these geometries. The lowest energies were found in Si_{20}-unit chains, with a slightly bent chain exhibiting the lowest ground state. In the following sections, we discuss our findings on the stability and electronic properties of these structures, as well as our full treatment of the anomalous Si_{60} fullerene case.

A.2. Results & Discussion

A.2.1. Structural Analysis

The Si_{60} geometries investigated in the current study are shown in Figure A.1. Binding energies, average bond lengths, and band gaps are given in Table A.2. The pristine clusters suffered significant distortion upon relaxation. The average bond length for the Si_{60} series was 2.423 Å.

Table A.1. Comparison of LANL2DZ ECP[a] basis set to the all-electron 6-311G basis set

geometry	basis set	binding energy (eV/atom)[b]	average bond length (Å)[c]
Si_{60} fullerene	LANL2DZ	-3.173	2.266
	6-311G	-2.932	2.399
$Si_{60}H_{60}$ fullerene	LANL2DZ	-3.100	2.366 (1.491)
	6-311G	-2.905	2.408 (1.506)

[a] Effective Core Potential
[b] Binding energies were calculated for the singlet state only
[c] Average Bond lengths; Si-H bonds in parentheses

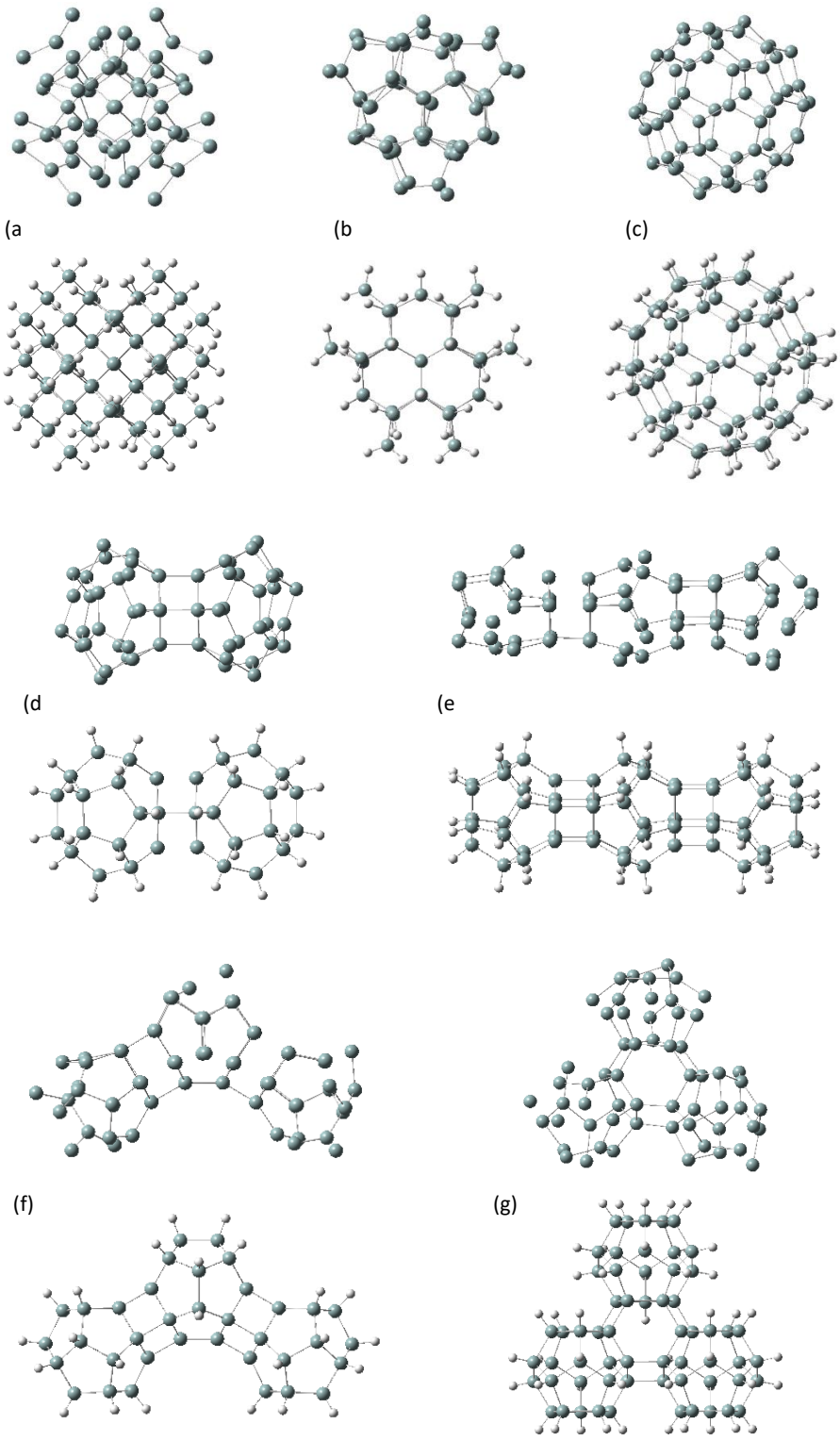

Figure A.1. Pristine (top) and passivated (bottom) Si_{60} nanoclusters optimized under B3LYP/6-311g. (a) Diamond cubic, (b) Wurtzite, (c) Si_{60} fullerene, (d) $(Si_{30})_2$ chain, (e) $(Si_{20})_3$ chain, (f) $(Si_{20})_3$ bent chain, and (g) $(Si_{20})_3$ triangle

Passivation reduced average bond lengths in the clusters except the Si_{60} fullerene and the $(Si_{30})_2$ chain, in which bond lengths slightly increased. The passivated average bond length was 2.411 Å. In addition, passivating the surface states yielded highly symmetric relaxed structures, as was expected (fig. A.1). A correlation was evident between the number of H-atoms used in the passivation of each of the clusters and the level of distortion in their pristine counterpart. Clusters requiring a greater number of H-atoms for passivation exhibited more substantial distortion. This is a manifestation of the surface state energy contribution and the mechanics of passivation. We note that the distortion in the Si_{60} fullerene, however, was not as severe as is to be expected considering its large surface area. It was interesting to instead find the pristine fullerene geometry only 0.072 eV/atom behind the most stable passivated bent chain at -2.932 eV/atom, the highest among the pristine clusters, and equal to the passivated diamond phase. Passivation of the fullerene geometry raised the binding energy by 0.027 eV/atom, as compared to 0.073 eV/atom when tested under LANL2DZ (table A.2). This further shows the inherent stability of the fullerene geometry. It may be partially explained by the particular mode of distortion suffered by the fullerene geometry. We found that upon relaxation of the pristine fullerene, the surface Si atoms pushed outward to reach an average tetrahedral angle of 120°, with some as low as 110°. These values are roughly 1% from the ideal Silane gas angle of 109.5°. The ability of the surface Si atoms to reach these angles was more pronounced in the Si_{60} fullerene than the other cage-like clusters, most likely due to its larger surface area.

The geometries based on Si_n units (n = 20, 30) were modeled after their carbon counterpart[297]. We chose these two small fullerene units for two reasons: (i) a significant amount of theoretical calculations[274,277,285,293] and some experimental efforts[290,298] have been conducted on the electronic properties and stability of these individual small fullerene derivatives, and (ii) they

Table A.2. Binding energies, average bond lengths, and band gaps for Si_{60} nanoclusters

	binding energy (eV/atom)			average bond length (Å)[a]		band gap (eV)[b]		
geometry	LANL2DZ	6-311G	Δ[c]	Si-Si	Si-H	HOMO	LUMO	Δ[d]
Si_{60} DC	-3.061	-2.899	0.033	2.478	-	-5.123	-4.379	0.744
$Si_{60}H_{64}$ DC	-3.132	-2.932		2.404	1.501	-6.464	-1.826	4.638
Si_{60} W	-3.107	-2.922	0.025	2.412	-	-5.241	-4.371	0.870
$Si_{60}H_{60}$ W	-3.149	-2.947		2.410	1.501	-6.296	-2.156	4.141
Si_{60} fullerene	-3.173	-2.932	-0.027	2.399	-	-5.550	-4.169	1.381
$Si_{60}H_{60}$ fullerene	-3.100	-2.905		2.408	1.506	-7.099	-2.219	4.879
$(Si_{30})_2$ chain	-3.084	-2.884	0.091	2.395	-	-5.455	-4.446	1.009
$(Si_{30})_2H_{48}$ chain	-3.176	-2.975		2.412	1.504	-6.060	-2.776	3.284
$(Si_{20})_3$ chain	-3.078	-2.887	0.116	2.430	-	-5.079	-4.407	0.672
$(Si_{20})_3H_{40}$ chain	-3.206	-3.003		2.415	1.503	-6.006	-2.696	3.310
$(Si_{20})_3$ bent chain	-3.079	-2.895	0.109	2.431	-	-5.253	-4.212	1.042
$(Si_{20})_3H_{40}$ bent chain	-3.207	-3.004		2.417	1.503	-5.977	-2.900	3.077
$(Si_{20})_3$ triangle	-3.053	-2.892	0.108	2.419	-	-5.391	-4.210	1.181
$(Si_{20})_3H_{48}$ triangle	-3.205	-3.000		2.413	1.503	-6.279	-2.203	4.075

[a] Average Bond Lengths are given for 6-311G only
[b] HOMO/LUMO gaps are given for 6-311G only
[c] Δ represents the energy increase/decrease due to surface passivation
[d] Δ represents the band gap

allowed the modeling of larger Si_{60} clusters by various additions, as we have done so here. Four structures were investigated: a linear chain of two Si_{30} cages, a similar chain of three Si_{20} cages, a bent version of the Si_{20} chain, and a triangular configuration of Si_{20} cages (fig. A.1d-g). We found the passivated $(Si_{20})_3$ bent chain geometry to be the most stable among our structures with the lowest ground state energy of -3.004 eV/atom. The relaxed structure exhibited an angle of 32.6° with respect to the central unit. Further bending, eventually resulting in the triangle geometry, appeared to be unfavorable with a slight increase in binding energy.

The results of the $(Si_{20})_3$ group suggest that the Si_{20} unit is more suitable for passivation than the Si_{30} unit (table A.2). Calculating the binding energies of the individual Si_{20} and Si_{30}

Table A.3. Binding energies and average bond lengths for Si_n[a] fullerene units under 6-311G

	binding energy (eV/atom)		average bond length (Å)	
geometry	6-311G	Δ	Si-Si	Si-H
Si_{20}	-2.770	0.169	2.445	-
$Si_{20}H_{20}$	-2.939		2.412	1.503
Si_{30}	-2.812	0.120	2.393	-
$Si_{30}H_{30}$	-2.932		2.407	1.504

[a] n = 20, 30

fullerene units, we found differences between pristine and passivated energies of 0.169 eV/atom and 0.120 eV/atom, respectively (table A.3). This result shows that the success of passivation in stabilizing a cluster is dependent on the surface area available for passivation. This is clear when comparing the binding energies of the Si_n group (n = 20, 30, 60).

A.2.2. Electronic Properties

Considering our results for Diamond Cubic and Wurtzite are in agreement with the behavior found in the previous study at the 75-300 atoms size[272], we primarily focused on the hollow-cage geometries and the effects of their passivation on electron densities. Highest Occupied Molecular Orbital (HOMO) and Lowest Unoccupied Molecular Orbital (LUMO) plots for the Si_{60} clusters are given in Figure A.2, while density-of-state (DOS) plots are shown in Figure A.3. As expected, passivation of surface states in the Si_{60} clusters opens up band gaps of ~3-5 eV, with the largest gap observed in the fullerene geometry (table A.2). The reduced gap in the remaining geometries is due to the concentration of highest occupied states around fully-coordinated Si-Si bonds ("Si Core" in fig. A.3). These states effectively decrease the size of the band gap by about 1.5 eV. We note that with thermal or photonic excitations, electrons from these states will transition to the conduction band. However, LUMO plots in Figure A.2 show that these electrons will

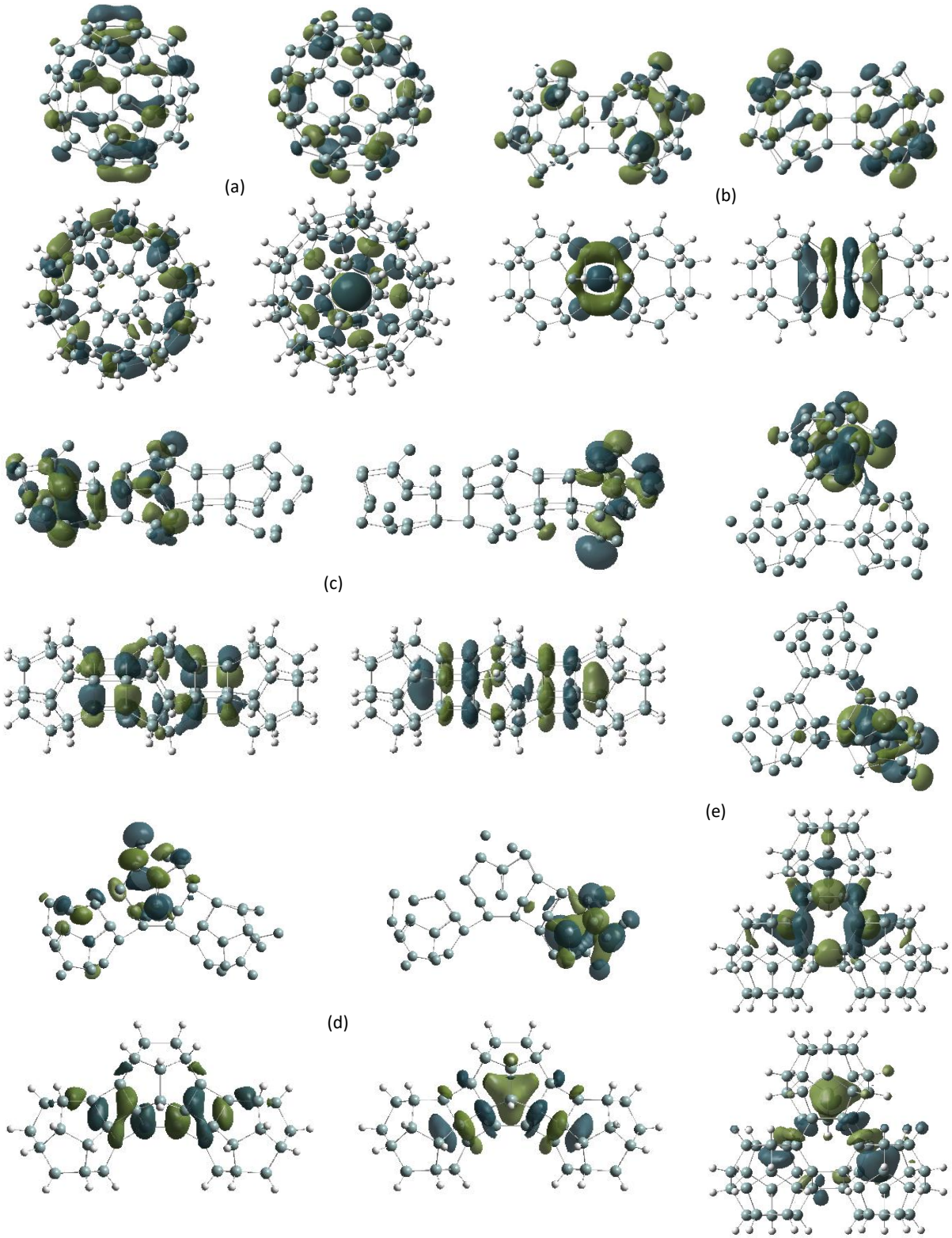

Figure A.2. HOMO (left)/LUMO (right) plots for pristine (top) and passivated (bottom) Si_{60} nanoclusters. (a) Si_{60} fullerene, (b) $(Si_{30})_2$ chain, (c) $(Si_{20})_3$ chain, (d) $(Si_{20})_3$ bent chain, and (e) $(Si_{20})_3$ triangle (from top: pristine HOMO/LUMO; passivated HOMO/LUMO)

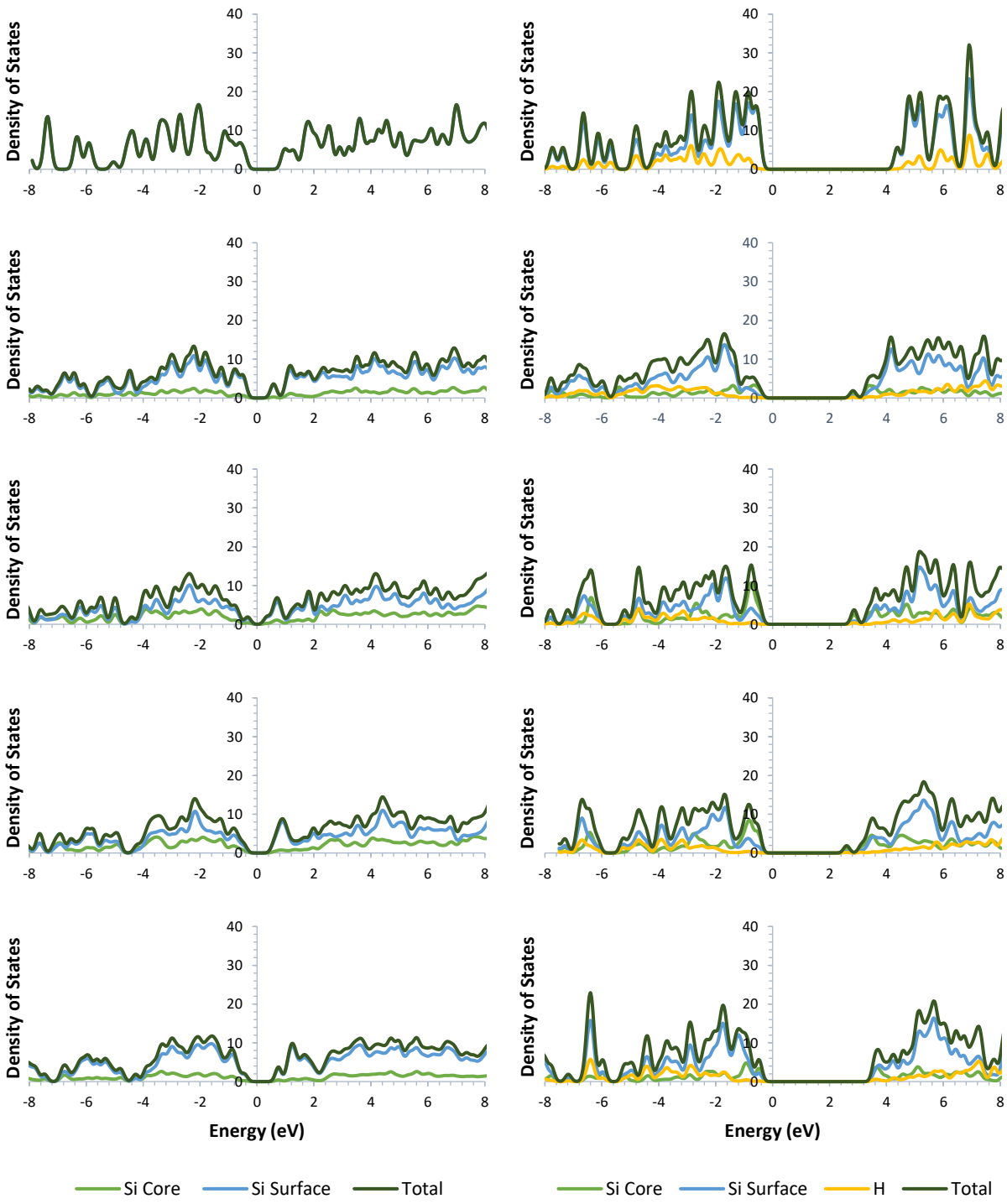

Figure A.3. Density of states for pristine (left) and passivated (right) Si_{60} nanoclusters. From top: Si_{60} fullerene, $(Si_{30})_2$ chain, $(Si_{20})_3$ chain, $(Si_{20})_3$ bent chain, and $(Si_{20})_3$ triangle; "Si Core" refers to fully coordinated Si atoms.

remain localized around the fully coordinated section of the cluster and recombine back into the HOMO, retaining the stability of these bonds. The same cannot be said for the Si_{60} fullerene geometry, in which no fully coordinated Si atoms exist. Passivation of this geometry yields a high concentration of electrons at the Si surface. This result may factor into the stability inconsistencies between the Si_{60} fullerene and the rest of the cage-like structures. Electron concentrations around fully coordinated Si-Si bonds in the linear and bent geometries may be providing an added stability factor that is nonexistent in the Si_{60} fullerene.

A.3. The Si_{60} Fullerene

A.3.1. Stability of Si-Si Bonds

We have seen thus far that the unique fullerene geometry behaves differently under passivation than its derivatives. In the previous section, we noted the lack of fully-coordinated Si-Si bonding in the fullerene geometry and a correlation between the presence of such bonds and the success of passivation in lowering the binding energy. In this light, we were motivated to investigate the effects of exohydrogenation on the Si-Si bonding network of the Si_{60} clusters. This was done by removing a single H atom from the surface of the passivated structure and calculating the electronic energy of the remaining configuration with and without relaxing the structure. This energy was added together with the electronic energy of a single H atom and then subtracted from the previously calculated electronic energy of the fully passivated cluster to yield an average value for the binding energy stored in a Si-H bond for that structure. The result was then multiplied by the number of Si-H bonds for the given geometry and subtracted from the total binding energy of the fully passivated cluster to produce the total binding energy stored within the Si-Si bonding network. Dividing this value by the number of Si atoms in the cluster yielded an average measure of the strength of a Si-Si bond in a passivated Si_{60} cluster.

Using the Si_{60} fullerene as an example, this was done mathematically as follows:

$$\overline{E(Si-H)}_{binding} = E(Si_{60}H_{60}) - [E(Si_{60}H_{59}) + E(H)]$$

, where $E(Si_{60}H_{59})$ was calculated once with initial relaxation and once without, and

$$E(Si\ Core)_{binding} = E(Si_{60}H_{60})_{binding} - n\overline{E(Si-H)}_{binding}$$

$$\overline{E(Si-Si)}_{binding} = E(Si\ Core)_{binding}/60$$

, where n is the number of Si-H bonds in the passivated structure. The difference between the results produced with relaxation and those without was defined as the average relaxation energy required to passivate a single dangling bond (table A.4). For this example, we found the Si-Si binding energy in the passivated fullerene at a value of -2.406 eV/Si atom, 0.525 eV/Si atom weaker than the pristine structure. A similar trend was found in the rest of the structures, with the magnitude of the effect decreasing with the surface area of the cluster. In structures where this

Table A.4. Comparison of Si-Si bonding strength in pristine and passivated clusters

geometry	binding energy[a] (eV/Si atom)	Δ	binding energy relaxed[b] (eV/Si atom)	Δ	relaxation energy[c] (eV/Si atom)
Si_{60} fullerene	-2.932	-0.525	-2.932	-0.272	-0.253
$Si_{60}H_{60}$ fullerene	-2.406		-2.660		
$(Si_{30})_2$ chain	-2.884	-0.282	-2.884	-0.256	-0.027
$(Si_{30})_2H_{48}$ chain	-2.602		-2.629		
$(Si_{20})_3$ chain	-2.887	-0.201	-2.887	-0.197	-0.004
$(Si_{20})_3H_{40}$ chain	-2.686		-2.690		
$(Si_{20})_3$ bent chain	-2.895	-0.190	-2.895	-0.185	-0.005
$(Si_{20})_3H_{40}$ bent chain	-2.705		-2.710		
$(Si_{20})_3$ triangle	-2.892	-0.279	-2.892	-0.275	-0.005
$(Si_{20})_3H_{48}$ triangle	-2.613		-2.618		

[a] Calculated from single point energies of $Si_{60}H_{n-1}$ clusters
[b] Calculated from optimized (relaxed) $Si_{60}H_{n-1}$ clusters
[c] Relaxation energy is given as the difference between columns 2 and 4 and represents the strain on the local environment of a Si atom upon forming a Si-H bond

effect is minimal, the passivation process is energetically favorable suggesting that the Si-H bonds are able to compensate for the weaker Si-Si bonding network. This balancing act is perhaps insufficient in the Si_{60} fullerene geometry, in which the weakening of the Si-Si bonds is largest.

Note that the relaxation energy incurred by the Si_{60} fullerene in receiving each additional H atom, -0.253 eV/Si atom, is also largest in magnitude among the Si_{60} clusters. This may be due to the hollow nature of the spherical geometry which allows for greater freedom in reshaping the local environment of the receiving Si atom towards the preferable tetrahedral configuration. Lower relaxation energies found in the Si_{20}-based structures may also explain the higher stability of these clusters under passivation. Both values – weakening of Si-Si bonding and relaxation energy – suggest that the fullerene geometry may be uniquely unsuited for exohydrogenation. This may also indicate why a Si fullerene, passivated or not, has yet to be found experimentally. In a competing chemical environment, smaller segment of Si will be passivated and be unable to form Si_{60} fullerene structure.

A.3.2. Aromatic Stabilization

It has been shown that the Si_{60} fullerene, like its carbon counterpart, exhibits a level of charge delocalization in its six-membered rings, though less than that found in C_{60}[273]. It is also generally understood that Si prefers sp^3 hybridization and any sp^2 bonds tend to destabilize. However, a recent study using reflection electron energy loss spectroscopy has characterized sp^2 hybridization in silicene, the Si counterpart to carbon's graphene and SiC graphene-like structures[299,300]. This motivated a search for possible sp^2 hybridization characterized by formation of π bonds in the rings of the Si_{60} fullerene.

Comparing the approximated radii of the pristine and passivated Si_{60} fullerenes, 5.378 Å and 5.972 Å, respectively, we hypothesized that due to the smaller radius of the pristine Si_{60}

fullerene, molecular orbitals might be in sufficient proximity to establish π bonding. In Figure A.2a, the HOMO plot of the pristine Si_{60} fullerene clearly shows a level of π bonding at the surface. The passivated counterpart shows no sp^2-type bonds, which is to be expected considering the larger 2.408 Å average bond length (table A.2). This mixing of sp^3- and sp^2-type bonding found in the pristine fullerene may additionally explain the higher stability over its passivated counterpart. Sp^2-type bonding is seen only in the Si_{60} fullerene geometry, in which the smallest bond lengths were about 2.26 Å. In the rest of the cage-like clusters, the smallest bond lengths were greater than 2.32 Å. This is due to the larger radius of the Si_{60} fullerene, which suggests that Si based hollow geometries in the nanoscale are more stable in larger dimensions than their carbon counterparts.

A.4. Conclusions

Several configurations of Si_{60} have been investigated with hybrid density functional theory and were found at this size to be more stable under hydrogen passivation with respect to the bulk diamond cubic phase. The lowest, most stable ground state among the investigated geometries was found in the $(Si_{20})_3H_{40}$ bent chain and was concluded to be a function of both the bending angle and the lower required number of H atoms in the passivation process. The Si_{60} fullerene exhibited anomalous binding energy values with respect to the passivation trend of positive effect on stability and thus was further investigated. The pristine structure showed the presence of sp^2-type bonding and was found to be energetically favorable over its passivated counterpart. Additional investigation of the internal Si-Si network found that in the process of exohydrogenation, a balance between the weakening of Si-Si bonds and the passivation of surface strain contributed to the overall stability of the structure. Results again suggest that exohydrogenation is not favorable in the Si_{60} fullerene geometry and that the reason lies in its bonding properties. In addition, we conclude that

the success of passivation depends on the surface area requiring passivation, with nanoclusters of larger surface area favoring pristine states.

Acknowledgements

All computations were performed on the High Performance Center servers at the University of Texas at Arlington.

References

1 UN Department of Economic and Social Affairs, *World population prospects*, 2019.

2 US Energy Information Administration, *International Energy Outlook*, 2019.

3 Organización Mundial de la Meteorología, *WMO statement on the status of the global climate in 2019*, 2020.

4 Climate Change: How Do We Know, https://climate.nasa.gov/evidence/.

5 J. Tsao, N. Lewis and G. Crabtree, *US Dep. Energy*, 2006, 1–24.

6 A. Lopez, B. Roberts, D. Heimiller, N. Blair and G. Porro, *Natl. Renew. Energy Lab. Doc.*, 2012, **1**, 1–40.

7 P. Moriarty and D. Honnery, *Int. J. Hydrogen Energy*, 2007, **32**, 1616–1624.

8 Z. Chen, H. N. Dinh and E. Miller, *Photoelectrochemical Water Splitting*, Springer New York, New York, NY, 2013.

9 E. Connelly, A. Elgowainy and M. Ruth, 2019, 2–6.

10 G. W. Crabtree and M. S. Dresselhaus, *MRS Bull.*, 2008, **33**, 421–428.

11 B. Y. Alfaifi, H. Ullah, S. Alfaifi, A. A. Tahir and T. K. Mallick, *Veruscript Funct. Nanomater.*, 2018, **2**, 1–26.

12 DOE, *FY 2018 Progress Report for the DOE Hydrogen and Fuel Cells Program*, 2019.

13 M. G. Walter, E. L. Warren, J. R. McKone, S. W. Boettcher, Q. Mi, E. A. Santori and N. S. Lewis, *Chem. Rev.*, 2010, **110**, 6446–6473.

14 A. Fujishima and K. Honda, *Nature*, 1972, **238**, 37–38.

15 S. Rühle, A. Y. Anderson, H. N. Barad, B. Kupfer, Y. Bouhadana, E. Rosh-Hodesh and A. Zaban, *J. Phys. Chem. Lett.*, 2012, **3**, 3755–3764.

16 Y. Chen, X. Feng, Y. Liu, X. Guan, C. Burda and L. Guo, *ACS Energy Lett.*, 2020, **5**, 844–866.

17 C. Ros, T. Andreu and J. R. Morante, *J. Mater. Chem. A*, 2020, **8**, 10625–10669.

18 Y. Yan and S. H. Wei, *Phys. Status Solidi Basic Res.*, 2008, **245**, 641–652.

19 H. Deng, J. Luo and S. Wei, *Chinese Phys. B*, 2018, **27**, 117104.

20 S. Sheng, G. Fang, C. Li, S. Xu and X. Zhao, *Phys. Status Solidi Appl. Mater. Sci.*, 2006, **203**, 1891–1900.

21 M. N. Huda, Y. Yan, A. Walsh, S. H. Wei and M. M. Al-Jassim, *Phys. Rev. B - Condens. Matter Mater. Phys.*, 2009, **80**, 1–7.

22 H. Kawazoe, H. Yanagi, K. Ueda and H. Hosono, *MRS Bull.*, 2000, **25**, 28–36.

23 R. Nagarajan, N. Duan, M. . Jayaraj, J. Li, K. . Vanaja, A. Yokochi, A. Draeseke, J. Tate

and A. . Sleight, *Int. J. Inorg. Mater.*, 2001, **3**, 265–270.

24 N. Zhang, J. Sun and H. Gong, *Coatings*, 2019, **9**, 1–27.

25 U. A. Joshi, A. Palasyuk, D. Arney and P. A. Maggard, *J. Phys. Chem. Lett.*, 2010, **1**, 2719–2726.

26 H. C. Kandpal and R. Seshadri, *Solid State Sci.*, 2002, **4**, 1045–1052.

27 N. Saito, H. Kadowaki, H. Kobayashi, K. Ikarashi, H. Nishiyama and Y. Inoue, *Chem. Lett.*, 2004, **33**, 1452–1453.

28 H. Kadowaki, N. Saito, H. Nishiyama, H. Kobayashi, Y. Shimodaira and Y. Inoue, *J. Phys. Chem. C*, 2007, **111**, 439–444.

29 A. Walsh, Y. Yan, M. N. Huda, M. M. Al-Jassim and S. H. Wei, *Chem. Mater.*, 2009, **21**, 547–551.

30 T. Saison, N. Chemin, C. Chanéac, O. Durupthy, L. Mariey, F. Maugé, V. Brezová and J.-P. Jolivet, *J. Phys. Chem. C*, 2015, **119**, 12967–12977.

31 K. Tolod, S. Hernández and N. Russo, *Catalysts*, 2017, **7**, 13.

32 I. D. Sharp, J. K. Cooper, F. M. Toma and R. Buonsanti, *ACS Energy Lett.*, 2017, **2**, 139–150.

33 A. J. E. Rettie, H. C. Lee, L. G. Marshall, J. F. Lin, C. Capan, J. Lindemuth, J. S. McCloy, J. Zhou, A. J. Bard and C. B. Mullins, *J. Am. Chem. Soc.*, 2013, **135**, 11389–11396.

34 A. J. E. Rettie, W. D. Chemelewski, D. Emin and C. B. Mullins, *J. Phys. Chem. Lett.*, 2016, **7**, 471–479.

35 Y. Hermans, S. Murcia-López, A. Klein, R. van de Krol, T. Andreu, J. R. Morante, T. Toupance and W. Jaegermann, *Phys. Chem. Chem. Phys.*, 2019, **21**, 5086–5096.

36 Y. Hermans, A. Klein, K. Ellmer, R. van de Krol, T. Toupance and W. Jaegermann, *J. Phys. Chem. C*, 2018, **122**, 20861–20870.

37 H. P. Sarker, P. M. Rao and M. N. Huda, *ChemPhysChem*, 2019, **20**, 773–784.

38 A. Nielander and N. S. Lewis, 2015.

39 B. Koo, S. Byun, S. W. Nam, S. Y. Moon, S. Kim, J. Y. Park, B. T. Ahn and B. Shin, *Adv. Funct. Mater.*, 2018, **28**, 1–8.

40 B. Tudu, R. Bortamuly and P. Saikia, in *Photoelectrochemical Water Splitting - Materials and Applications*, 2020, pp. 183–213.

41 T. J. Jacobsson, V. Fjällström, M. Edoff and T. Edvinsson, *Sol. Energy Mater. Sol. Cells*, 2015, **134**, 185–193.

42 Y. F. Tay, H. Kaneko, S. Y. Chiam, S. Lie, Q. Zheng, B. Wu, S. S. Hadke, Z. Su, P. S. Bassi, D. Bishop, T. C. Sum, T. Minegishi, J. Barber, K. Domen and L. H. Wong, *Joule*, 2018, **2**, 537–548.

43 J. Liu, D.-M. Zhuang, M.-J. Cao, C.-Y. Wang, M. Xie and X.-L. Li, *Int. J. Photoenergy*, 2012, **2012**, 1–7.

44 S. Chen, J. H. Yang, X. G. Gong, A. Walsh and S. H. Wei, *Phys. Rev. B - Condens. Matter Mater. Phys.*, 2010, **81**, 35–37.

45 P. Sarker, M. M. Al-Jassim and M. N. Huda, *J. Appl. Phys.*, 2015, **117**, 035702.

46 D. Muñoz-Rojas, G. Subías, J. Oró-Solé, J. Fraxedas, B. Martínez, M. Casas-Cabanas, J. Canales-Vázquez, J. Gonzalez-Calbet, E. García-González, R. I. Walton and N. Casañ-Pastor, *J. Solid State Chem.*, 2006, **179**, 3883–3892.

47 K. Keerthi, B. G. Nair, M. D. Benoy, R. Raphael and R. R. Philip, *Mater. Chem. Phys.*, 2017, **199**, 591–596.

48 K. Rajeshwar, M. K. Hossain, R. T. Macaluso, C. Janáky, A. Varga and P. J. Kulesza, *J. Electrochem. Soc.*, 2018, **165**, H3192–H3206.

49 P. Sarker, D. Prasher, N. Gaillard and M. N. Huda, *J. Appl. Phys.*, 2013, **114**, 133508.

50 L. Zhou, E. Bainglass, M. Masroor, B. Giri, G. Li, A. Carl, R. L. Grimm, M. N. Huda, L. V. Titova and P. M. Rao, *J. Mater. Chem. A*, 2021, **9**, 1643–1654.

51 R. G. Parr and W. T. Yang, *Density-Functional Theory of Atoms and Molecules*, 1989.

52 R. O. Jones, *Rev. Mod. Phys.*, 2015, **87**, 897–923.

53 K. Capelle, *Brazilian J. Phys.*, 2006, **36**, 1318–1341.

54 C. J. Cramer, *Essential of Computational Chemistry. Theories and Models*, John Wiley and Sons, Ltd., Chichester., 2nd edn., 2004.

55 W. Kohn, *Rev. Mod. Phys.*, 1999, **71**, 1253–1266.

56 P. Hohenberg and W. Kohn, *Phys. Rev.*, 1964, **136**, 1912–1919.

57 W. Kohn and L. J. Sham, *Phys. Rev.*, 1965, **140**, 1–6.

58 E. Fermi, *Rend. Accad. Naz. Lincei*, 1927, **32**, 602–607.

59 L. H. Thomas, *Math. Proc. Cambridge Philos. Soc.*, 1927, **23**, 542.

60 D. C. Langreth and M. J. Mehl, *Phys. Rev. B*, 1983, **28**, 1809–1834.

61 P. A. M. Dirac, *Math. Proc. Cambridge Philos. Soc.*, 1930, **26**, 376–385.

62 S. H. Vosko, L. Wilk and M. Nusair, *Can. J. Phys.*, 1980, **58**, 1200–1211.

63 G. L. Oliver and J. P. Perdew, *Phys. Rev. A*, 1979, **20**, 397–403.

64 V. Sahni, K. P. Bohnen and M. K. Harbola, *Phys. Rev. A*, 1988, **37**, 1895–1907.

65 P. R. Antoniewicz and L. Kleinman, *Phys. Rev. B*, 1985, **31**, 6779–6781.

66 J. P. Perdew, K. Burke and M. Ernzerhof, *Phys. Rev. Lett.*, 1996, **77**, 3865–3868.

67 J. P. Perdew, J. A. Chevary, S. H. Vosko, K. A. Jackson, M. R. Pederson, D. J. Singh and

C. Fiolhais, *Phys. Rev. B*, 1992, **46**, 6671–6687.

68 G. Ortiz, *Phys. Rev. B*, 1992, **45**, 11328–11331.

69 C. Bowen, G. Sugiyama and B. J. Alder, *Phys. Rev. B*, 1994, **50**, 14838–14848.

70 S. Moroni, D. M. Ceperley and G. Senatore, *Phys. Rev. Lett.*, 1995, **75**, 689–692.

71 C. Filippi, D. J. Singh and C. J. Umrigar, *Phys. Rev. B*, 1994, **50**, 14947–14951.

72 J. L. Bao, L. Gagliardi and D. G. Truhlar, *J. Phys. Chem. Lett.*, 2018, **9**, 2353–2358.

73 F. Zhou, C. A. Marianetti, M. Cococcioni, D. Morgan and G. Ceder, *Phys. Rev. B - Condens. Matter Mater. Phys.*, 2004, **69**, 201101.

74 A. D. Becke, *J. Chem. Phys.*, 1993, **98**, 1372–1377.

75 J. Heyd, G. E. Scuseria and M. Ernzerhof, *J. Chem. Phys.*, 2003, **118**, 8207–8215.

76 M. Cococcioni, in *Correlated Electrons: Modeling and Simulation*, 2012.

77 S. L. Dudarev, G. A. Botton, S. Y. Savrasov, C. J. Humphreys and A. P. Sutton, *Phys. Rev. B*, 1998, **57**, 1505–1509.

78 G. Kresse, M. Marsman and J. Furthmüller, *Manual*, 2014, 237.

79 R. P. Feynman, *Phys. Rev.*, 1939, **56**, 340–343.

80 P. Pulay, *Mol. Phys.*, 1969, **17**, 197–204.

81 G. P. Francis and M. C. Payne, *J. Phys. Condens. Matter*, 1990, **2**, 4395–4404.

82 Von N. W. Ashcroft; N. D. Mermin, *Phys. unserer Zeit*, 1978, **9**, 33–33.

83 H. J. Monkhorst and J. D. Pack, *Phys. Rev. B*, 1976, **13**, 5188–5192.

84 P. E. Blöchl, *Phys. Rev. B*, 1994, **50**, 17953–17979.

85 L. D. Whalley, J. M. Frost, B. J. Morgan and A. Walsh, *Phys. Rev. B*, 2019, **99**, 085207.

86 P. Y. Yu and M. Cardona, *Fundamentals of Semiconductors - Physics and Materials Properties*, Springer, 3rd edn., 2005.

87 R. F. W. Bader, *Acc. Chem. Res.*, 1985, **18**, 9–15.

88 K. Momma and F. Izumi, *J. Appl. Crystallogr.*, 2008, **41**, 653–658.

89 H. Kadowaki, N. Saito, H. Nishiyama, H. Kobayashi, Y. Shimodaira and Y. Inoue, *J. Phys. Chem. C*, 2007, **111**, 439–444.

90 C. Janáky, K. Rajeshwar, N. R. de Tacconi, W. Chanmanee and M. N. Huda, *Catal. Today*, 2013, **199**, 53–64.

91 D. W. Kim, I.-S. Cho, S. S. Shin, S. Lee, T. H. Noh, D. H. Kim, H. S. Jung and K. S. Hong, *J. Solid State Chem.*, 2011, **184**, 2103–2107.

92 J. Tang and J. Ye, *J. Mater. Chem.*, 2005, **15**, 4246–4251.

93 J. Nilsson, A. Landa-Cánovas, S. Hansen and A. Andersson, *Catal. Today*, 1997, **33**, 97–108.

94 C. E. Kim, S. H. Yoo, D. F. Bahr, C. Stampfl and A. Soon, *Inorg. Chem.*, 2017, **56**, 6545–6550.

95 S. H. Kim, S. Park, C. W. Lee, B. S. Han, S. W. Seo, J. S. Kim, I. S. Cho and K. S. Hong, *Int. J. Hydrogen Energy*, 2012, **37**, 16895–16902.

96 M. N. Huda, A. Walsh, Y. Yan, S.-H. Wei and M. M. Al-Jassim, *Cit. J. Appl. Phys.*, 2010, **107**, 224706.

97 K. T. Butler, J. M. Frost and A. Walsh, *Energy Environ. Sci.*, 2015, **8**, 838–848.

98 H. Irie, M. Miyayama and T. Kudo, *J. Appl. Phys.*, 2001, **90**, 4089–4094.

99 S. E. Cummins and L. E. Cross, *J. Appl. Phys.*, 1968, **39**, 2268–2274.

100 V. M. Fridkin, *Photoferroelectrics*, Springer-Verlag, 1st edn., 1979.

101 N. D. Gavrilova, A. M. Lotonov and A. A. Kornilova, *Inorg. Mater.*, 2008, **44**, 171–175.

102 G. Kresse and D. Joubert, *Phys. Rev. B*, 1999, **59**, 1758–1775.

103 G. Kresse and J. Furthmüller, *Phys. Rev. B - Condens. Matter Mater. Phys.*, 1996, **54**, 11169–11186.

104 G. Kresse and J. Furthmüller, *Comput. Mater. Sci.*, 1996, **6**, 15–50.

105 M. Methfessel and A. T. Paxton, *Phys. Rev. B*, 1989, **40**, 3616–3621.

106 P. E. Blöchl, O. Jepsen and O. K. Andersen, *Phys. Rev. B*, 1994, **49**, 16223–16233.

107 V. I. Anisimov, J. Zaanen and O. K. Andersen, *Phys. Rev. B*, 1991, **44**, 943.

108 M. V. Ganduglia-Pirovano, A. Hofmann and J. Sauer, *Surf. Sci. Rep.*, 2007, **62**, 219–270.

109 E. Şaşioğlu, C. Friedrich and S. Blügel, *Phys. Rev. B - Condens. Matter Mater. Phys.*, 2011, **83**, 121101–121102.

110 W. Setyawan, G. L. W. Hart, H. T. Stokes, M. Jahnatek, D. Morgan, D. O. Demchenko, J. Xue, R. V. Chepulskii, R. H. Taylor, M. J. Mehl, O. Levy, S. Wang, K. Yang and S. Curtarolo, *Comput. Mater. Sci.*, 2012, **58**, 218–226.

111 G. Henkelman, A. Arnaldsson and H. Jónsson, *Comput. Mater. Sci.*, 2006, **36**, 354–360.

112 E. Sanville, S. D. Kenny, R. Smith and G. Henkelman, *J. Comput. Chem.*, 2007, **28**, 899–908.

113 W. Tang, E. Sanville and G. Henkelman, *J. Phys. Condens. Matter*, 2009, **21**, 084204.

114 M. Yu and D. R. Trinkle, *J. Chem. Phys.*, 2011, **134**, 064111.

115 M. P. Marder, *Condensed Matter Physics*, Wiley, 2nd edn., 2015.

116 A. R. Lim, S. H. Choh and Min Su Jang, *J. Phys. Condens. Matter*, 1995, **7**, 7309–7323.

117 J. D. Bierlein and A. W. Sleight, *Solid State Commun.*, 1975, **16**, 69–70.

118 A. W. Sleight, H. y. Chen, A. Ferretti and D. E. Cox, *Mater. Res. Bull.*, 1979, **14**, 1571–1581.

119 G. Dreyer and E. Tillmanns, *Neues Jahrb. Miner.*, 1981, 151–154.

120 M. M. Qurashi and W. H. Barnes, *Am. Mineral.*, 1953, **38**, 489–500.

121 A. Jain, S. P. Ong, G. Hautier, W. Chen, W. D. Richards, S. Dacek, S. Cholia, D. Gunter, D. Skinner, G. Ceder, K. A. Persson, D. Skinner, W. Chen, S. Cholia, G. Hautier, D. Gunter, S. P. Ong, S. Dacek, W. D. Richards, A. Jain, G. Ceder, S. P. Ong, G. Hautier, W. Chen, W. D. Richards, S. Dacek, S. Cholia, D. Gunter, D. Skinner, G. Ceder and K. A. Persson, *APL Mater.*, 2013, **1**, 011002.

122 C. Keller, *ZAAC - J. Inorg. Gen. Chem.*, 1962, **318**, 89–106.

123 R. Roth and J. Waring, *Am. Mineral.*, 1963, **18**, 1348–1356.

124 M. P. Ghimire, Sandeep, T. P. Sinha and R. K. Thapa, *Phys. B Condens. Matter*, 2011, **406**, 3454–3457.

125 V. I. Popolitov, A. N. Lobachev and V. F. Peskin, *Ferroelectrics*, 1982, **40**, 9–16.

126 N. V. Zubkova, D. Y. Pushcharovsky, G. Giester, A. S. Smolin, E. Tillmanns, F. Brandstätter, V. Hammer, I. S. Peretyazhko, A. N. Sapozhnikov and A. A. Kashaev, *Neues Jahrb. für Mineral. - Monatshefte*, 2002, **2002**, 145–159.

127 F. Wang, C. Di Valentin and G. Pacchioni, *J. Phys. Chem. C*, 2011, **115**, 8345–8353.

128 X. Nie, S. H. Wei and S. B. Zhang, *Phys. Rev. Lett.*, 2002, **88**, 4.

129 Y. Ogo, H. Hiramatsu, K. Nomura, H. Yanagi, T. Kamiya, M. Hirano and H. Hosono, *Appl. Phys. Lett.*, 2008, **93**, 032113.

130 I. Hargittai and B. Chamberland, *Comput. Math. with Appl.*, 1986, **12**, 1021–1038.

131 A. Walsh, D. J. Payne, R. G. Egdell and G. W. Watson, *Chem. Soc. Rev.*, 2011, **40**, 4455.

132 C. E. Mohn and S. Stølen, *Phys. Rev. B - Condens. Matter Mater. Phys.*, 2011, **83**, 14103.

133 E. Bainglass and M. N. Huda, *J. Electrochem. Soc.*, 2019, **166**, H3195–H3201.

134 W. Li, X. Wang, Z. Wang, Y. Meng, X. Sun, T. Yan, J. You and D. Kong, *Mater. Res. Bull.*, 2016, **83**, 259–267.

135 K. E. Kweon, G. S. Hwang, J. Kim, S. Kim and S. Kim, *Phys. Chem. Chem. Phys.*, 2015, **17**, 256–260.

136 O. Monfort and G. Plesch, *Environ. Sci. Pollut. Res.*, 2018, **25**, 19362–19379.

137 M. A., M. J., M. Ashokkumar and P. Arunachalam, *Appl. Catal. A Gen.*, 2018, **555**, 47–74.

138 T. Saison, P. Gras, N. Chemin, C. Chanéac, O. Durupthy, V. Brezová, C. Colbeau-Justin

and J. P. Jolivet, *J. Phys. Chem. C*, 2013, **117**, 22656–22666.

139 X. Ding, K. Zhao and L. Zhang, *Environ. Sci. Technol.*, 2014, **48**, 5823–5831.

140 C. Zhang and Y. Zhu, *Chem. Mater.*, 2005, **17**, 3537–3545.

141 N. Zhang, R. Ciriminna, M. Pagliaro and Y.-J. Xu, *Chem. Soc. Rev.*, 2014, **43**, 5276–5287.

142 S. Girish Kumar and K. S. R. Koteswara Rao, *Appl. Surf. Sci.*, 2015, **355**, 939–958.

143 J. Tang, Z. Zou and J. Ye, *Catal. Letters*, 2004, **92**, 53–56.

144 F. Ren, J. Zhang and Y. Wang, *RSC Adv.*, 2015, **5**, 29058–29065.

145 R. Radha, A. Srinivasan, P. Manimuthu and S. Balakumar, *J. Mater. Chem. C*, 2015, **3**, 10285–10292.

146 M. Ge, Y. Li, L. Liu, Z. Zhou and W. Chen, *J. Phys. Chem. C*, 2011, **115**, 5220–5225.

147 X. Zhang, Y. Gong, X. Dong, X. Zhang, C. Ma and F. Shi, *Mater. Chem. Phys.*, 2012, **136**, 472–476.

148 Z. Zhu, Y. Yan and J. Li, *Micro Nano Lett.*, 2015, **10**, 460–464.

149 Z. Liu, Q. Yu, J. Liu, T. Li and F. Huang, *Micro Nano Lett.*, 2017, **12**, 195–200.

150 S. Li, S. Hu, W. Jiang, Y. Liu, J. Liu and Z. Wang, *J. Colloid Interface Sci.*, 2017, **501**, 156–163.

151 L. Jiang, S. Wang, L. Shi, Y. Zhao, Z. Wang, M. Zhang and S. Yuan, *Chinese J. Chem.*, 2017, **35**, 183–188.

152 F. Opoku, K. K. Govender, C. G. C. E. van Sittert and P. P. Govender, *Appl. Surf. Sci.*, 2018, **427**, 487–498.

153 J. Jia, P. Xue, R. Wang, X. Bai, X. Hu, J. Fan and E. Liu, *J. Chem. Technol. Biotechnol.*, 2018, **93**, 2988–2999.

154 Q. Guo, Y. Huang, H. Xu, D. Luo, F. Huang, L. Gu, Y. Wei, H. Zhao, L. Fan and J. Wu, *Solid State Sci.*, 2018, **78**, 95–106.

155 X. Lu, W. Che, X. Hu, Y. Wang, A. Zhang, F. Deng, S. Luo and D. D. Dionysiou, *Chem. Eng. J.*, 2019, **356**, 819–829.

156 L. Zhang, Y. Man and Y. Zhu, *ACS Catal.*, 2011, **1**, 841–848.

157 C. Bhattacharya, H. C. Lee and A. J. Bard, *J. Phys. Chem. C*, 2013, **117**, 9633–9640.

158 A. Phuruangrat, P. Dumrongrojthanath, S. Thongtem and T. Thongtem, *Mater. Lett.*, 2018, **224**, 67–70.

159 B. Aurivillius, *Ark. foer Kemi*, 1952, **5**, 39–47.

160 P. Millán, A. Castro and J. B. Torrance, *Mater. Res. Bull.*, 1993, **28**, 117–122.

161 A. Castro, P. Millán, M. J. Martínez-Lope and J. B. Torrance, *Solid State Ionics*, 1993, **63**–**65**, 897–901.

162 A. Castro, P. Millan, R. Enjalbert, E. Snoeck and J. Galy, *Mater. Res. Bull.*, 1994, **29**, 871–879.

163 A. Castro, P. Millan and R. Enjalbert, *Mater. Res. Bull.*, 1995, **30**, 871–882.

164 P. Millan, A. Ramirez and A. Castro, *Mater. Sci. Lett.*, 1995, **14**, 1657–1660.

165 C. D. Ling, R. L. Withers, A. D. Rae, S. Schmid and J. G. Thompson, *Acta Crystallogr. Sect. B Struct. Sci.*, 1996, **52**, 610–615.

166 A. Martínez-de la Cruz and F. E. Longoria Rodríguez, *Mater. Res. Bull.*, 2007, **42**, 1851–1855.

167 A. Singh, D. P. Dutta, M. Roy, A. K. Tyagi and M. H. Fulekar, *J. Mater. Sci.*, 2014, **49**, 2085–2097.

168 A. De Vita, Keele University, 1992.

169 V. I. Anisimov, J. Zaanen and O. K. Andersen, *Phys. Rev. B*, 1991, **44**, 943–954.

170 R. W. Wolfe, R. E. Newnahm and M. I. Kay, *Solid State Commun.*, 1969, **7**, 1797–1801.

171 C. M. Rost, E. Sachet, T. Borman, A. Moballegh, E. C. Dickey, D. Hou, J. L. Jones, S. Curtarolo and J. P. Maria, *Nat. Commun.*, 2015, **6**, 8485.

172 W. H. Baur, *Acta Crystallogr. Sect. B Struct. Crystallogr. Cryst. Chem.*, 1974, **30**, 1195–1215.

173 V. Kapos, J. Hutton, M. B. J. Harfoot, D. P. Tittensor, N. D. Burgess, S. Knight, M. I. Jones, S. Blyth, J. P. W. Scharlemann, S. Brooks, A. P. Arnell and S. H. M. Butchart, *Conserv. Lett.*, 2018, **11**, 1–13.

174 F. Perera, *Envorimental Heal. Perspect.*, 2017, **125**, 141–48.

175 H. Hosseinzadeh-Bandbafha, M. Tabatabaei, M. Aghbashlo, M. Khanali and A. Demirbas, *Energy Convers. Manag.*, 2018, **174**, 579–614.

176 EIA, *U.S. Energy information administration*, 2017.

177 *Office of Energy Efficiency & Renewable Energy*, 2014.

178 J. Zeitouny, E. A. Katz, A. Dollet and A. Vossier, *Sci. Rep.*, 2017, **7**, 1–9.

179 H. Kawasaki, K. Konishi, D. Adachi, H. Uzu, T. Irie, K. Yoshikawa, K. Nakano, T. Uto, W. Yoshida, K. Yamamoto and M. Kanematsu, *Nat. Energy*, 2017, **2**, 17032.

180 K. Thornton and M. Asta, *Model. Simul. Mater. Sci. Eng.*, 2005, **13**, R53–R69.

181 S. R. Kalidindi and M. De Graef, *Annu. Rev. Mater. Res.*, 2015, **45**, 171–193.

182 Ziv Hameiri, *Prog. Photovoltaics*, 2016, **24**, 405–407.

183 N. Tsuda, K. Nasu, A. Fujimori and K. Siratori, *Electronic Conduction in Oxides*,

Springer, Berlin, 2nd edn., 2000.

184 H. Naderi, M. M. Matin and A. R. Bahrami, *J. Biomater. Appl.*, 2011, **26**, 383–417.

185 T. Minami, *Semicond. Sci. Technol.*, 2005, **20**, S35–S44.

186 F. U. Hamelmann, *J. Phys. Conf. Ser.*, 2014, **559**, 012016.

187 S. C. Dixon, D. O. Scanlon, C. J. Carmalt and I. P. Parkin, *J. Mater. Chem. C*, 2016, **4**, 6946–6961.

188 P. P. Edwards, A. Porch, M. O. Jones, D. V. Morgan and R. M. Perks, *Dalt. Trans.*, 2004, 2995.

189 K. H. L. Zhang, K. Xi, M. G. Blamire and R. G. Egdell, *J. Phys. Condens. Matter*, 2016, **28**, 383002.

190 G. Hautier, A. Miglio, G. Ceder, G.-M. Rignanese and X. Gonze, *Nat. Commun.*, 2013, **4**, 2292.

191 M. N. Huda, M. M. Al-Jassim and J. A. Turner, *J. Renew. Sustain. Energy*, 2011, **3**, 053101.

192 A. Bhatia, G. Hautier, T. Nilgianskul, A. Miglio, G.-M. Rignanese, X. Gonze, J. Suntivich, J. Sun, H. J. H. H. J. Kim, ‖ Kee, H. J. H. H. J. Kim, S. Chen, G.-M. Rignanese, X. Gonze, J. Suntivich, J. Sun, H. J. H. H. J. Kim, ‖ Kee, H. J. H. H. J. Kim, S. Chen, G.-M. Rignanese, X. Gonze and J. Suntivich, *Chem. Mater.*, 2016, **28**, 30–34.

193 H. Kawazoe, M. Yasukawa, H. Hyodo, M. Kurita, H. Yanagi and H. Hosono, *Nature*, 1997, **389**, 939–942.

194 H. Hiramatsu, K. Ueda, H. Ohta, M. Hirano, T. Kamiya and H. Hosono, *Appl. Phys. Lett.*, 2003, **82**, 1048.

195 H. Hiramatsu, K. Ueda, H. Ohta, M. Orita, M. Hirano and H. Hosono, *Thin Solid Films*, 2002, **411**, 125–128.

196 A. Y. Anderson, Y. Bouhadana, H. N. Barad, B. Kupfer, E. Rosh-Hodesh, H. Aviv, Y. R. Tischler, S. Rühle and A. Zaban, *ACS Comb. Sci.*, 2014, **16**, 53–65.

197 T. Minami, Y. Nishi and T. Miyata, *Appl. Phys. Express*, 2016, **9**, 052301.

198 A. A. Pomeransky and I. B. Khriplovich, *Surv. High Energy Phys.*, 1999, **14**, 145–173.

199 T. Dimopoulos, A. Peić, P. Müllner, M. Neuschitzer, R. Resel, S. Abermann, M. Postl, E. J. W. List, S. Yakunin, W. Heiss and H. Brückl, *J. Renew. Sustain. Energy*, 2013, **5**, 011205.

200 S. Masudy-Panah, K. Radhakrishnan, H. R. Tan, R. Yi, T. I. Wong and G. K. Dalapati, *Sol. Energy Mater. Sol. Cells*, 2015, **140**, 266–274.

201 J. Morasch, H. F. Wardenga, W. Jaegermann and A. Klein, *Phys. Status Solidi Appl. Mater. Sci.*, 2016, **213**, 1615–1624.

202 A. Bhaumik, A. Haque, P. Karnati, M. F. N. Taufique, R. Patel and K. Ghosh, *Thin Solid Films*, 2014, **572**, 126–133.

203 I. Repins, M. A. Contreras, B. Egaas, C. DeHart, J. Scharf, C. L. Perkins, B. To and R. Noufi, *Prog. Photovoltaics Res. Appl.*, 2008, **16**, 235–239.

204 W. Wang, M. T. Winkler, O. Gunawan, T. Gokmen, T. K. Todorov, Y. Zhu and D. B. Mitzi, *Adv. Energy Mater.*, 2014, **4**, 1301465.

205 R. B. Hall and J. D. Meakin, *Thin Solid Films*, 1979, **63**, 203–211.

206 A. Polman, M. Knight, E. C. Garnett, B. Ehrler and W. C. Sinke, *Science (80-.).*, 2016, **352**, aad4424–aad4424.

207 M. I. Hoffert, *Science (80-.).*, 2010, **329**, 1292–1294.

208 D. Shin, B. Saparov and D. B. Mitzi, *Adv. Energy Mater.*, 2017, **7**, 1602366.

209 D. Shin, B. Saparov, T. Zhu, W. P. Huhn, V. Blum and D. B. Mitzi, *Chem. Mater.*, 2016, **28**, 4771–4780.

210 A. D. Becke, *J. Chem. Phys.*, 2014, **140**, 18A301.

211 K. Burke, *J. Chem. Phys.*, 2012, **136**, 150901.

212 B. Richardson-Todd, *Nurs. Stand.*, 2013, **17**, 38–41.

213 R. O. Jones and O. Gunnarsson, *Rev. Mod. Phys.*, 1989, **61**, 689–746.

214 K. Lejaeghere, G. Bihlmayer, T. Bjorkman, P. Blaha, S. Blugel, V. Blum, D. Caliste, I. E. Castelli, S. J. Clark, A. Dal Corso, S. de Gironcoli, T. Deutsch, J. K. Dewhurst, I. Di Marco, C. Draxl, M. Du ak, O. Eriksson, J. A. Flores-Livas, K. F. Garrity, L. Genovese, P. Giannozzi, M. Giantomassi, S. Goedecker, X. Gonze, O. Granas, E. K. U. Gross, A. Gulans, F. Gygi, D. R. Hamann, P. J. Hasnip, N. A. W. Holzwarth, D. Iu an, D. B. Jochym, F. Jollet, D. Jones, G. Kresse, K. Koepernik, E. Kucukbenli, Y. O. Kvashnin, I. L. M. Locht, S. Lubeck, M. Marsman, N. Marzari, U. Nitzsche, L. Nordstrom, T. Ozaki, L. Paulatto, C. J. Pickard, W. Poelmans, M. I. J. Probert, K. Refson, M. Richter, G.-M. Rignanese, S. Saha, M. Scheffler, M. Schlipf, K. Schwarz, S. Sharma, F. Tavazza, P. Thunstrom, A. Tkatchenko, M. Torrent, D. Vanderbilt, M. J. van Setten, V. Van Speybroeck, J. M. Wills, J. R. Yates, G.-X. Zhang and S. Cottenier, *Science (80-.).*, 2016, **351**, aad3000–aad3000.

215 S. K. Barman and M. N. Huda, *J. Phys. Condens. Matter*, 2018, **30**, 165701.

216 H. T. Evans, *Zeitschrift für Krist.*, 1979, **150**, 299–320.

217 R. W. Potter, *Geol. Econ.*, 1977, **72**, 1524–1542.

218 G. Will, E. Hinze and A. R. M. Abdelrahman, *Eur. J. Mineral.*, 2002, **14**, 591–598.

219 K. Koto and N. Morimoto, *Acta Crystallogr. Sect. B Struct. Crystallogr. Cryst. Chem.*, 1970, **B26**, 915–924.

220 L.-W. Wang, *Phys. Rev. Lett.*, 2012, **108**, 085703.

221 J. A. Bragagnolo, A. M. Barnett, J. E. Phillips, R. B. Hall, A. Rothwarf and J. D. Meakin, *IEEE Trans. Electron Devices*, 1980, **27**, 645–651.

222 P. Lukashev, W. R. L. Lambrecht, T. Kotani and M. van Schilfgaarde, *Phys. Rev. B*, 2007, **76**, 195202.

223 S. H. Wei, Q. Xu, B. Huang, Y. Zhao, Y. Yan and R. Noufi, *Conf. Rec. IEEE Photovolt. Spec. Conf.*, 2012, **100**, 118–120.

224 S. I. Hitoshi Matsumoto, Nobuo Nakayama, Kazufumi Yamaguchi, *Jpn. J. Appl. Phys.*, 1977, **16**, 1283–1284.

225 A. M. Al-Dhafiri, G. J. Russell and J. Woods, *Semicond. Sci. Technol.*, 1992, **7**, 1052–1057.

226 P. Khatri and M. N. Huda, *Int. J. Photoenergy*, 2015, **2015**, 1–8.

227 C. N. Savory, A. M. Ganose, W. Travis, R. S. Atri, R. G. Palgrave and D. O. Scanlon, *J. Mater. Chem. A*, 2016, **4**, 12648–12657.

228 S. C. Riha, S. Jin, S. V. Baryshev, E. Thimsen, G. P. Wiederrecht and A. B. F. Martinson, *ACS Appl. Mater. Interfaces*, 2013, **5**, 10302–10309.

229 S. K. Barman and M. N. Huda, *J. Appl. Phys.*, 2020, **128**, 015703.

230 T. F. Krüger and H. Müller-Buschbaum, *J. Alloys Compd.*, 1992, **190**, L1–L3.

231 F. F. Abdi, T. J. Savenije, M. M. May, B. Dam and R. Van De Krol, *J. Phys. Chem. Lett.*, 2013, **4**, 2752–2757.

232 X. Zhu, Z. Guan, P. Wang, Q. Zhang, Y. Dai and B. Huang, *Chinese J. Catal.*, 2018, **39**, 1704–1710.

233 F. Wang, W. Septina, A. Chemseddine, F. F. Abdi, D. Friedrich, P. Bogdanoff, R. Van De Krol, S. D. Tilley and S. P. Berglund, *J. Am. Chem. Soc.*, 2017, **139**, 15094–15103.

234 J. Li, M. Griep, Y. Choi and D. Chu, *Chem. Commun.*, 2018, **54**, 3331–3334.

235 M. Nolan and S. D. Elliott, *Phys. Chem. Chem. Phys.*, 2006, **8**, 5350–5358.

236 A. Nayak, T. Ohno, T. Tsuruoka, K. Terabe, T. Hasegawa, J. K. Gimzewski and M. Aono, *Adv. Funct. Mater.*, 2012, **22**, 3606–3613.

237 D. Han, Y. Y. Sun, J. Bang, Y. Y. Zhang, H. B. Sun, X. Bin Li and S. B. Zhang, *Phys. Rev. B - Condens. Matter Mater. Phys.*, 2013, **87**, 1–5.

238 D. S. Sholl and J. A. Steckel, *Density Functional Theory*, John Wiley & Sons, Inc., Hoboken, NJ, USA, 2009, vol. 31.

239 J. Neugebauer and M. Scheffler, *Phys. Rev. B*, 1992, **46**, 16067–16080.

240 G. Makov and M. C. Payne, *Phys. Rev. B*, 1995, **51**, 4014–4022.

241 J. C. Boettger, *Phys. Rev. B*, 1994, **49**, 16798–16800.

242 V. Fiorentini and M. Methfessel, *J. Phys. Condens. Matter*, 1996, **8**, 6525–6529.

243 J. L. F. Da Silva, C. Stampfl and M. Scheffler, *Surf. Sci.*, 2006, **600**, 703–715.

244 W. Sun and G. Ceder, *Surf. Sci.*, 2013, **617**, 53–59.

245 Y. Hinuma, T. Toyao, T. Kamachi, Z. Maeno, S. Takakusagi, S. Furukawa, I. Takigawa and K. I. Shimizu, *J. Phys. Chem. C*, 2018, **122**, 29435–29444.

246 S. K. Barman and M. N. Huda, *Phys. Status Solidi - Rapid Res. Lett.*, 2019, **13**, 1–5.

247 T. J. Frankcombe and O. M. Løvvik, *J. Phys. Chem. B*, 2006, **110**, 622–630.

248 F. Izumi and K. Momma, *Solid State Phenom.*, 2007, **130**, 15–20.

249 M. L. Polak, M. K. Gilles, J. Ho and W. C. Lineberger, *J. Phys. Chem.*, 1991, **95**, 3460–3463.

250 A. D. Walkingshaw, N. A. Spaldin and E. Artacho, *Phys. Rev. B - Condens. Matter Mater. Phys.*, 2004, **70**, 1–7.

251 N. A. McDowell, K. S. Knight and P. Lightfoot, *Chem. - A Eur. J.*, 2006, **12**, 1493–1499.

252 F. Corà, M. G. Stachiotti, C. R. A. Catlow and C. O. Rodriguez, *J. Phys. Chem. B*, 1997, **101**, 3945–3952.

253 M. Stachiotti, F. Cora and C. Catlow, *Phys. Rev. B - Condens. Matter Mater. Phys.*, 1997, **55**, 7508–7514.

254 E. Bainglass, A. Walsh and M. N. Huda, *Chem. Phys.*, 2021, 111117.

255 J. M. Zhang, Q. Pang, K. W. Xu and V. Ji, *Surf. Interface Anal.*, 2008, **40**, 1382–1387.

256 R. I. Eglitis, *Appl. Surf. Sci.*, 2015, **358**, 556–562.

257 Y. Takagi, T. Yamada, M. Yoshino and T. Nagasaki, *Ferroelectrics*, 2016, **490**, 167–173.

258 X. Tian, T. Wang, L. Fan, Y. Wang, H. Lu and Y. Mu, *Appl. Surf. Sci.*, 2018, **427**, 357–362.

259 Z. Zhao, Z. Li and Z. Zou, *RSC Adv.*, 2011, **1**, 874.

260 G. Wulff, *Zeitschrift für Krist. - Cryst. Mater.*, 1901, **34**, 449.

261 G. D. Barmparis, Z. Lodziana, N. Lopez and I. N. Remediakis, *Beilstein J. Nanotechnol.*, 2015, **6**, 361–368.

262 J. W. Gibbs, *Am. J. Sci.*, 1878, **s3-16**, 441–458.

263 N. Garcia-Castello, J. D. Prades, R. Orlando and A. Cirera, *J. Phys. Chem. C*, 2012, **116**, 22078–22085.

264 K. Jackson and J. Jellinek, *J. Chem. Phys.*, 2016, **145**, 244302–1.

265 I. Rata, A. A. Shvartsburg, M. Horoi, T. Frauenheim, K. W. M. Siu and K. A. Jackson, *Phys. Rev. Lett.*, 2000, **85**, 546–549.

266 K. A. Jackson, M. Horoi, I. Chaudhuri, T. Frauenheim and A. A. Shvartsburg, *Phys. Rev. Lett.*, 2004, **93**, 013401-1–4.

267 E. Kaxiras and K. Jackson, *Phys. Rev. Lett.*, 1993, **71**, 727–730.

268 J. C. Yang, W. G. Xu and W. S. Xiao, *J. Mol. Struct. THEOCHEM*, 2005, **719**, 89–102.

269 K. Raghavachari and C. M. M. Rohlfing, *J. Chem. Phys.*, 1988, **89**, 2219–2234.

270 W. Qin, W. C. Lu, L. Z. Zhao, Q. J. Zang, C. Z. Wang and K. M. Ho, *J. Phys. Condens. Matter*, 2009, **21**, 455501.

271 R. L. Zhou and B. C. Pan, *Phys. Lett. A*, 2007, **368**, 396–401.

272 C. L. Mayfield and M. N. Huda, *Comput. Theor. Chem.*, 2013, **1019**, 125–131.

273 M. C. Piqueras, R. Crespo, E. Ortí and F. Tomás, *Chem. Phys. Lett.*, 1993, **213**, 509–513.

274 S. Yoo, J. Zhao, J. Wang and C. Z. Xiao, *J. Am. Chem. Soc.*, 2004, **126**, 13845–13849.

275 M. Anafcheh and R. Ghafouri, *Struct. Chem.*, 2014, **25**, 37–42.

276 Y. Pei and X. C. Zeng, *J. Clust. Sci.*, 2011, **22**, 343–354.

277 Y. Pei, Y. Gao and X. C. Zeng, *J. Chem. Phys.*, 2007, **127**, 044704.

278 L. Wang, D. Li and D. Yang, *Mol. Simul.*, 2006, **32**, 663–666.

279 Q. Sun, Q. Wang, P. Jena, J. Z. Yu and Y. Kawazoe, *Sci. Technol. Adv. Mater.*, 2003, **4**, 361–365.

280 J. Zhao, L. Ma and B. Wen, *J. Phys. Condens. Matter*, 2007, **19**, 226208.

281 S. Nagase and K. Kobayashi, *Chem. Phys. Lett.*, 1991, **187**, 291–294.

282 L. Wang and D. Yang, *Mol. Simul.*, 2010, **36**, 493–495.

283 K. Jug and M. Krack, *Chem. Phys.*, 1993, **173**, 439–450.

284 M. Menon and K. R. Subbaswamy, *Chem. Phys. Lett.*, 1994, **219**, 219–222.

285 J. G. Han, Z. Y. Ren, L. S. Sheng, Y. W. Zhang, J. A. Morales and F. Hagelberg, *J. Mol. Struct. THEOCHEM*, 2003, **625**, 47–58.

286 S. Barman, P. Sen and G. P. Das, *J. Phys. Chem. C*, 2008, **112**, 19963–19968.

287 J. Jia, Y. N. Lai, H. S. Wu and H. Jiao, *J. Phys. Chem. A*, 2010, **114**, 12755–12758.

288 S. Yoo, N. Shao and X. C. Zeng, *J. Chem. Phys.*, 2008, **128**, 104316.

289 S. Yoo, N. Shao, C. Koehler, T. Fraunhaum and X. C. Zeng, *J. Chem. Phys.*, 2006, **124**, 164311.

290 J. Tillmann, J. H. Wender, U. Bahr, M. Bolte, H. W. Lerner, M. C. Holthausen and M. Wagner, *Angew. Chemie - Int. Ed.*, 2015, **54**, 5429–5433.

291 F. D. Proft, C. V. Alsenov and P. Geerling, *J. Phys. Chem.*, 1996, **100**, 7440–7448.

292 R. Robles and S. N. Khanna, *Phys. Rev. B - Condens. Matter Mater. Phys.*, 2009, **80**, 115414.

293 A. Willand, M. Gramzow, S. Alireza Ghasemi, L. Genovese, T. Deutsch, K. Reuter and S. Goedecker, *Phys. Rev. B - Condens. Matter Mater. Phys.*, 2010, **81**, 201405.

294 J. Ulises Reveles and S. N. Khanna, *Phys. Rev. B - Condens. Matter Mater. Phys.*, 2006, **74**, 035435.

295 J. Ulises Reveles and S. N. Khanna, *Phys. Rev. B - Condens. Matter Mater. Phys.*, 2005, **72**, 165413.

296 E. Degoli, G. Cantele, E. Luppi, R. Magri, D. Ninno, O. Bisi and S. Ossicini, *Phys. Rev. B - Condens. Matter Mater. Phys.*, 2004, **69**, 155411.

297 D. Tománek, 2014, http://www.nanotube.msu.edu/fullerene/.

298 H. G. Xu, X. Y. Kong, X. J. Deng, Z. G. Zhang and W. J. Zheng, *J. Chem. Phys.*, 2014, **140**, 024308.

299 P. De Padova, C. Quaresima, B. Olivieri, P. Perfetti and G. Le Lay, *Appl. Phys. Lett.*, 2011, **98**, 6–9.

300 M. N. Huda, Y. Yan and M. M. Al-Jassim, *Chem. Phys. Lett.*, 2009, **479**, 255–258.